AIX-MARSEILLE UNIVERSITÉ
Faculté des Sciences

THÈSE DE DOCTORAT

École Doctorale: *Physique et Sciences de la Matière*
Spécialité: ÉNERGIE, RAYONNEMENT ET PLASMA

FENICIA:
UN CODE DE SIMULATION DES PLASMAS BASÉ SUR UNE APPROCHE DE COORDONNÉES ALIGNÉES INDÉPENDANTE DES VARIABLES DE FLUX

Présentée par:

Farah HARIRI

Soutenue le 19 Novembre 2013 devant le jury composé de:

Prof.	Laurent VILLARD	École Polytechnique de Lausanne (EPFL, Lausanne)	Rapporteur
Prof.	Eric SONNENDRÜCKER	Max-Plank-Institut für Plasmaphysik (IPP, Garching)	Rapporteur
Prof.	Peter BEYER	Université d'Aix-Marseille (AMU, Marseille)	Examinateur
Prof.	Steve COWLEY	Culham Center for Fusion Energy (CCFE, Oxford)	Examinateur
Prof.	Nabil NASSIF	American University of Beirut (AUB, Beirut)	Examinateur
Prof.	Yanick SARAZIN	CEA (IRFM, Cadarache)	Examinateur
Dr.	Maurizio OTTAVIANI	CEA (IRFM, Cadarache)	Directeur de thèse

Laboratoire d'accueil:
Institut de **R**echerche sur la **F**usion par confinement **M**agnétique
Commissariat à l'**É**nergie **A**tomique et aux Énergies Alternatives (CEA), Cadarache
13108 Saint-Paul-Lez-Durance, France

AIX-MARSEILLE UNIVERSITY
Faculty of Sciences
A dissertation in candidacy for the degree of

Doctor of Philosophy

Doctoral School: *Physics and Material Sciences*
Specialty: ENERGY, RADIATION AND PLASMA

FENICIA:
A Generic Plasma Simulation Code Using a **F**lux-Indep**EN**dent **FI**eld-Aligned **C**oord**I**nate **A**pproach

Presented by:

Farah HARIRI

Thesis defended on November 19, 2013 in front of the jury composed of:

Prof.	Laurent VILLARD	École Polytechnique de Lausanne (EPFL, Lausanne)	Referee
Prof.	Eric SONNENDRÜCKER	Max-Plank-Institut für Plasmaphysik (IPP, Garching)	Referee
Prof.	Peter BEYER	Université d'Aix-Marseille (AMU, Marseille)	Examiner
Prof.	Steve COWLEY	Culham Center for Fusion Energy (CCFE, Oxford)	Examiner
Prof.	Nabil NASSIF	American University of Beirut (AUB, Beirut)	Examiner
Prof.	Yanick SARAZIN	CEA (IRFM, Cadarache)	Examiner
Dr.	Maurizio OTTAVIANI	CEA (IRFM, Cadarache)	PhD Advisor

Research Institute:
Institute for **M**agnetic **F**usion **R**esearch
French Alternative Energies and Atomic Energy Commission (CEA), Cadarache
13108 Saint-Paul-Lez-Durance, France

Abstract

Already 60 years of intense international pursuit of the laboratory confinement of high temperature ($T > 10^8 K$) plasmas for the purpose of obtaining successful controlled nuclear fusion reactors, conceived to produce stable burning plasmas with large amplification factors. Micro-turbulence and macro-scale magnetohydrodynamical instabilities govern the confinement properties of tokamak plasmas. Nowadays, the simulation of turbulence in a full tokamak is very challenging since one must simultaneously resolve the machine size and the scales of turbulence. The scale of the turbulence is on the order of the ion gyroradius, ρ_i, while the size of an ITER-like tokamak is much larger, $a/\rho_i \sim 500$, where a is the minor radius. This requires a very fine computational grid and is slightly beyond today's computational capabilities for realistic a/ρ_i. Thus, one can conceive that much more efficient codes are made possible by a suitable choice of coordinates that allow the smallest number of grid points in a certain direction, exploiting the elongated nature of turbulence, which has short perpendicular scales but long parallel scales. The idea consists on finding a local transformation that aligns a suitable coordinate to the magnetic field, thus leading to efficient computation of the parallel derivative. For this purpose, the so-called field-aligned coordinates have been employed so far in tokamak turbulence simulations . The gain in computational efficiency obtained by using optimal coordinates can be a couple of orders of magnitude for a turbulence simulation of a large device like ITER.

In this Thesis, I develop and illustrate a new approach to field-aligned coordinates which is not based on flux variables [Hariri 2013] that I call FCI. The method employs standard Cartesian or Polar coordinates to discretize the fields. Parallel derivatives are computed directly along a coordinate that follows the local field, and poloidal derivatives are computed in the original Cartesian frame. I first show how the new method has a number of advantages over methods constructed starting from flux coordinates, allowing for more flexible coding in a variety of situations including X-point configurations. It permits high resolution in realistic tokamak geometry while retaining the important toroidal features. This method is also applicable to non-tokamak magnetic configurations. In light of these findings, a plasma simulation code FENICIA has been developed based on the FCI approach with the ability to tackle a wide class of physical models. The code has been validated on several three-dimensional test models. The accuracy of the approach is tested in particular with respect to the question of spurious radial transport, an obvious concern when abandoning flux coordinates. In this regard, I also show that numerical radial diffusion can be easily kept under control with the choice of suitable algorithms, at a minimal computational cost.

Then, tests on a 3D model for Ion Temperature Gradient (ITG) driven turbulence in cylindrical geometry demonstrate that the method is well suited to exploit the flute property of small parallel gradients by minimizing the number of degrees of freedom needed to treat a given problem in an accurate and efficient manner. Benchmarks and numerical method accuracy are detailed in the linear regime. Moreover, simulations in the nonlinear turbulent regime allow one to recover, at reduced numerical cost, the standard features of slab ITG turbulence. Finally, the method was tested in an X-point configuration such as one with a magnetic island. Results show good agreement with the exact solutions of the sound wave propagation inside and outside the island. On the magnetic separatrix including the X-point, convergence studies are performed and adequate conservation properties are verified showing the robustness of the approach in very demanding situations.

Résumé

Ce travail porte sur le développement et la vérification d'une nouvelle approche de coordonnées alignées, qui tire partie de l'anisotropie du transport dans un plasma immergé dans un fort champ magnétique. Sa prise en compte dans les codes numériques permet de réduire grandement le coût de calcul nécessaire pour une précision donnée. Une particularité de l'approche nouvellement développée dans ce manuscrit est en particulier sa capacité à traiter, pour la première fois, des configurations avec point X. Toutes ces analyses ont été conduites avec FENICIA, code modulaire entièrement développé dans le cadre de cette thèse, et permettant la résolution d'une classe de modèles génériques.

Le premier chapitre précise le contexte de la physique des tokamaks dans lequel se place ce travail. C'est une introduction à la problématique du confinement d'un plasma dans un champ magnétique et au principe du tokamak. La rupture du confinement due à la turbulence et aux instabilités magnétohydrodynamiques (MHD) est également présentée. L'anisotropie du transport dans un tokamak, qui a motivé le développement des coordonnées alignées et qui est donc au cœur du projet de cette thèse, est présentée en détail. La motivation du travail est ainsi exposée, et replacée dans le contexte général des différents systèmes de coordonnées alignées qui sont proposés dans la littérature et utilisés dans les codes internationaux. Dans ce chapitre introductif, la classe de modèles abordés dans la thèse est également présentée sous une forme générique, qui utilise un découplage entre parties résolues numériquement de manière explicite et implicite.

Le deuxième chapitre est consacré à un état de l'art des systèmes de coordonnées utilisés dans les codes dédiés à l'étude de la turbulence dans les plasmas de tokamaks. Ces rappels historiques et scientifiques permettent de mettre en exergue les avancées et avantages que représente la technique introduite dans ce travail. Du fait que les gradients dans la direction des lignes de champ magnétique sont de plusieurs ordres de grandeur plus petits que les gradients perpendiculaires aux lignes de champ, des systèmes de coordonnées curvilignes adaptées à cette propriété permettent de réduire considérablement les coûts

de calcul, en autorisant en particulier un maillage plus lâche dans une des directions. Divers types de telles coordonnées curvilignes ont étés introduites dans la littérature depuis plus de vingt ans. Une revue des principales variantes est faite dans ce chapitre, rappelant leurs avantages et inconvénients. L'idée introduite par M. Ottaviani, qui consiste à utiliser un système de coordonnées où l'abscisse curviligne le long des lignes de champ est décrite localement entre deux plans poloïdaux par la coordonnée toroïdale, est rappelée et généralisée à un contexte indépendant de tout système de coordonnées de flux. Cette nouvelle méthode est appelée FCI pour Flux Coordinate Independent. Son principe est de discrétiser un problème tri-dimensionnel (3D) dans un tokamak par un petit nombre de plans poloïdaux. Ces mêmes plans peuvent être discrétisés de manière quelconque, mais avec un maillage assez fin pour représenter les variations perpendiculaires aux lignes de champ. En pratique un maillage cartésien des plans poloïdaux est utilisé dans ce travail. Pour la discrétisation des dérivées parallèles, la méthode utilise une ligne de champ qui, d'un de ses côtés, prend appui sur un point du maillage poloïdal. L'autre extrémité de cette même ligne n'est pas sur un point de grille *a priori*. Cela nécessite la détermination de l'intersection de cette ligne de champ avec les plans poloïdaux voisins. Une interpolation sur ceux-ci est alors réalisée, ayant comme avantage de permettre une discrétisation indépendante de chaque plan poloïdal. Dans la dernière partie du chapitre, les outils mathématiques nécessaires au calcul efficace des lignes de champ et des dérivées parallèles avec cette méthode sont précisés. Les démontrations sont données, et des applications à certains cas particuliers permettent de mieux comprendre le principe. Il est précisé également comment des configurations avec point X peuvent aussi être traitées avec cette méthode. Finalement, une présentation mathématique avec une suite de propositions et de leur démonstration est adoptée pour la partie technique énonçant les résultats permettant de calculer de manière efficace les dérivées le long des lignes de champ.

Le troisième chapitre est consacré à la description du code FENICIA et des algorithmes qui y sont utilisés. Ce code parallèle en Fortran a été développé entièrement au cours de cette thèse. Les schémas d'intégration en temps sont présentés en premier. Ils sont destinés à pouvoir s'appliquer à toute une classe de systèmes abstraits d'équations différentielles partielles (EDP) ayant en commun d'avoir une partie linéaire qui pourra être traitée implicitement et une partie non-linéaire qui sera traitée explicitement. Une méthode de type prédicteur-correcteur d'ordre 2 construite pour stabiliser un schéma saute-mouton est dérivée pour ce type de problème. Les différents opérateurs différentiels en espace apparaissant dans les opérateurs abstraits sont discrétisés par des schémas de différences finis adéquats, y compris ceux basés sur les dérivées parallèles introduits dans le chapitre précédent. En dehors de techniques classiques, un point spécifique à la méthode développée dans cette thèse est l'interpolation des valeurs à l'intersection avec une ligne de champ dans les plans poloïdaux. Une interpolation de type Hermite bicubique, donc d'ordre 4, est utilisée pour ceci, les dérivées nécessaires étant reconstruites à partir des valeurs ponctuelles voisines par différences finies d'ordre correspondant. Une vérification de l'ordre de la méthode est effectuée ainsi qu'une comparaison à une méthode de splines cubiques de MATLAB, montrant que pour le problème traité, l'erreur est comparable. Une représentation graphique des modules du code ainsi que des extensions possibles est présentée, ainsi que pour l'évolution en temps du code. Ce chapitre montre la modularité du code permettant de le faire évoluer.

Le quatrième chapitre décrit la validation du code et de la méthode FCI développée dans cette thèse sur des cas tests représentatifs. Il commence par la validation de la méthode d'interpolation, en particulier sur le cas le plus simple du transport parallèle aux lignes de champ d'une quantité scalaire. Pour estimer la précision numérique nécessaire, une étude physique des ordres de grandeur des différents termes impliqués est menée. Ensuite une étude de la diffusion numérique est proposée dans un cas où le gradient parallèle est nul et où le seul transport transverse aux lignes de champ proviendrait de la diffusion numérique. On vérifie que cette diffusion numérique est régie par le nombre de points par longueur d'onde. Ensuite commence la validation de l'approche FCI à proprement parler, en montrant que les ondes acoustiques ioniques peuvent être simulées par cette approche avec une résolution très faible dans la direction toroïdale. Finalement, le code entier est validé sur des simulations de modèles de plus en plus complets. D'abord un modèle centre-guide 2D avec diffusion est validé pour tester le comportement dans un seul plan poloïdal. On passe ensuite à un modèle fluide linéaire d'instabilité ITG. Dans les deux cas les résultats numériques sont en accord avec la théorie, ce qui permet une validation convaincante du code.

Dans le cinquième chapitre, on exploite le code pour des simulations non linéaires d'une turbulence portée par le gradient de température ionique, dite ITG (Ion Temperature Gradient), qui joue un rôle important dans le transport de chaleur dans les tokamaks. Est également étudié un cas de géométrie avec îlots magnétiques que les approches précédentes de coordonnées alignées ne pouvaient pas traiter. Le chapitre commence avec une présentation du modèle complet fluide de turbulence implémenté dans le code. Les simplifications effectuées sont également discutées en relation avec les objectifs de la thèse. Ensuite une discussion complète du modèle linéaire est proposée avec un calcul de la relation de dispersion et des seuils et taux d'instabilité, avant de passer aux simulations non-linéaires. Une étude de l'erreur en fonction du nombre de points toroïdaux est en particulier effectuée. Elle montre qu'une précision tout à fait satisfaisante est atteinte à partir d'une quinzaine de points seulement dans la direction toroïdale. Pour montrer l'avantage principal de la méthode par rapport aux techniques précédemment utilisées, le chapitre se conclut par une discussion d'un cas test avec point X et de tests au travers de la séparatrice. La bonne convergence du code vers des solutions analytiques de part et d'autre de la séparatrice d'un îlot magnétique, ou vers la solution numérique centrée sur la séparatrice elle-même, attestent la capacité du code à traiter cette configuration magnétique.

Le dernier chapitre conclut la thèse en rappelant les principaux résultats obtenus et les points forts de la méthode ainsi que les axes de recherche futurs, en particulier sur la physique à ajouter pour traiter des cas plus réalistes. En résumé, la méthode développée dans ce travail est validée. Elle peut s'avérer pertinente pour un large champ d'application dans le contexte de la fusion magnétique. Il est montré dans cette thèse que cette technique devrait pouvoir s'appliquer aussi bien aux modèles fluides que gyrocinétiques de turbulence, et qu'elle permet notamment de surmonter un des problèmes fondamentaux des techniques actuelles, qui peinent à traiter de manière précise la traversée de la séparatrice.

Acknowledgments

In loving memory of my paternal grand-mother

To my Parents, I give my appreciation for your support and love over the years. You mean the World to me.

A million thanks to my two brothers Ali and Mohamad, and to my sister Amani who have always been wonderfully supportive wherever and whenever. I am also lucky to have my remaining three grandparents by my side to whom I owe many thanks for their love and encouragement. Big thanks to my maternal grand-father who flied all the way to France to be by my side on the day of my defense. I am grateful to my uncles and aunts as well, with special thanks to my uncle Bassem for granting me endless support, even through the post when needed. I would also like to offer thanks to aunt Neimat for feeding me with delicious food.

It has been more than three years since I left home. On September 19th 2010, I moved to the hamlet of Cadarache, a small settlement of houses in the middle of nowhere, southern France. Being there for at least nine months to live on my own was not really easy, let alone the number of times I experienced melancholy, dizziness and mood swings. Mom, Dad, I missed you back then more than I ever did. Spring came earlier that year. All of a sudden, in almost any part of my apartment, I started seeing centipedes roaming through my place. Those ugly unpleasant pests were there darting into my view with their legs rippling and antennae waving. They run and stop, run and stop again. And I was there sitting with my Baygon insecticide bottle, my only weapon, waiting for the combat. When one of them shows up, we both stop; watch each other, both of us ready to run. Often the battle was short and I always proudly won! Ever since I found the first one seemingly waiting to ambush me in the bathtub, Gaaaack..., I decided to urgently move to the city area. On July 15th 2011, I moved to 38 Rue Mignet located in Aix-en-Provence. Since then, my everyday life pretty much changed. Even though at my arrival, I was miffed by very persistent mice that I found above the kitchen stove nestling in my food cupboards. I have tried poison traps, glue traps, good old-fashioned mousetraps and high tech sonic pest control, in vain! After this experience, I found myself outwitted by a 3 ounce rodent and I have to admit that mice are far more intelligent than most people give them credit for. It took me a while before I could completely get rid of them. After all, I can't but cherish all the blessings I have had throughout the two years of my stay in Aix-en-Provence. It has been a pleasant and astonishing period of time. I enjoyed my Saturday morning coffee at the market. I met great friends. I traveled to many interesting places. I have been loved. I had some good international food. And, I always enjoyed the sunny Aix-en-Provence. It's time for me to move on again and look forward for another experience! Mom, Dad, it's true that now I have my own life, but I will be forever grateful for your unwavering support. Today, I hope I made you proud and I thank you for your understanding.

I will always remember my years at Cadarache happily. Thought it was a difficult path, I was aided by many friends and colleagues who made this PhD thesis possible.

Foremost, I thank Alain Bécoulet, the Head of the Institute for Magnetic Fusion Research (IRFM) for accepting my candidacy to join the Transport Turbulence and MHD group (GTTM). I also thank the administrative staff for their presence and efforts. Thanks to Emmanuel Joffrin (for his scientific support, for beefing up my french vocabulary and also for the many discussions about history, cultures and diversity), to Jean-Michel Bernard (for controlling my expenses at CEA and simulating my mood as a function of my daily look), Tuong Hoang (for his encouragement), Jean-Marc Ané (for the article he wrote about my work) and Yvan Lausenaz (for his support).

I owe more than simple thanks to Xavier Litaudon, the Head of the Plasma Heating and Confinement department for his constant encouragement, for having faith in me and for making me feel confident every time I was losing motivation. I offer my heartfelt appreciation for his loyalty to all students, and for his kindness to me in particular. I will always remember your words, your positive energy and your motivational approach that helped me hold on during times of stress and disillusionment.

I would like to express my gratitude to my advisor, Maurizio Ottaviani, whose expertise, vast knowledge and understanding, added considerably to my graduate experience. Thank you for being so tolerant and for letting me drive the Thesis in my own way. Thank you for being tremendously kind. I can't forget that when I first arrived in France, you were there helping me in all the procedures to settle in and providing me with valuable advice. It was a great experience working with you.

It has been a true pleasure working with Yanick Sarazin, to whom I owe appreciation as well for his contribution to this work, particularly the material constituting Chapter 5. I am grateful to his willingness to explain to me many ideas I otherwise might not have grasped. Thank you for the great informative courses you willingly give to all students on a regular basis. Besides being an excellent teacher, you have a sense of humor and an infectious laughter that I will most certainly miss.

Thanks also are due to my PhD committee. I thank Prof. Laurent Villard for the very fruitful discussions about the tests across the separatrix including the X-point and I look forward to working with his team at EPFL. I would particularly like to acknowledge discussions with Prof. Steve Cowley whom I had the chance to meet at the Culham Plasma Physics summer school in 2011. He has given me a lot of support and I deeply appreciate his modesty. I thank Prof. Éric Sonnendrücker for reading my manuscript carefully and making useful suggestions. I thank Peter Beyer for his help and advice especially during the ANR E2T2's annual meetings. I would like to warmly thank Prof. Nabil Nassif for introducing me to the world of Computational Science. He was my mentor in the course of 5 years of study at AUB and I can't but thank him for his guidance and good advice. I further offer a special thanks to the head of the AUB student section Ms Leila Knio and to my mathematics teachers Abdallah Lyzzaik and Mohammad el-Hajj for supporting me and having faith in me throughout my entire graduate studies.

I owe thanks to Peter Hill who generously helped me throughout the third year of my PhD with many useful tips. He also helped in adding features to the code including the magnetic island tested in Chapter 5.

Thanks to Xavier Garbet whose foresight and rigorous suggestions have been of great help throughout this work.

I sincerely thank Yves Peysson for the many wonderful conversations and useful suggestions (in particular concerning the moving average test presented in Chapter 5). Every single time we discussed I learned something new about life, about science and technology, about medicine, about psychology... Your words and insights have surely reshaped a lot of things in my life, thank you Yves.

I thank Greg Hammett, C.S. Chang and Jeff Candy for the many helpful discussions during the IPAM workshop in the U.S. I also thank Wendell Horton for the enlightening conversations on Turbulent transport models.

To Sheldong Wang, I owe thanks for organizing my visit to the SWIP lab and for introducing me to Chengdu (China). I would also like to thank Volker Naulin for inviting me to Roskilde (Denmark) and I appreciate his interest in using the FCI approach.

I am extremely honored and grateful to receive the Itoh Project Prize in

Plasma Turbulence for 2013 at the 40th EPS conference on Plasma Physics held in Espoo (Finland). I would like to thank Prof. Sanae-I Itoh and the award's committee (S. Itoh, A. Fasoli, A. Fujisawa, E. Gusakov, C. Hidalgo, K. Itoh, U. Stroth) for their recognition of my accomplishments and efforts.

I am grateful to my colleagues at CEA. Because I can not list them all, I would like to salute a few special individuals. First, thanks to Patrick Tamain and Ahmad Ratnani for useful discussions about the numerical schemes used in this work. Many thanks to Philippe Ghendrih (especially for the refreshing everyday good mornings), Roland Sabot, Chantal Passeron, Virginie Grandgirard, Guillaume Latu, Rémi Dumont, Patrick Maget, Guilhem Dif-Pradalier, Marina Bécoulet, Marc Goniche, Didier Moreau, Gloria Falchetto, Gerardo Giruzzi, Guido Ciraolo and Joan Decker. I also thank Patrice Fiet for the wonderful photo album of my defense.

To my Friends, our nights, our trips, our talks, our smiles... All will remain woven into my memory. Girls first! Thanks to Emelie Nilsson for the crazy happy moments we spent together and for supporting me in shaky times. Thanks to Claudia Norcini for the nice moments we shared in the office. I offer very special thanks to Timothé Nicolas who kept me sane for the past three years– Thank you for having been by my side no matter what. Thanks to Didier Vezinet, that marvelous guy to whom I owe my respect and recognition for his kind help and support. I would like to thank Grégoire Hornung for the amazing time we shared together. I thank Jean-Baptiste Girardo for making the past year so interesting– I never thought I would share such a mutual understanding with anyone, you made my days brighter. Thanks to François Orain for being so caring and funny. I owe my next thanks to Maxime Lesur who filled my first three months with laughter until he left France. He taught me the Fortran language and helped me in deriving the gyrofluid model presented in this thesis. So much thanks to Shimpei Futatani for the many hours of complicity and amazement. Thanks to David Zarzoso for always being there to help out and answer my questions. Thanks to many more folks: Thomas-Cartier Michaud, Jérémie Abiteboul, Antoine Merle, Yue Dong, Dmytro Meshcheriakov, Bilal Chouli, Walid Helou, Maxim Irishkin, Hugo Arnichand, Jonathan Jacquot, Hugo Bufferand, Laurent Chôné, Arnaud Monnier, Damien Estève, Pierre Cottier, Nevenick Calec, Alexandre Storelli, Florian Le Bourdais, Alexandre Fil, Doriana Milelli, Fabien Rozar, Aakanksha Saxena, Olivier Fabbris, Marco Mazzei, Sabine Cockenpot, Hyacinthe Dujol and Liu Feng.

Last but not least, I am especially grateful to Sophie Moufawad for her support, confidence and understanding. I also thank Ghina El-Jannoun particularly for the awesome trip we did to Monaco. I further thank Jessy Haykal, Nadine Mouhanna, Sahar Oueidat, Fatmeh Hammoud, Marwa Aidibi, Nadwa Chatila, Loay Kadri and Rayan Makarem for being such good friends to me and always reminding me that everything will work out.

Cadarache, December 2012

From left to right:
György STEINBRECHER, Grégoire HORNUNG, Marc GONICHE, Francesco PALERMO, Fabien ROZAR, Thomas CARTIER-MICHAUD, François ORAIN, Virginie GRANDGIRARD, Guillaume LATU, Alexandre FIL, Julien ROBERT, Ahmed RATNANI, Farah HARIRI, David MOULTON, Jonathan JACQUOT, Timothée NICOLAS, Aurore BACK, Emmanuel JOFFRIN, Jean-Michel BERNARD, Laurent COLAS, Mervat MADI.

Contents

List of Figures

Chapter 1

Introduction

> فَقُل لِمَن يَدَّعِي في العِلمِ فَلسَفَةً،
>
> حَفِظتَ شَيئًا وَ غَابَت عَنكَ أَشيَاءُ
>
> ---
>
> أَبُو نَوَّاس (٧٤٧ - ٨١٥)

Contents

Acrylique (F. Hariri, 2005)

Today, fusion energy is under the spotlight again as a carbon-free energy source. Planet Earth is the only planet on which life exists, as far as we know. Earth was formed 4.6 billion years ago, the geomagnetic field and the ozone layer were created shielding most of the harmful radiation from the Sun and realizing an environment where only the energy of light reaching the ground was useful for life. As the use of fossil fuel resources has expanded significantly in developed countries, large amounts of carbon dioxide are emitted influencing the environment of Earth. An era of huge energy consumption is beginning in the twenty-first century.

The ultimate objective of fusion research is to study the conditions and design of fusion devices for reaching a burning plasma i.e., a fully ionized gas self-sustained in an extreme state by power released from the fusion reactions of its atomic nuclei. The burning plasma would then provide a new reliable, clean and safe power producing system. To achieve this, fusion makes two demands. Firstly, to ignite the plasma, temperatures in the order of hundreds of millions of degrees centigrade must be attained for significant fusion yield. The second, which is considered as the most difficult challenge, is to sustain the plasma at these temperatures by confining and controlling it in order to maintain its density and ensure that it does not suffer excessive heat losses. Tokamaks, a large family of fusion research devices which early development took place in the late 1950's, utilize an ingenious scheme that addresses both challenges at the same time. In this context, a worldwide cooperation aims to build in south France (Cadarache) the International Thermonuclear Experimental Reactor-ITER project a Sun on Earth, oriented towards demonstrating the technical and scientific viability of fusion as an energy source. More information about this project and about fusion theoretical concepts are available in [Wesson 2011, Hazeltine 2003, Chen 1984, Tomabechi 1991, Holtkamp 2007].

A tremendous amount of development remains before fusion can be applied to the commercially successful generation of electricity. Future experiments will be large and expensive, costing as much as several billions of dollars each. Such machines must be designed to perform optimally, allowing little room for uncertainty. Numerical studies of plasma confinement is playing a profoundly important role in designing these machines. It is an essential tool in analyzing the equilibrium, stability, and transport of all current major fusion experiments. Even when restricting to Magneto-Hydrodynamical (MHD) and turbulent transport processes, the range of time scales to be resolved in a fusion plasma is already very broad. It typically extends from about 10^{-6}s for the fastest growing instabilities to the energy confinement time of several seconds, the time scale required for the plasma profile to relax to a steady state. As far as turbulence is concerned, it develops on time scales in the range of a fraction to several milliseconds. Spatial scales are also very disparate. They range from the Larmor (or cyclotron) radius ρ_s of the order of a few millimeters for ions to the machine size a of a few meters in the directions transverse to the equilibrium magnetic field $\mathbf{B}$. As a matter of fact, it is computationally very expensive to run algorithms that embody these complex processes on today's generation of computers. Although ab initio gyrokinetic particle simulations can now model the full torus down to ITER-relevant ion spatial scales, namely $\rho_* \equiv \rho_i/a = 2.10^{-3}$, including the electron scales requires to step down the size of the domain of study. Besides, even when restricting to kinetic ions, nowadays most powerful supercomputers can hardly allow for the exploration of self-organization states in ITER-like plasmas on energy confinement times.

However, as will be extensively discussed in this thesis, much computer resources can be spared by employing coordinate systems which take benefit of the physical characteristics of magnetized plasmas, namely the strong anisotropy of both spatial and temporal scales in the parallel and transverse directions (with respect to the equilibrium guiding magnetic field $\mathbf{B}$). In turn, the full torus can be resolved much more cheaply if a loose discretization is used in the parallel direction, while still resolving the relevant scales.

1.1 Tokamak topology and plasma confinement

1.1.1 Topology and Magnetic Equilibrium

When they are immersed in a constant magnetic field, constant both in magnitude and in direction, charged particles undergo a helical motion along the magnetic field lines. The radius of the cross-section of the helix of "s" species is given by the Larmor radius $\rho_s = m_s v_\perp / e_s B$, while the gyro-frequency is $\omega_{cs} = e_s B/m_s$. Here, m_s is the mass, $v_\perp$ the transverse velocity, e_s the charge and B the magnitude of the magnetic field. Particles are all the more bound to field lines since the magnetic field magnitude is large. This is the basic principle of plasma confinement by means of a magnetic field. For thermal particles at temperatures of the order of $T_i \sim T_e \sim$ 20keV, then $v_\perp \sim v_{th} = \sqrt{T/m}$, with $v_{thi} \sim 10^6$m.s^{-1} for Deuterium ions and $v_{the} \sim 6.10^7$m.s^{-1} for electrons, so that Larmor radii are of order of $\rho_i \sim 4.10^{-3}$m and $\rho_e \sim 6.10^{-5}$m for a magnetic field of $B = 5.3$T. Conversely, particles are almost free to stream along the magnetic field (up to trapping effects in between local mirrors, mainly due to the inhomogeneity of B along the magnetic field lines). These roughly correspond to the ITER parameters.

If the motion of charged particles is constrained by the cyclotron gyration in the plane transverse to $\mathbf{B}$, it remains free along the magnetic field. Then arises the question of the confinement in the third direction, namely the parallel one. Two options can then be envisaged: either open or closed magnetic configurations. Open ones face the problem of particle and energy losses at the end points. They have rapidly revealed inefficient in view of building economically viable fusion power plants, even when adding magnetic mirrors to reduce these losses. The only alternative then relies on closed configurations. From the mathematical point of view, closed configurations of the 3-dimensional (3D) magnetic equilib-

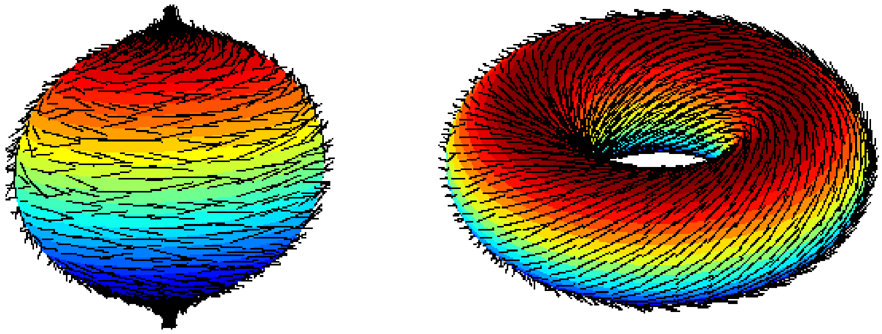

Figure 1.1: Hairy ball (left) and doughnut (right), showing the existence of at least one (here two) cowlick on the ball. Conversely, the doughnut can be entirely covered without any cowlick.

rium can be topologically equivalent to either a sphere or to a torus (possibly with several holes). Here comes into play the so-called *hairy ball theorem*, which was first proved by L.E.J. Brouwer in 1912, after some seminal works by the French mathematician Henri Poincaré (1854-1912) at the end of the 19th century, among others. This theorem states that: « For the ordinary sphere, if f is a continuous function that assigns a vector in $\mathbf{R}^3$ to every point p on a sphere such that $f(p)$ is always tangent to the sphere at p, then there is at least one p such that $f(p) = 0$ ». In other words, whenever one attempts to comb a hairy ball flat, there will always be at least one tuft of hair at one point on the ball (see Fig. 1.1).

When applied to the issue of plasma confinement by means of a magnetic field, this theorem states that any closed magnetic flux surface which would be topologically equivalent to a sphere would unavoidably have a point where the magnetic field vector would vanish. The plasma would then inevitably leak from this critical point, since it would no longer be confined by any magnetic field. Indeed, the confinement of the plasma intrinsically requires that the surface is covered by a non-zero magnetic field everywhere. This explains why only toroidal configurations are relevant for magnetic confinement, since this is the only 3D configuration which is not subject to any equivalent of the hairy ball theorem (Fig. 1.1).

The second difficulty then consists in generating such stable toroidal magnetic flux surfaces. In a tokamak, like the one shown in Fig. 1.2, a high temperature plasma is confined in an axisymmetric toroidal vessel by a helical magnetic field, as illustrated in Fig 1.3. The main component of the magnetic field $\mathbf{B}$ is the toroidal field $\mathbf{B}_\varphi$, produced by poloidal currents in external coils. This component of the magnetic field is of the order of a few Teslas, which is typically 5 orders of magnitudes larger than that of the Earth. The smaller (typically by one order of magnitude) poloidal magnetic field $\mathbf{B}_\theta$ is produced by the toroidal current $\mathbf{I}_p$ of several mega Ampère which circulates in the plasma along the toroidal direction (cf. Fig. 1.3). This current is primarily generated by a transformer effect, by varying the magnetic flux inside a central solenoid located on

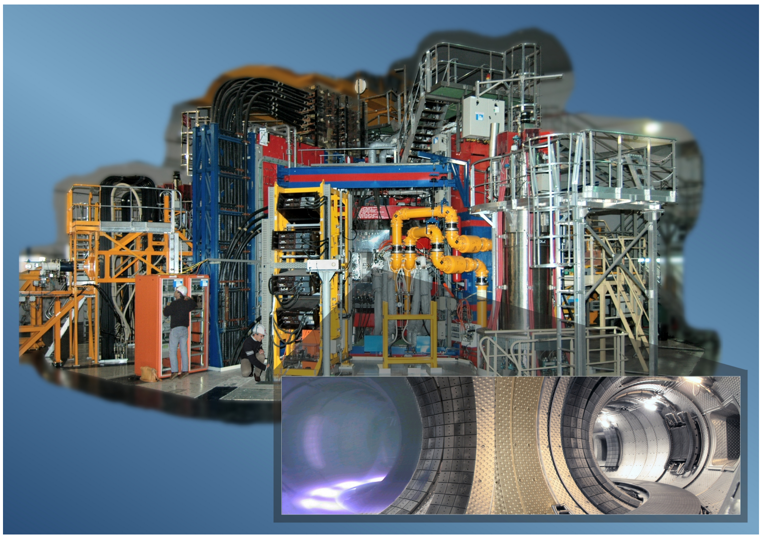

Figure 1.2: The tokamak Tore Supra, at CEA Cadarache, France

the symmetry axis of the torus. The plasma then plays the role of the secondary circuit. The combination of $\mathbf{B}_\varphi$ and $\mathbf{B}_\theta$ causes field lines to twist around a torus. The resulting magnetic flux surfaces are nested tori, characterized by a mean helicity of the field lines. In section 1.1.2 are briefly recalled the different magnetic field representations in toroidal geometry.

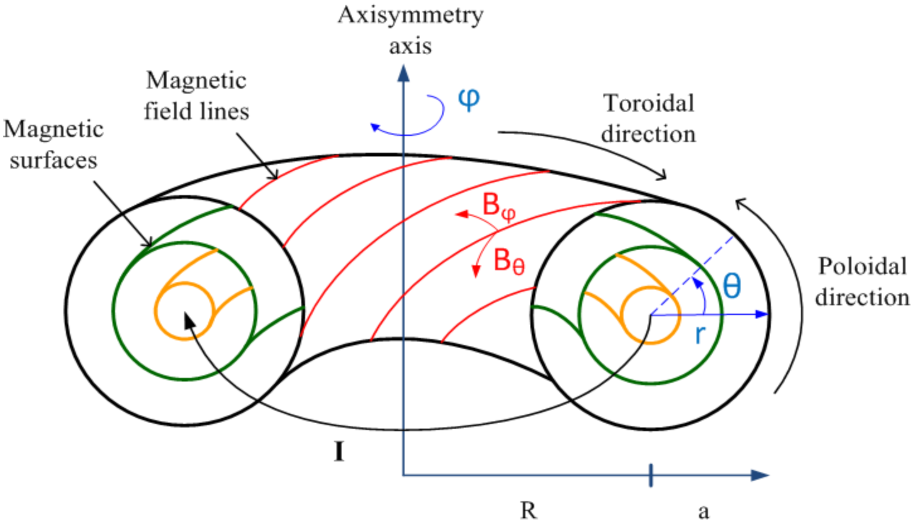

Figure 1.3: Schematic of the magnetic configuration of a torus described here by the toroidal coordinate system (r, θ, φ) with aspect ratio R/a. R denotes the major radius measuring distance from the symmetry axis, and a is the minor radius measuring distance from the magnetic axis.

1.1.2 Mathematical description of a Tokamak magnetic equilibrium

Preliminaries

Coordinates should be introduced to understand the physics of the torus, quantitatively. For this purpose, I recall in this section the basic definitions used to describe the torus coordinate systems that will be discussed throughout this thesis.

Magnetic field lines are lines which are everywhere tangent to the magnetic field. In other words, the magnitude B of $\mathbf{B}$ can vary along these lines, but $\mathbf{B}.\boldsymbol{\nabla} s = 0$, with s the curvilinear abscissa along the field line. *Magnetic surfaces*, or *flux surfaces*, correspond to those surfaces engendered by field lines. Their normal vector is everywhere orthogonal to the magnetic field. To define a coordinate system, we need to introduce three spatial functions

$$\psi(\mathbf{x}), \theta(\mathbf{x}), \varphi(\mathbf{x}) \tag{1.1}$$

which have non-coplanar gradients. Mathematically, this is a condition on the triple vector product of the gradients, or the Jacobian J,

$$\boldsymbol{\nabla}\psi \times \boldsymbol{\nabla}\theta.\boldsymbol{\nabla}\varphi \equiv J^{-1} \geq 0, \tag{1.2}$$

where the equality can hold only at isolated singular points, for example at the origin of the coordinate system (or at the magnetic axis). The coordinate system is said to be direct if the Jacobian J is strictly positive.

Flux coordinates are a set of coordinate functions adapted to the shape of the flux surfaces. *Flux labels* correspond to f functions which are constant on flux surfaces. To make (1.1) a magnetic flux coordinate system, we choose ψ to be a flux label, i.e.,

$$\mathbf{B}.\boldsymbol{\nabla}\psi = 0 \tag{1.3}$$

We take θ to be a poloidal angle (increasing the short way around the torus) and φ to be a toroidal angle (increasing the long way around the torus), each varying between 0 and 2π. Here we will choose φ to be the same angle as that in a cylindrical coordinate system, making these axisymmetric magnetic flux coordinates. Thus, we have $\partial/\partial\varphi = 0$ for axisymmetric quantities.

Efforts to provide the most appropriate coordinates for the torus have lead to two most commonly used flux coordinate systems: the Hamada coordinates [Hamada 1962] in which the angle variables are chosen to make the Jacobian a constant; and Boozer coordinates [Boozer 1981] which is obtained if we take the Jacobian to be proportional to the inverse of the square of the magnetic field. These coordinates have been shown to be particularly useful for calculating guiding center drift orbits in magnetic confinement devices [Boozer 1981, Boozer 1980, White 1984].

Expression of B in flux coordinates

In a tokamak equilibrium, there exist two common labels of magnetic flux surfaces. These are the poloidal flux ψ_P (also simply ψ) and the toroidal flux ψ_T. The poloidal flux is defined on a ribbon-like surface S_θ stretched between the magnetic axis and the flux surface at a given value of θ by:

$$\psi_P = \int_{S_\theta} \frac{\boldsymbol{\nabla}\theta}{|\boldsymbol{\nabla}\theta|}.\mathbf{B}\; dS \tag{1.4}$$

Similarly, but at given values of φ, the toroidal flux is defined by:

$$\psi_T = \int_{S_\varphi} \frac{\boldsymbol{\nabla}\varphi}{|\boldsymbol{\nabla}\varphi|}.\mathbf{B}\; dS \tag{1.5}$$

From these functions, it is possible to construct a flux label function $r(\psi)$ with the dimension of a length.

Then, the general form of the magnetic field in an axisymmetric toroidal configuration like a tokamak is:

$$\mathbf{B} = F\boldsymbol{\nabla}\varphi + \boldsymbol{\nabla}\psi \times \boldsymbol{\nabla}\varphi \tag{1.6}$$

where F can be shown to be a function of the poloidal magnetic flux ψ only: $F(\psi)$ [Hazeltine 2003]. By computing the scalar product of $\mathbf{B}$ with the toroidal direction vector $\boldsymbol{\nabla}\varphi$, it readily appears that the function F relates to the toroidal component of the magnetic field $B_\varphi \equiv R\mathbf{B}.\boldsymbol{\nabla}\varphi$: $F(\psi) = RB_\varphi$.

One important quantity for characterizing the magnetic equilibrium of a tokamak plasma is the measure of the number of toroidal turns per poloidal turn of these field lines, called the *safety factor* q. It can be expressed as the rate of change of toroidal flux with poloidal flux as follow:

$$q = \frac{d\psi_T}{d\psi_P} \tag{1.7}$$

q is constant on a given flux surface, but varies from one surface to another. Its logarithmic variation across the flux surfaces defines the *magnetic shear* $s \equiv \mathrm{d}\log q/\mathrm{d}\log r$, with r a radial coordinate labeling magnetic surfaces. Both the safety factor and its shear have important implications for the MHD stability of the plasma. q typically varies from 1 in the core plasma, on the magnetic axis, to several units in the vicinity of the last closed field surface. The safety factor q is so called because of the role it plays in determining stability. If q is a rational $q = m/n$, where m and n are integers, the field line joins up on itself after m toroidal and n poloidal rotations. Rational surfaces play a critical role in the confinement properties of the plasma, since they are the locations where macro-MHD instabilities preferentially develop.

The magnetic geometry around the X-point

This fairly simple description of the tokamak magnetic equilibrium omits one important characteristic of magnetic surfaces, which is encountered in a certain number of devices. It deals with the existence of an *X-point* at the boundary of the plasma confined region. The current flowing in judiciously located at external toroidal coils is used so as to cancel the poloidal component of B at some specific location. In this case, one moves from a limiter configuration, where the last closed field surface (LCFS) is created by the direct interaction with plasma facing components (fig.1.4a), to an axisymmetric divertor one, where the LCFS intercept the divertor target plates in a private region only, far from the main confined plasma (fig.1.4b). The advantage of such diverted plasmas is then to benefit from a larger volume to radiate the power that is convected out of the confined plasma.

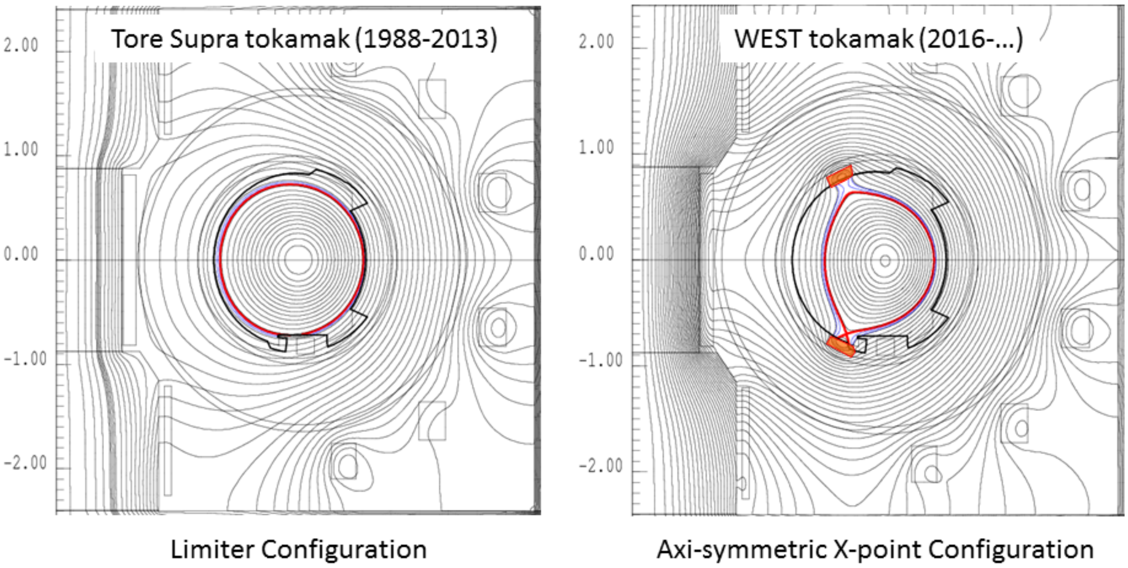

Figure 1.4: (left) Tore Supra tokamak (CEA, France) with a limiter configuration. (right) WEST tokamak (CEA, France) with an axi-symmetric X-point divertor.

The X-point connects two otherwise-separated magnetic surfaces. It is singular in the sense that the safety factor q diverges at this point: there, the field lines no longer loop poloidally (cf. discussion in section 1.1.2). When plasmas are bounded by a separatrix as shown in Fig. 1.5, the q profile is fundamentally modified. The reason is that the value of q for surfaces close to the separatrix is dominated by the null at the X-point. Let d be the shortest distance of a flux surface from the X-point. The analytical expressions of q as $d \longrightarrow 0$ in terms of $\mathbf{B}_\theta$ and $\mathbf{B}_\varphi$ can be written as:

$$q \longrightarrow \frac{\mathbf{B}_\varphi}{\pi R|\nabla \mathbf{B}_\theta|} ln\frac{\lambda}{d} \tag{1.8}$$

where λ is a length characterizing the overall geometry. Thus, as the separatrix is approached, $q \longrightarrow \infty$. It turns out that the numerical implementation of the parallel operator $\nabla_\parallel$ which involves q, is critical in the neighborhood of the X-point and shall be discussed in the next section.

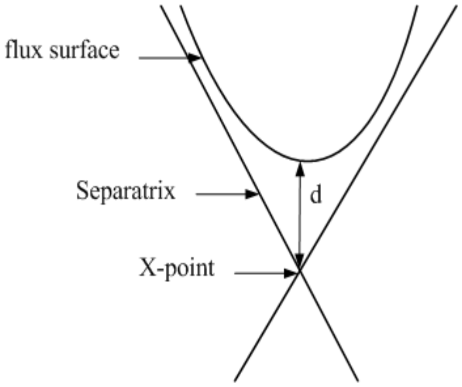

Figure 1.5: Illustrating the geometry of the flux surface around the X-point when the plasma is bounded by a separatrix

1.1.3 Basics of plasma confinement

When considering single particle trajectories, the fact that the field lines are helical appears to be essential to their confinement. It ensures the existence of three motion invariants, which are the magnetic moment $\mu = mv_\perp^2/2B$ which is an adiabatic invariant, with ϕ the electric potential and ψ the poloidal magnetic flux (see section 1.1.2), the energy $\mathcal{E} = mv_\parallel^2/2 + \mu B + e\phi$, and the toroidal kinetic canonical momentum $P_\varphi = e\psi + mRv_\varphi$ (with R the major radius and v_φ the toroidal velocity). In addition, the motion is characterized by three angles (i.e. periodic coordinates): the gyro-angle φ_c, and the two periodic directions θ and φ of the torus. In this case, the particle trajectories are integrable. Conversely, field lines which would be toroidal only would not allow for their confinement. Indeed, in such a case, particles would drift away from the field lines, approximately in the $\mathbf{B} \times \nabla\mathbf{B}$ direction (mostly vertical in tokamaks) at a speed typically ρ_* smaller than the thermal velocity $v_d \sim \rho_* v_{th}$. Furthermore, since this $\mathbf{v}_d$ drift depends on the particle charge, ions and electrons would drift in opposite directions. The resulting vertical electric field $\mathbf{E}$ would then push all the particles out of the domain due to the additional electric drift $\mathbf{v}_E = \mathbf{E} \times \mathbf{B}/B^2$.

From the plasma point of view as a whole, so to say, confinement results from a macroscopic MHD balance: the Lorentz force $\mathbf{j} \times \mathbf{B}$ ($\mathbf{j}$ being the plasma current density) opposes to the pressure gradient $\boldsymbol{\nabla} p$, which tends to push the plasma out of the toroidal volume:

$$\mathbf{j} \times \mathbf{B} = \boldsymbol{\nabla} p \tag{1.9}$$

Here, the only component of $\mathbf{j}$ which contributes to the MHD equilibrium is the diamagnetic current. As a matter of fact, the plasma *beta* parameter $\beta = p/(B^2/2\mu_0)$, defined as the ratio of the plasma pressure (or equivalently its thermal energy) p to the magnetic energy $B^2/2\mu_0$, with μ_0 the permeability of free space, is always smaller than unity (it actually hardly exceeds 10% because of MHD instabilities above a certain threshold).

The Grad-Shafranov equation exactly accounts for this macroscopic MHD balance in toroidal magnetic configurations. Projecting Ampère's law on the toroidal direction provides the toroidal component of the current. Considering the expression of the magnetic field in toroidal configurations, Eq. (1.6), leads to:

$$\begin{aligned}
\mu_0 j_\varphi / R &= (\boldsymbol{\nabla} \times \mathbf{B}).\boldsymbol{\nabla}\varphi \\
&= \left[\boldsymbol{\nabla} \times (\boldsymbol{\nabla}\psi \times \boldsymbol{\nabla}\varphi)\right].\boldsymbol{\nabla}\varphi \\
&= \boldsymbol{\nabla}.[(\boldsymbol{\nabla}\psi \times \boldsymbol{\nabla}\varphi) \times \boldsymbol{\nabla}\varphi] \qquad (1.10) \\
&= \boldsymbol{\nabla}.\left(-|\boldsymbol{\nabla}\varphi|^2 \boldsymbol{\nabla}\psi\right) = -\boldsymbol{\nabla}.\left(\frac{\boldsymbol{\nabla}\psi}{R^2}\right) \qquad (1.11)
\end{aligned}$$

The two components of the plasma current then read as follows:

$$\begin{aligned}
\mu_0 \mathbf{j}_\varphi &= -R^2 \boldsymbol{\nabla}.\left(\frac{\boldsymbol{\nabla}\psi}{R^2}\right)\boldsymbol{\nabla}\varphi \qquad (1.12) \\
\mu_0 \mathbf{j}_\theta &= \boldsymbol{\nabla} \times (F\boldsymbol{\nabla}\varphi) = F'\,\boldsymbol{\nabla}\psi \times \boldsymbol{\nabla}\varphi \qquad (1.13)
\end{aligned}$$

where the prime denotes derivative with respect to ψ: $F' \equiv dF/d\psi$. Injecting these previous expressions into Eq. (1.9) then leads to:

$$\begin{aligned}
\mathbf{j} \times \mathbf{B} &= \mathbf{j}_\varphi \times \mathbf{B}_\theta + \mathbf{j}_\theta \times \mathbf{B}_\varphi \\
&= -\frac{FF'}{\mu_0 R^2}\,\boldsymbol{\nabla}\psi - \boldsymbol{\nabla}.\left(\frac{\boldsymbol{\nabla}\psi}{\mu_0 R^2}\right)\,\boldsymbol{\nabla}\psi \\
&= p'\,\boldsymbol{\nabla}\psi
\end{aligned}$$

One finally obtains the Grad-Shafranov equation:

$$\Delta^*\psi + FF' + \mu_0 R^2 p' = 0 \qquad (1.14)$$

with $\Delta^*\psi \equiv -R^2\boldsymbol{\nabla}.(\boldsymbol{\nabla}\psi/R^2)$. This differential equation involving the poloidal flux function ψ provides the equilibrium dynamics for an axisymmetric system such as a tokamak. Solving this equation requires the knowledge of the flux functions $F(\psi)$ and $p(\psi)$, respectively associated to the plasma current profile and to the pressure profile.

1.2 Breaking the confinement: turbulence and MHD modes

Plasma confinement is not ideal in tokamaks. One can basically distinguish two classes of physical processes which lead to a degradation of the confinement: those breaking the conservation of at least one of the motion invariants $(\mathcal{E}, P_\varphi, \mu)$ without affecting significantly the magnetic equilibrium, and those leading to magnetic islands inside the LCFS. Electrostatic (and to a less extent electromagnetic) micro-turbulence and collisional transport belong to the first category: neither energy nor kinetic toroidal momentum are conserved in the turbulent state, while collisions lead to an increase of the entropy of the system. The second category contains the large spectrum of MHD instabilities. In this case, magnetic islands are usually created at low-order rational values[1] of the safety factor q. The growth of these islands can not only degrade the confinement by reducing the pressure gradient, but can even lead to disruptions, i.e. to the sudden and complete loss of confinement, such that all the energy stored in the plasma is released on the plasma facing components, and possibly on the whole surrounding wall, in a few hundreds of microseconds. A brief overview of some of the main characteristics of these two classes of physical processes is given in the following sub-sections.

1.2.1 Drift wave turbulence

From a general point of view (in contrast with the sometimes more restrictive understanding of this term), drift-wave (DW) turbulence refers to the saturated nonlinear regime of those instabilities where waves become unstable within the framework of *magnetized plasmas*, where the transverse motion of particles and fluid is governed by *velocity drifts*. In the fluid description, these drift velocities are the electric (or $E \times B$) drift $\mathbf{v}_E = \mathbf{E} \times \mathbf{B}/B^2$ and the diamagnetic drift $\mathbf{v}_{*s} = \mathbf{B} \times \boldsymbol{\nabla} p_s/e_s n_s B^2$, with s being the plasma species and e_s, p_s and n_s the Coulomb charge, the pressure and the density of the s-species respectively. Such a regime is encountered in plasmas where turbulence develops on much longer time scales than the cyclotron gyro-period $\omega_{cs}^{-1} = m_s/e_s B$. Within this framework, most of the cross-field turbulent transport is governed by the fluctuations of the electric drift velocity.

Among the DW instabilities, two main families can be distinguished: those already arising in the presence of a constant (both in magnitude and in direction) guiding magnetic field, and those relying on the existence of the magnetic field inhomogeneity. Obviously, both require the plasma to be out of thermodynamical equilibrium to develop, i.e. that there exist gradients (typically of density, pressure or temperature) in the system. The first branch develops as long as some mechanism leads to the existence of a phase shift between the electric potential fluctuations and those of the transport quantity (e.g. density or temperature). The second branch arises due to the curvature drift currents of oppositely charged species flowing in opposite directions. The model derived by Hasegawa and Wakatani [Hasegawa 1983] and the slab branch of the ITG (ion temperature gradient) driven turbulence both belong to the first class of DW instabilities. While

---

[1] Any rational number m/n can be recast in the form of a so-called continuous fraction: $m/n = a_1 + \frac{1}{a_2 + \frac{1}{a_3 + \frac{1}{\dots}}}$, with $a_i \in \mathbb{N}$. The rank k of the last term of the series $[a_1, a_2, ..., a_k]$ provides the order of the rational number m/n. For instance, $\frac{3}{2} = 1 + \frac{1}{2}$ is of order 2, while $\frac{11}{7} = 1 + \frac{1}{2 + \frac{1}{3}}$ is of order 3.

the phase shift is due to collisions in the HW model, it is due to Landau damping or parallel diffusivity in the slab ITG case. The latter case correspond to the model presently implemented in the FENICIA code, as discussed in Chapter 5. Relying on different classes of particles (ions or electrons, either passing or trapped in the magnetic wells), the toroidal branches of ITG and ETG modes, and also TEM (trapped electron modes) all belong to the second family of DW instabilities.

1.2.2 Tearing modes and magnetic islands

Magnetohydrodynamical (MHD) instabilities in the plasma can lead to the spontaneous appearance of usually large scale magnetic islands, such as those illustrated in Fig. 1.6. They break the simple nesting of the axisymmetric toroidal surfaces, hence the axisymmetry of the magnetic equilibrium. These islands form at surfaces with (usually low order) rational values of the safety factor q. They involve modes characterized by poloidal m and toroidal n wave numbers such that $q = -m/n$. These modes are *resonant* on this magnetic surface, in the sense that their parallel gradient vanishes there[2]. There, initially well-defined magnetic field lines break and reconnect to form a magnetic island. As illustrated in Figure 1.7, magnetic islands modify the topology of the magnetic equilibrium. The surface that separates the closed and open surfaces is called the *separatrix*. Its center defines the O-point, while X-points separate two adjacent O-points. The formation of magnetic islands is generally associated with resistive instabilities, particularly the so-called tearing modes (see below). The reason is that *ideal* MHD instabilities, which assume that the plasma is perfectly conducting (zero resistivity), are described within the framework of the ideal Ohm's law, which states that the sum of Lorentz and Coulomb forces is equal to zero: $\mathbf{E} + \mathbf{v} \times \mathbf{B} = \mathbf{0}$. In this case, the magnetic flux can be considered as frozen-in to the fluid, in the sense that it moves with the fluid (it can be shown that the magnetic flux through each surface moving with the fluid is constant). Conversely, *resistive* magnetic instabilities account for some finite resistivity η of the plasma, such that $\mathbf{E} + \mathbf{v} \times \mathbf{B} = \eta\mathbf{j}$, with $\mathbf{j}$ being the plasma current density. In this case, it is no longer forbidden that field lines cross over. As a matter of fact, since the plasma is not perfectly conducting, island formation can occur in the nonlinear regime of all MHD instabilities.

The tearing instability in a tokamak is driven by the radial gradient of the equilibrium toroidal current density. The name derives from the tearing and rejoining of magnetic field lines which occur during the instability as a consequence of finite resistivity [Wesson 2011]. At and in the neighborhood of the resonant surface for the mode, the Lorentz's force contribution to Ohm's law goes to zero, so that the $\eta\mathbf{j}$ term becomes important in balancing the induced electric field. In the nonlinear regime, tearing modes lead to magnetic islands. The growth of these islands is mainly determined by resistive diffusion.

---

[2] Indeed, considering a mode $\phi = \hat{\phi}(r,t)\exp\{i(m\theta + n\varphi)\} + cc$ (with cc the conjugate complex), then it comes, in the limit of large aspect ratio tokamaks ($R/a \gg 1$): $R\nabla_{\parallel}\phi = i(n + m/q)\hat{\phi} + cc$, which vanishes at r_{mn} such that $q(r_{mn}) = -m/n$

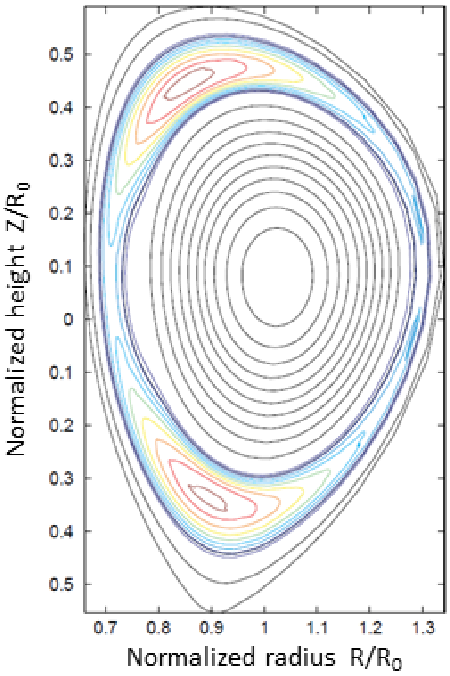

Figure 1.6: Simulation of a $(m, n) = (2, 1)$ neoclassical island in ITER, with m and n the poloidal and toroidal wave number, respectively [ITER physics basis, *Nucl. Fusion* **39** (1999) 2251, chapter 3].

The development of magnetic islands is particularly deleterious to the confinement for several reasons. First of all, the pressure tends to flatten inside the island as a result of the fast parallel transport, hence reducing the overall energy content of the plasma. Secondly, several magnetic islands located at different radial positions can overlap, leading to chaotic transport over large radial distances. Somewhat related is the possibility for these modes to lead to the too fast outward transport of energetic particles such as Helium ashes (alpha particles), possibly preventing them to deposit their energy into the bulk plasma before escaping the confined region. Last but not least, these islands may not saturate before reaching the boundary of the plasma, hence leading to the sudden loss of any confinement called a disruption.

A major concern is the study of the growth and the saturation mechanisms of magnetic islands in tokamaks. These issues are expected to depend on the interplay between the island and turbulence, which also affects both pressure and current transport. Nowadays, theoretical tools to study those phenomena are limited (see e.g. [Connor 1988, Cowley 1986]). In chapter 5, we attempt a numerical treatment of the effects of turbulence on resistive tearing modes using FENICIA.

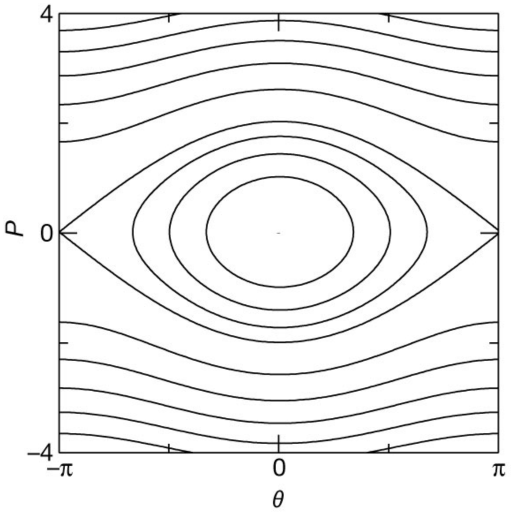

Figure 1.7: Schematic view of a magnetic island.

1.3 The anisotropy of transport in the plasma

A strongly magnetized high-temperature plasma is strongly anisotropic due to the presence of the magnetic field itself. Physically, this anisotropy is due to the fact that particles are relatively free to stream in the parallel direction, i.e. along the magnetic field lines, but exhibit gyro-orbits in the transverse direction to the magnetic field. In other words, it is a consequence of the rapid communication along the magnetic field lines (at the sound speed for electrostatic instabilities) and slow communication across the field lines (typically velocities across the field do not exceed the diamagnetic speed, which is about ρ_* smaller than the acoustic one). This property is inherent to the confinement principle in tokamaks: no upper constraint is put on plasma transport coefficients along the magnetic field $\mathbf{B}$. Instead, the aim behind confinement is to lower those coefficients in the direction transverse to $\mathbf{B}$. In addition, fluctuation measurements indicate a relatively short perpendicular correlation length ($\sim 5 - 10\rho_i$) [Fonck 1993, Mazzucato 1993], but a long parallel correlation length ($\sim qR$) [Zweben 1989].

An estimation of the parallel transport coefficient, dominated by collisions, for any ion or electron "α" species is given by

$$\chi_{\parallel} \approx \frac{v_{th}^2}{\nu_\alpha} \tag{1.15}$$

where v_{th} is the thermal velocity. The collision frequency ν_α, which typically scales like $\nu_\alpha \sim n_\alpha T_\alpha^{-3/2}$ (with n_α and T_α the density and temperatures of α species), is small in hot and rarefied plasmas such as tokamak plasmas. $\chi_{\parallel}$ is of the order of $10^9 \mathrm{m}^2.\mathrm{s}^{-1}$ for ions in typical fusion plasmas. Due to this fast parallel transport, fluid quantities such as density n, temperature T and current density $\mathbf{j}$, can be assumed at lowest order to be fairly constant on magnetic flux surfaces. Fluctuations are usually of order ρ_* smaller in the core confined plasma.

The perpendicular turbulent transport coefficient which governs the dynamics of the equilibrium profiles is governed by turbulence. It can be estimated by assuming it is of the order of the gyro-Bohm coefficient, namely

$$\chi_\perp \approx \rho_* \rho_\alpha^2 \omega_{c\alpha} \tag{1.16}$$

$\omega_{c\alpha}$ being the cyclotron frequency for a species α and ρ_* being the Larmor radius ρ_α normalized to the minor radius a. Consequently, the ratio of parallel transport to perpendicular transport coefficients writes

$$\frac{\chi_\parallel}{\chi_\perp} \sim \frac{\omega_{c\alpha}}{\rho_* \nu_\alpha} \tag{1.17}$$

For ITER-like tokamak parameters, ($\rho_* = 2.10^{-3}$, $\omega_{ci} \approx 10^8 s^{-1}$ and $\nu_i \approx 10^2 s^{-1}$). Considering ion transport, this leads to the following very large ratio of transport coefficients for equilibrium quantities:

$$\frac{\chi_\parallel}{\chi_\perp} \approx 10^9 \gg 1 \tag{1.18}$$

As far as turbulence is concerned, time dynamics is typically of the order of the ion diamagnetic frequency $\omega_{*i} \sim (k_\perp \rho_i) v_{thi}/L_T$, with L_T the temperature gradient length. It is equilibrated by parallel transport, either governed by $c_s k_\parallel$ (c_s being the sound speed) or $k_\parallel^2 \chi_\parallel$, depending on whether the plasma is weakly collisional or not, respectively. Here $k_\perp$ and $k_\parallel$ stand for typical wave vectors of turbulence in transverse and parallel directions, respectively. The most important direct result of the anisotropy of transport in strongly magnetized plasmas is that *turbulence has elongated structures along the magnetic field lines*[3]. Knowing that turbulence develops transverse scales of the order of the ion gyro-radius, $k_\perp \rho_i \sim 1$, the typical ratio between parallel and transverse correlation length of turbulent eddies is then given by:

$$\frac{k_\parallel}{k_\perp} \sim \frac{\rho_i}{qR} \ll 1$$

The ratio of the characteristic scales is typically of the order of ρ_*, which is expected to be equal to about 2.10^{-3} in ITER.

This important property leads to a considerable simplification to be gained in performing analysis or numerical solutions using a coordinate system aligned with the magnetic field. Indeed, in this case, one can then take benefit of the anisotropy to adopt a much smaller number of grid points in the parallel direction than in the transverse one, typically in the ratio $\rho_* a/R$. With a minimal necessary

---

[3] The fact that turbulent structures are much more elongated in the parallel direction than in the transverse one also results from the resonant character of wave-particle interactions in these weakly collisional plasmas. At leading order, the resonance condition takes the following form: $\omega = k_\parallel v_\parallel$, with ω the wave frequency. It turns out that micro plasma instabilities which develop in tokamaks are in the range $\omega \lesssim v_{th}/R$. Considering thermal resonating particles for which $v_\parallel \approx v_{th}$, it readily appears that the following inequality $k_\parallel R \lesssim 1$ has to be fulfilled for the resonance condition to be satisfied.

simulation mesh, the same physics can be tackled. As detailed in the next section, this is the primary motivation for developing a numerical approach which takes advantage of this anisotropy, which is the subject of this thesis.

1.4 Motivation and outline

1.4.1 Taking advantage of the plasma anisotropic transport

Tokamak plasma turbulence evolves from a large class of instabilities (such as, for instance, ion temperature gradient driven modes, trapped-electron modes and current and pressure driven MHD modes) that have a highly elongated mode structure along the equilibrium magnetic field. From the theoretical point of view, these instabilities are characterized by long parallel wavelengths, of the order of the system size ($\sim qR$) , and short perpendicular wavelengths of the order of the ion gyro-radius (ρ_i). Also, there is ample evidence from numerical simulations and experimental measurements [Fonck 1993, Zweben 1989] that the nonlinear (turbulent) regime is also characterized by gradients parallel to the magnetic field much smaller than the gradients in the perpendicular direction. As a consequence, from the numerical viewpoint, one can assume that the number of degrees of freedom necessary to describe the solution of a given model is substantially less than what it would be if the turbulence had small scales in all the directions. Especially, the grid mesh does not need to be of the order of the Larmor radius in all directions: it can be much larger in the parallel direction. Thus, one can conceive that much more efficient codes are made possible by a suitable choice of coordinates, that allow the smallest number of grid points in a certain direction. for this purpose, field-aligned coordinates have been employed for already a couple of decades in tokamak turbulence simulations [Cowley 1991, Hammett 1993, Dimits 1993, Scott 1998, Scott 2001]. The resulting gain in computational efficiency obtained by using this type of coordinates can be a couple of orders of magnitude for a turbulence simulation of a large device like ITER.

There are several potential difficulties of using field aligned coordinates for the numerical meshgrid. Among them, it is important to mention the fact that one looses at least one of the two natural periodic directions of the torus. But in practice, the important criterion is that parallel gradients are accurately computed even though fewer grid points are considered in a given direction. The approach developed in this thesis shows that it is indeed possible to reach such a target with different types of meshing which do not even need being related to flux functions. In addition, and most importantly, our approach allows one to deal with any kind of magnetic equilibrium, including the case of X-points configurations either in an axisymmetric divertor or across a magnetic island.

1.4.2 The general class of models

The second motivation for this thesis is to construct a numerical code capable of handling a very large class of models relevant to controlled magnetic fusion. Turbulent transport in tokamaks is studied via numerical simulations of a variety of model equations which retain the important physics one wants to study. A fairly general structure of model equations is given as follows:

$$\partial_t L \cdot S = E(S) + I \cdot S \tag{1.19}$$

where S is a structure of vectors representing the state of the system. $E(S)$ is a nonlinear operator that can be treated explicitly without much penalty. L and I represent linear operators such that the reduced problem obtained by setting $E(S) = 0$ could be treated implicitly. The splitting of the right hand side (r.h.s.) between E and I is by no means unique and depends on the physics to be studied. As a general rule, one aims at treating explicitly only the physics occurring at the timescale of interest for the specific problem. The main constraint with respect to a generic r.h.s. is that the implicit problem be linear. We further assume that L and I are time-independent. And boundary conditions are built into L beforehand.

This general structure includes a broad class of turbulence models ranging from the simple Hasegawa-Mima equation up to the fluid and kinetic equations. For instance, one can consider fluid and gyro-fluid equations, which have longly been used to gain insight into plasma instabilities and turbulence [Hammett 1993]. They provide the dynamics of a few moments (typically 4-6 moments, for density, parallel flow, parallel and perpendicular pressure, parallel and perpendicular heat flux, etc.) of the gyro-kinetic equation, expressing fundamental nonlinear conservation laws which the turbulence must satisfy. Closure approximations for the high order moments are made which provide improved fluid models of kinetic effects such as wave-particle resonances (Landau-damping and its inverse) [Hammett 1990, Hammett 1992, Sarazin 2009], gyro-radius orbit averaging [Dorland 1993b], and the dominant nonlinearities [Dorland 1993b]. An example of a typical gyro-fluid model can be found in [Dorland 1993a, Ottaviani 1999, M.A.Beer 1995]. Besides, one may also study within this general structure of models the drift-kinetic and gyro-kinetic equations which have also been widely used to investigate turbulence.

As for the splitting of the r.h.s. of Eq. (1.19) between $E(S)$ and I, we note that $E(S)$ would typically contain nonlinear terms such as the electric drift, possible parallel nonlinearities, linear terms related to the drift frequencies and source terms while I would typically account for perpendicular diffusive terms (either accounting for collisions or modeling turbulent transport) as well as linear terms pertaining to the parallel dynamics.

To highlight the main motivation, we exemplify the class of models (1.19) by considering the following normalized drift-wave model that one can get, for instance, from Eqs.(7-8) of the gyro-fluid model given in [Dorland 1993b] in the zero Larmor radius limit. It belongs to the general class of drift-wave models discussed just above. The ion temperature is kept as a constant. This model will be used to demonstrate the viability of the FCI approach in Chapter 4. It involves the linearized versions of both continuity and parallel momentum conservation equations:

$$\begin{cases} \partial_t n + [\phi, log(n_0)] + C_\parallel \nabla_\parallel u = 0 \\ \\ \partial_t u + \frac{1}{\tau} C_\parallel \nabla_\parallel n + C_\parallel \nabla_\parallel \phi = 0 \\ \\ n = \phi - \rho_*^2 \nabla_\perp^2 \phi \end{cases} \tag{1.20}$$

The last relationship derives from the quasi-neutrality condition, with the assumption that electrons respond adiabatically to the electric potential fluctuations. The last term accounts for the ion polarization density. Here n is the relative perturbed ion guiding center density, n_0 is the equilibrium density profile, u is the ion parallel velocity normalized to the thermal speed, and ϕ is the electrostatic potential normalized to T_e/e. Both transverse coordinates (x, y) involved in the Poisson bracket are normalized to the tokamak minor radius a. We define two dimensionless parameters: $C_\parallel = a/(\rho_* R)$ where R is the tokamak major radius, $\rho_* = \rho_s/a$ is the reduced gyro-radius with $\rho_s = (mT_e)^{1/2}/eB$ being the ion sound Larmor radius. Moreover τ is the ratio of electron temperature to ion temperature T_e/T_i. Time is normalized to the Bohm timescale $a^2/(\rho_s c_s)$, where $c_s = (T_e/m)^{1/2}$ is the ion sound speed. The explicit expression of the dimensionless parallel derivative operator $\nabla_\parallel$ depends on the magnetic field structure. In the case of a cylindrical geometry one can write $\nabla_\parallel = \partial_\phi + 1/q(r)\, \partial_\theta$ with (r, θ) the polar coordinates in the poloidal plane and $q(r)$ the safety factor.

Writing this system in the same form as (1.19) yields

$$\partial_t \begin{vmatrix} 1 - \rho_*^2 \nabla_\perp^2 & -1 & 0 \\ 0 & 1 & 0 \\ 0 & 0 & 1 \end{vmatrix} \begin{vmatrix} \phi \\ n \\ u \end{vmatrix} = \begin{vmatrix} 0 \\ -[\phi, log(n_0)] \\ 0 \end{vmatrix} - \begin{vmatrix} 0 & 0 & 0 \\ 0 & 0 & C_\parallel \nabla_\parallel \\ C_\parallel \nabla_\parallel & \frac{1}{\tau} C_\parallel \nabla_\parallel & 0 \end{vmatrix} \begin{vmatrix} \phi \\ n \\ u \end{vmatrix} \tag{1.21}$$

It follows from the latter form of the system that solving the equations often requires the computation of $\nabla_\parallel$ while constructing the matrix-vector product $I.S$. A challenging numerical task is thus to implement parallel derivatives with minimal numerical dissipation and minimal number of points. It turns out that employing a coordinate system for nonlinear simulations where coordinates are aligned with the magnetic field lines is computationally more efficient. Those are called “field-aligned coordinate systems". In the next chapter, we review the different approaches to field-aligned coordinates that have been developed in the last two decades and the advantages of using them in turbulence codes.

1.4.3 Outline

Field-aligned coordinates employed so far are derived from predefined flux coordinates. In this Thesis, a new flux-independent field-aligned coordinate system that I refer to as the FCI (Flux Coordinate Independent) approach is presented. The method employs standard Cartesian coordinates, such that poloidal derivatives are computed in the original Cartesian frame, but parallel derivatives are computed directly along the local field line.

In Chapter 2, I give a historical overview on all the field-aligned coordinate approaches that have been employed so far. The new method is shown to have a number of advantages over earlier approaches [Hariri 2013], allowing for more flexible coding and coping with tokamak X-point magnetic geometries, a situation that can not be handled by conventional approaches.

Chapter 3 contains a detailed description on the implementation of the FCI approach into a new nonlinear 3D code that I have developed from scratch during the course of this Thesis and I have called FENICIA. The code solves the general class of plasma models (1.19), thus allowing one to simultaneously tackle a wide range of physics problems. The code is furthermore designed to be flexible and easily adaptable to many magnetic geometries.

Several numerical tests carried out with FENICIA are described in Chapter 4 to qualify both the new method and the code, using various models belonging to Eq. (1.19). More precisely, the accuracy of the approach is tested in particular with respect to the question of spurious radial transport, an obvious concern when abandoning flux coordinates. In this regard, I show that numerical radial diffusion can be easily kept under control with the choice of suitable algorithms, at a minimal computational cost. The contribution of the parallel dynamics to the overall error is shown to be negligible. In addition, the numerical method's accuracy is detailed in the linear regime where I demonstrate that the numerical growth rate and rotational frequency match the values predicted by theory.

In Chapter 5, simulations in the nonlinear turbulent regime allow one to recover, at reduced numerical cost, the standard features of slab ITG turbulence. A study of the linear instability's threshold and growth rate is investigated. Thereafter, I demonstrate the strength of the approach by showing a convergence test on a 3D model for Ion Temperature Gradient (ITG) driven turbulence which proves that the method is well suited to minimize the number of degrees of freedom needed to treat a given problem in an accurate and efficient manner. Unlike elder approaches, the FCI approach can be extended to deal with X-point configurations such as magnetic islands. To finish, I subsequently show that this approach can indeed be applied to an X-point geometry in any modular tokamak simulation code and I show its robustness in very demanding cases. In this instance, I consider a magnetic configuration with an island and a separatrix and I perform tests on a sound wave propagation problem. Analytical solutions are constructed both inside and outside the island. I first show that the numerical results are in good agreement with the exact solutions. Then, I carry out a study of an initial perturbation sitting across the X-point of the island in a numerically demanding situation. Since there is no analytic solution in this case, I perform convergence studies and I verify the adequate conservation properties.

Chapter 2

A General Overview on Field-Aligned Coordinate Systems

أَعَزُّ مَكَانٍ في الدُّنَى سَرجُ سَابِحٍ

وَ خَيرُ جَليسٍ في الزَّمَانِ كِتَابُ

أَبو الطَّيِّب المُتَنَبّي (٩١٥ - ٩٦٥)

Contents

Acrylique, (F. Hariri, 2006)

Field-aligned coordinates are necessary to optimize plasma turbulence codes. It's widely employed in today's codes allowing the number of grid points needed to represent structures elongated along the magnetic field to be greatly reduced compared with traditional coordinate systems as shown in Fig. 2.1. The main idea is that one of the coordinates be aligned along the magnetic field as illustrated in Fig. 2.1. The coordinate φ is transformed onto s in the new field-aligned system.

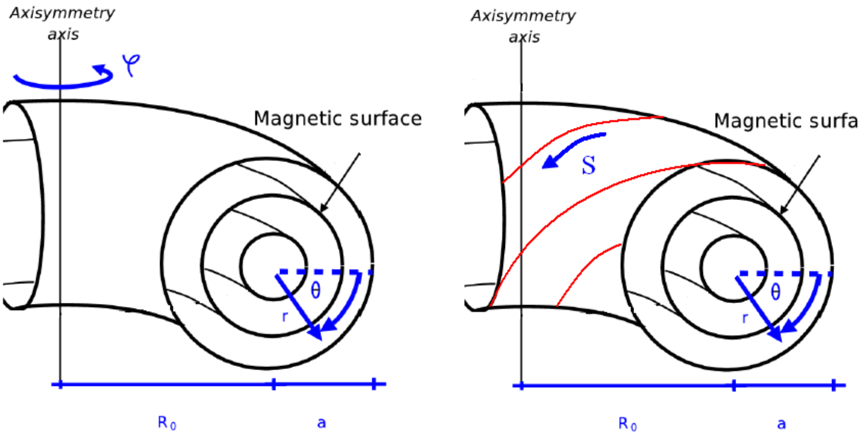

(a) (b)

Figure 2.1: (a) Conventional coordinate systems; (b) field-aligned coordinate systems

In this chapter, I give a historical review on two-dimensional field-aligned coordinate techniques that have been used so far, with their respective advantages and drawbacks. In the last part, I introduce a new three-dimensional Flux Coordinate Independent (FCI) field-aligned approach that will be considered throughout this thesis.

2.1 Review

In this section, we review the different approaches to field-aligned coordinate systems that have been implemented in present codes. Polar coordinates (r, θ, φ) in cylindrical geometry are used for simplicity.

In general, the procedure consists of **a.** dividing the simulation domain (either a given magnetic surface or the whole toroidal manifold) into suitable blocks; **b.** for each block, finding a coordinate transformation from the original system, e.g. (R, Z, φ), to a new system where one of the coordinates (s) is such that $\nabla_{\|} \propto \partial/\partial s$; and **c.** using a suitable numerical implementation. Typically, one employs finite differences in s for fluid codes and also integration of $\partial f/\partial t + \partial f/\partial s = 0$ along the characteristics in the s direction for kinetic codes.

2.1.1 S. Cowley 1991

Historically, coordinate transformations were in 2D, on given magnetic surfaces. The first implementation of field-aligned coordinates in a plasma turbulence code can be traced back to thinking in the early nineties [Cowley 1991] that led to Ref. [Hammett 1993, Beer 1995] in which the following transformation is considered:

$$\left\{\begin{array}{ll} \xi & = \varphi - q(r)\,\theta \\ s & = \theta \\ \rho & = r \end{array}\right. \tag{2.1}$$

Here ρ determines a flux surface, ξ determines a magnetic field line and θ labels a position along the field lines. The magnetic surface corresponding to this type of transformations is illustrated below in Fig. 2.2 where φ is the toroidal angle shown in the abscissa and θ is the poloidal angle shown in the ordinate. Derivatives with respect to the original variables are given by

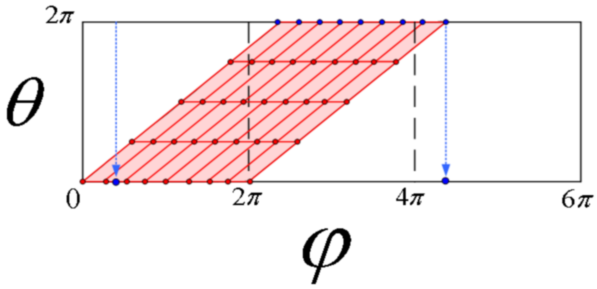

Figure 2.2: Field lines corresponding to the magnetic field direction on a given magnetic surface (θ, φ).

$$\begin{aligned} \frac{\partial}{\partial r} &= \frac{\partial}{\partial \rho} - q\prime(r)\,\theta\,\frac{\partial}{\partial \xi} \\ \frac{\partial}{\partial \varphi} &= \frac{\partial}{\partial \xi} \\ \frac{\partial}{\partial \theta} &= \frac{\partial}{\partial s} - q(r)\,\frac{\partial}{\partial \xi} \end{aligned} \tag{2.2}$$

while the parallel derivative is given by

$$R\,\nabla_{\|} = \frac{1}{q(r)}\,\frac{\partial}{\partial s}. \tag{2.3}$$

Since the parallel variable is coarse, in this representation, on any given flux surface, all the information on the fine structure of turbulence is necessarily carried by the toroidal angle φ. This coordinate transformation, as it is, has some drawbacks. **(a)** First, one notices that the new coordinate s is not periodic. Care must be taken, when setting boundary conditions at the end points of an s line, that the original double-periodicity of the given magnetic surface is enforced. Non-compliance with this constraint would lead to spurious solutions and dubious results [Scott 1998, Ottaviani 2011]. **(b)** The second problem is the consequence of the term, proportional to θ, appearing in the expression of the radial derivative in Eq. (2.2). This term, familiar from the ballooning transformation, leads to mixed-derivatives of increasing weight as one moves away from $\theta = 0$, when computing certain operators, such as the Laplacian. These terms are the consequence of θ-dependent non-diagonal metric coefficients in the new coordinate system. Although mathematically correct, they pose a numerical challenge since their numerical treatment can introduce artificial inhomogeneities in the poloidal direction even for systems possessing poloidal symmetry [Ottaviani 2011]. **(c)** A third problem is in the actual code implementation, where the derivative along s is usually dropped from the poloidal derivative expression, thus approximating it by $\partial/\partial\theta \approx -q(r)\,\partial/\partial\xi$. **(d)** The last problem with this coordinate transformation is that $R\,\nabla_{\|} = 1/q(r)\,\partial_s$ which means that it cannot deal with the separatrix, since there the safety factor becomes infinite. In other words, in the expression of ξ, the term proportional to θ dominates as $q \longrightarrow \infty$, thus leading the two coordinates ξ and s to merge and become identical. In that case, their respective orientation vectors turn out to be almost aligned at a given magnetic surface (a constant r value). That is: $\boldsymbol{\nabla}\xi|_r = \boldsymbol{\nabla}\varphi - q\,\boldsymbol{\nabla}\theta \propto \boldsymbol{\nabla}s$.

One can see that transformation (2.2) is equivalent to the ballooning transformation [Connor 1979], as already remarked in [Kim 1994]. Indeed it seems that when dealing with linear analytic theory, the possibility of exploiting a ballooning-type (WKB) approximation turns out to be a clear advantage of this approach.

2.1.2 B. Scott 2001

The second approach was introduced in Ref. [Scott 2001]. The key difference with respect to the first approach is the use of the so-called shifted-metric technique. It consists in sectioning the toroidal manifold given by the magnetic surface into a number of parts, N_θ, each having its own coordinate system, differing one from the other by a shift in the origin as follows:

$$\begin{cases} \xi &= \varphi - q(r)\,(\theta - \theta_k) \\ s &= (\theta - \theta_k) \\ \rho &= r \end{cases} \tag{2.4}$$

The parallel direction is still labeled by the poloidal angle θ, but it integrates the shifted-metric technique. Figure 2.3 illustrates the division of the poloidal manifold into k sectors, where $\theta_k = k\,\Delta\theta$ with $\Delta\theta = 2\pi/N_\theta$ and $k = 0, N_\theta - 1$. A given sector is defined by quadrangles such that $0 \leq \varphi \leq 2\pi$ and $\theta_k \leq \theta \leq \theta_k + \Delta\theta$. Derivatives with respect to the original variables are now given by

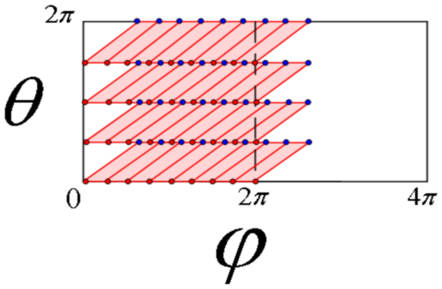

Figure 2.3: The shifted metric coordinate system chooses these shifts such that the coordinate system is orthogonal at a particular value of θ_k. At each θ_k, one is on a different coordinate system, but each of them is still field aligned.

$$\begin{aligned} \frac{\partial}{\partial r} &= \frac{\partial}{\partial \rho} - q\prime(r)\,(\theta - \theta_k)\,\frac{\partial}{\partial \xi} \\ \frac{\partial}{\partial \varphi} &= \frac{\partial}{\partial \xi} \\ \frac{\partial}{\partial \theta} &= \frac{\partial}{\partial s} - q(r)\,\frac{\partial}{\partial \xi} \end{aligned} \tag{2.5}$$

The main progress achieved by using this approach can be summarized by the following. One observes that operations are now performed on an orthogonal grid as a result of the shifted-metric technique and spurious effects from magnetic shear are removed since for each poloidal sector k, the additional term that leads to metric distortion vanishes at $\theta = \theta_k$ giving $\partial_r = \partial_\rho$. Thus problem **(b)** of the first approach (2.1) is solved. Problem **(a)** is less harmful by splitting the interpolation equally at sub-domain boundaries instead of having it localized on the manifold ends. Notice that the accuracy needed to compute the values of a function at the interpolation points is automatically assured by the high resolution needed to describe a function on a given $s_k = 0$ line. Problems **(c)** and **(d)** are still a drawback of this approach.

2.1.3 M. Ottaviani 2011

Later, a third approach was suggested in Ref. [Ottaviani 2011]. The key observation of this approach is that, as a consequence of the flute property, one can lower the resolution in any chosen direction, provided that enough information on the fine structure of the turbulent fields can be carried by the variation in any other direction. One then realizes that there is just another alternative to this meshing, which preserves the good property of double periodicity. It is given by switching the roles of coarse/fine mesh between the poloidal/toroidal angles. The author in [Ottaviani 2011] introduces a new way of labeling the position along a field line by its toroidal angle instead of the poloidal angle. This approach retains the advantages of the second approach and differs only by interchanging the role of the toroidal/poloidal angles.

This latter choice has a coarse toroidal grid. This implies that it is now the toroidal angle that must be used to describe variations along the field lines. This can be justified mathematically by sectioning the toroidal manifold in N_φ overlapping toroidal sectors, each with its own set of field-aligned coordinates given by the family of transformations:

$$\begin{cases} \xi &= \theta - \frac{1}{q(r)}\left(\varphi - \varphi_k\right) \\ s &= \left(\varphi - \varphi_k\right) \\ \rho &= r \end{cases} \tag{2.6}$$

where $\varphi_k = k\,\Delta\varphi$ with $\Delta\varphi = 2\pi/N_\varphi$ and $k = 0, N_\varphi - 1$. Here a given sector is defined by quadrangles such that $0 \le \theta \le 2\pi$ and $\varphi_k - \Delta\varphi \le \varphi \le \varphi_k + \Delta\varphi$. Figure 2.4 illustrates the new way of tracing the field lines, retaining the advantages of the shifted-metric technique, but interchanging the role of the angles. Derivatives with respect to the original variables are now given by

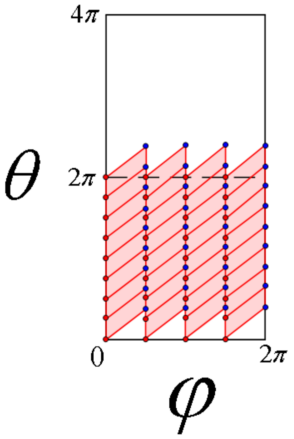

Figure 2.4: The third schematic of a magnetic surface where the number of points is reduced in the toroidal direction rather than the poloidal direction

$$\begin{aligned} \frac{\partial}{\partial r} &= \frac{\partial}{\partial \rho} - \frac{q\prime(r)}{q^2(r)}\left(\varphi - \varphi_k\right)\frac{\partial}{\partial \xi} \\ \frac{\partial}{\partial \varphi} &= \frac{\partial}{\partial s} - \frac{1}{q(r)}\frac{\partial}{\partial \xi} \\ \frac{\partial}{\partial \theta} &= \frac{\partial}{\partial \xi} \end{aligned} \tag{2.7}$$

whereas the parallel derivative is now simply given by

$$R\,\nabla_\parallel = \frac{\partial}{\partial s}. \tag{2.8}$$

This new system has additional advantages. Problem **(c)** common to the first and the second approach is solved because the poloidal derivative ∂_θ becomes exactly equal to ∂_ξ. Furthermore, problem **(d)** is solved simply because $\nabla_\parallel = \partial/\partial s$, so there is no more difficulty dealing with the region around the magnetic axis. This is due to the fact the two coordinates ξ and s become respectively equal to θ and $(\varphi - \varphi_k)$ as $q \longrightarrow \infty$, and no longer reduce to a single coordinate as was the case in the transformations discussed in sections. 2.1.2 and 2.1.1.

2.2 The Flux-Coordinate Independent (FCI) Approach

The last approach of Sec. 2.1.3 represents a substantial step forward. It separates the coordinate needed to label a position along a field line (φ), from the coordinates needed to describe a given function in the poloidal plane (r, θ). In order to fully describe a given field, of the type occurring in plasma turbulence models, one needs high resolution in any given poloidal plane, but only a small number of these planes. The parallel derivative is then computed in one go, by using values at the end points of arcs of magnetic field lines. This generically requires interpolating in the poloidal plane, since, usually, end points are not grid nodes. Accuracy of the interpolation operation would constrain the resolution in the poloidal planes to be adequately high, but one needs high resolution anyway, in order to keep the necessary information on the fine structure and to carry out the operations in the poloidal plane to a satisfactory accuracy. Thus, the need to use interpolation for the parallel operations does not introduce substantial constraints, and indeed one can anticipate that the tests of Chapter 4 indicate that the poloidal operations, and not parallel operations, are the main source of error in common situations.

The approach of Sec. 2.1.3 still relies on flux coordinates, for instance (r, θ). This section sketches how the field-aligned coordinates approach can be constructed in a way that avoids the use of flux coordinates to discretize the fields in the poloidal plane. Instead, the fields are discretized on a given grid related to the laboratory reference frame. For a tokamak, these are the usual (R, Z, φ) cylindrical coordinates such that Z is the direction of the torus symmetry axis, R the distance from the axis and φ the toroidal angle. We refer to this method as FCI (Flux-Coordinate Independent) approach [Hariri 2013].

Although the final result will be found fairly intuitive, at least in the context of cylindrical geometry, we prefer to proceed in a formal manner. This ensures that the approach is mathematically sound and prepares the way to extensions to more general situations and geometries.

2.2.1 Generic 2D coordinate transformations, straight geometry

One considers a class of static low-β equilibria, such that the suitably normalized axisymmetric magnetic field is given by

$$\mathbf{B} = \mathbf{b}(\mathbf{x}) + \hat{\mathbf{z}} \tag{2.9}$$

where one employs a three dimensional Cartesian reference system (x, y, z) such that $\hat{\mathbf{z}}$ is the direction of the magnetic axis, the main magnetic field along z is constant and normalized to unity, and $\mathbf{b}(\mathbf{x})$ is the poloidal magnetic field in the poloidal plane (x, y). The vector $\mathbf{x}$ indicates the position in this plane. The poloidal field can be written in terms of a flux function $\psi(\mathbf{x})$ such that

$$\mathbf{b} = \boldsymbol{\nabla} \times (\psi\hat{\mathbf{z}}) \tag{2.10}$$

Magnetic surfaces can be labeled by the value of ψ. Both closed and open field lines can be treated. The parallel derivative operator is given by

$$\nabla_{\|} = \mathbf{b}\,.\,\boldsymbol{\nabla} + \partial/\partial z \tag{2.11}$$

One has to look for a change of coordinates from the original (x, y, z) to a new set (ξ^{α}, s) such that s can be treated as a slowly-varying coordinate and only the two ξ^{α} $(\alpha = 1, 2)$ carry the information on the small scales. Taking advantage from what was learned in the previous sections, one divides the domain in a certain number of sectors centered around z_k, and extending to the boundary in the (x, y) directions, with k labeling a given sector. One then considers a set of transformations of the form:

$$\begin{cases} \xi^{\alpha} & = V^{\alpha}(\mathbf{x}) + C^{\alpha}(\mathbf{x})(z - z_k) \\ s & = z - z_k \end{cases} \tag{2.12}$$

where $V^{\alpha}(\mathbf{x})$ and $C^{\alpha}(\mathbf{x})$ are yet unknown functions. Derivatives with respect to the original variables, (x, y, z), are now given by

$$\begin{aligned} \frac{\partial}{\partial x^{\alpha}} &= \frac{\partial V^{\beta}}{\partial x^{\alpha}}\frac{\partial}{\partial \xi^{\beta}} + \frac{\partial C^{\beta}}{\partial x^{\alpha}}(z - z_k)\frac{\partial}{\partial \xi^{\beta}} \\ \frac{\partial}{\partial z} &= C^{\alpha}\frac{\partial}{\partial \xi^{\alpha}} + \frac{\partial}{\partial s} \end{aligned} \tag{2.13}$$

In terms of the new variables the parallel derivative is given by

$$\nabla_{\|} = b^{\alpha}\frac{\partial V^{\beta}}{\partial x^{\alpha}}\frac{\partial}{\partial \xi^{\beta}} + (z - z_k)\,b^{\alpha}\frac{\partial C^{\beta}}{\partial x^{\alpha}}\frac{\partial}{\partial \xi^{\beta}} + C^{\beta}\frac{\partial}{\partial \xi^{\beta}} + \frac{\partial}{\partial s} \tag{2.14}$$

In order to get $\nabla_{\|} = \partial/\partial s$ and eliminate the fast-varying derivatives, one has to satisfy the conditions:

$$C^{\alpha} = -b^{\beta}\frac{\partial V^{\alpha}}{\partial x^{\beta}} \tag{2.15}$$

$$b^{\alpha}\frac{\partial C^{\beta}}{\partial x^{\alpha}} = 0 \tag{2.16}$$

Knowing that

$$b^{x} = \frac{\partial\psi}{\partial y} \tag{2.17}$$

$$b^{y} = \frac{-\partial\psi}{\partial x} \tag{2.18}$$

and that for any function A,

$$[\psi, A] = \frac{\partial \psi}{\partial x}\frac{\partial A}{\partial y} - \frac{\partial \psi}{\partial y}\frac{\partial A}{\partial x}, \tag{2.19}$$

Hence, the Poisson bracket notation is used such that the following operation is satisfied:

$$b^\alpha \frac{\partial A}{\partial x^\alpha} \equiv -[\psi, A], \tag{2.20}$$

Eqs. (2.15-2.16) can then be written as

$$[\psi, [\psi, V^\alpha]] = 0, \tag{2.21}$$

where $C^\alpha = [\psi, V^\alpha]$.

Conjecture:

A general solution of Eq. (2.21) is

$$V^\alpha = f^\alpha(\psi) + g^\alpha(\psi)\,\chi(x, y), \tag{2.22}$$

where f^α and g^α are arbitrary functions of ψ, and $\chi(x, y)$ is a function chosen such that

$$[\psi, \chi] = 1, \tag{2.23}$$

whose solution can be found with the method of characteristics. $\chi(x, y)$ identifies the position on $\psi = \mathrm{const}$ surfaces and plays the role of a poloidal angle. Note that the Poisson bracket in (2.23) is equal to 1 for simplicity (see proof below).

- **Proof:** Let $V^\alpha = f^\alpha(\psi) + g^\alpha(\psi)\,\chi(x, y)$, then

$$[\psi, V^\alpha] = \frac{\partial \psi}{\partial x}\frac{\partial (f^\alpha + g^\alpha\,\chi)}{\partial y} - \frac{\partial \psi}{\partial y}\frac{\partial (f^\alpha + g^\alpha\,\chi)}{\partial x}, \tag{2.24}$$

Using the chain rule one gets

$$\begin{aligned}
[\psi, f(\psi)] &= \frac{\partial \psi}{\partial x}\frac{\partial f(\psi)}{\partial y} - \frac{\partial \psi}{\partial y}\frac{\partial f(\psi)}{\partial x}, && (2.25)\\
&= \frac{\partial \psi}{\partial x}\frac{\partial f(\psi)}{\partial \psi}\frac{\partial \psi}{\partial y} - \frac{\partial \psi}{\partial y}\frac{\partial f(\psi)}{\partial \psi}\frac{\partial \psi}{\partial x} && (2.26)\\
&= 0 && (2.27)
\end{aligned}$$

Similarly, $[\psi, g(\psi)] = 0$. This leads to

$$\begin{aligned}
[\psi, V^\alpha] &= [\psi, f(\psi)] + g(\psi)\,[\psi, \chi] + \chi\,[\psi, g(\psi)] && (2.28)\\
&= g(\psi)\,[\psi, \chi] && (2.29)
\end{aligned}$$

Recall that $[\psi, \chi]$ may be a constant or a function of ψ, but for simplicity, χ is chosen here such that $[\psi, \chi] = 1$, yielding

$$[\psi, V^\alpha] = g(\psi) \tag{2.30}$$

Therefore,

$$[\psi, [\psi, V^\alpha]] = [\psi, g(\psi)] \tag{2.31}$$
$$= 0 \tag{2.32}$$

Thus, V^α in Eq. (2.22) is a general solution to Eq. (2.21) such that the parallel gradient computed at fixed ξ^α reduces to

$$\nabla_\parallel = \frac{\partial}{\partial s}.$$

Consequently,

$$C^\alpha(\mathbf{x}) = [\psi, V^\alpha] = g^\alpha(\psi). \tag{2.33}$$

The system 2.12 then writes

$$\begin{cases} \xi^\alpha & = f^\alpha(\psi) + g^\alpha(\psi)\,\chi(x,y) + g^\alpha(\psi)(z - z_k) \\ s & = z - z_k \end{cases} \tag{2.34}$$

Discretization of $\nabla_\parallel$ using the FCI approach

In practice, one defines any field at nodes in the Cartesian (x, y, z) grid. Derivatives in the poloidal plane are computed in this reference frame by holding z constant without performing any coordinate transformation. Knowledge of the magnetic field geometry and performing the FCI transformation is only needed for the implementation of the parallel derivative. This depends on the scheme of choice. In order to compute the parallel derivative by finite differences, one has to use function values at points $(\mathbf{x}{+}\Delta\mathbf{x}, z_k{+}\Delta z)$ corresponding to a given increment Δs along s. This means finding end points along field lines for a given displacement Δz along z. From the set of equations (2.12), and knowing that $\xi^\alpha = cst$, one finds the following finite difference equations for the unknown increments $\Delta\mathbf{x}$:

$$[f^\alpha(\psi) + g^\alpha(\psi)\chi(\mathbf{x})]_{\mathbf{x}+\Delta\mathbf{x}} + [g^\alpha(\psi)]_{\mathbf{x}+\Delta\mathbf{x}}\Delta z = [f^\alpha(\psi) + g^\alpha(\psi)\chi(\mathbf{x})]_{\mathbf{x}} \tag{2.35}$$

But on a field line, the following condition is satisfied

$$\psi(\mathbf{x} + \Delta\mathbf{x}) = \psi(\mathbf{x}) \tag{2.36}$$

It follows that $f(\psi(\mathbf{x} + \Delta\mathbf{x})) = f(\mathbf{x})$ and $g(\psi(\mathbf{x} + \Delta\mathbf{x})) = g(\mathbf{x})$.

Consequently, from Eq. (2.35) one gets the following constraint

$$\chi(\mathbf{x} + \Delta\mathbf{x}) = \chi(\mathbf{x}) - \Delta z. \tag{2.37}$$

Thus end points for FD computations are obtained by moving along field lines for a given increment along z.

Conjecture:

Assuming $b^z = 1$, computing the map from ψ reduces to solving the following system of differential equations for the set of unknowns Δx, Δy and Δz an increment taken along the magnetic field line:

$$\begin{cases} \dfrac{dx}{dz} & = b^x = \partial_y \psi \\ \\ \dfrac{dy}{dz} & = b^y = -\partial_x \psi \end{cases} \tag{2.38}$$

• **Proof:** Let $\mathbf{x}(z) = \mathbf{x}_0 + \Delta\mathbf{x}(z)$ and $z_k \le z \le z_k + \Delta z$. Equations (2.36) and (2.37) equivalently write

$$\psi[\mathbf{x}(z)] = \psi(\mathbf{x}_0) \tag{2.39}$$

$$\chi[\mathbf{x}(z)] = \chi(\mathbf{x}_0) - z \tag{2.40}$$

Differentiating the latter system of equations yields

$$\frac{d\mathbf{x}}{dz} \cdot \boldsymbol{\nabla}_{\mathbf{x}} \psi = 0 \tag{2.41}$$

$$\frac{d\mathbf{x}}{dz} \cdot \boldsymbol{\nabla}_{\mathbf{x}} \chi = -1 \tag{2.42}$$

One can equivalently write

$$\frac{dx}{dz}\,\partial_x \psi + \frac{dy}{dz}\,\partial_y \psi = 0 \tag{2.43}$$

$$\frac{dx}{dz}\,\partial_x \chi + \frac{dy}{dz}\,\partial_y \chi = -1 \tag{2.44}$$

From (2.43) one gets

$$\frac{dy}{dz} = -\frac{dx}{dz}\,\frac{\partial_x \psi}{\partial_y \psi} \tag{2.45}$$

Putting Eq. (2.45) into Eq. (2.44) yields

$$\frac{dx}{dz}\,\partial_x \chi - \frac{dx}{dz}\,\frac{\partial_x \psi\,\partial_y \chi}{\partial_y \psi} = -1 \tag{2.46}$$

Using condition Eq. (2.23), one finally gets

$$\frac{dx}{dz}\,\partial_x \chi - \frac{dx}{dz}\,\frac{\partial_x \chi\,\partial_y \psi + 1}{\partial_y \psi} = -1 \tag{2.47}$$

from which one obtains the field-line equations:

$$\begin{cases} \dfrac{dx}{dz} & = \partial_y \psi \\ \\ \dfrac{dy}{dz} & = -\partial_x \psi \end{cases} \tag{2.48}$$

Given a certain magnetic equilibrium defining ψ, it is then possible to calculate the unknown displacements Δx and Δy for a given displacement Δz along the field line using $\boldsymbol{\nabla}\psi$. Practically, Δx and Δy are obtained bt integrating along the field lines (2.48) from $(x, y, z) = (x_0, y_0, z_k)$ to $(x, y, z) = (x_0+\Delta x, y_0+\Delta y, z_k+\Delta z)$.

This method gives the coordinates of a point that follows the field lines. However, as shown in Fig. 2.5, this point is not necessarily a node of the given mesh. Consequently, computation of parallel derivatives by finite differences require interpolation at end points of each field line. The interpolation technique and its implementation into a new code will be discussed in details in Chapter 3.

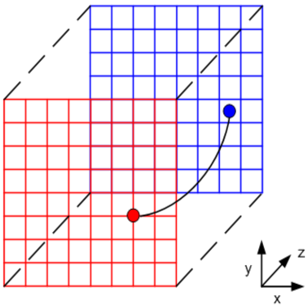

Figure 2.5: A grid showing the path of a point going from one poloidal plane to the next one. It does not necessarily hit a node of the next plane.

Special case, cylindrical geometry

The usual cylindrical geometry can be recovered by taking $\psi = \psi(r)$ with $r = (x^2 + y^2)^{1/2}$ and with the magnetic axis located at $x = 0, y = 0$. The solution of Eq. (2.23) is obviously $\chi \propto \arctan(y/x)$ where χ is proportional to the usual poloidal angle, via the safety factor. The ultimate goal is to solve for the vector $\boldsymbol{\Delta}\mathbf{x}$ for a given Δz using Eq. (2.37).
Let $\chi = h(\psi)\arctan(y/x)$ and solve for $[\psi, \chi] = 1$:

$$\iff h(\psi)\left[\psi(r), \arctan\left(\frac{y}{x}\right)\right] = 1 \tag{2.49}$$

$$\iff h(\psi)\partial_r\psi(r)\left[r, \arctan\left(\frac{y}{x}\right)\right] = 1 \tag{2.50}$$

$$\iff h(\psi) = \frac{r}{\partial_r\psi(r)} \tag{2.51}$$

Knowing that the poloidal magnetic field is defined as

$$\mathbf{b} = \boldsymbol{\nabla} \times (\psi\hat{\mathbf{z}}) \tag{2.52}$$

$$= -\partial_r\psi(r) \tag{2.53}$$

and that $B^z = 1$, the expression of the safety factor writes

$$\begin{aligned} q &= \frac{rB^z}{||\mathbf{b}||} && (2.54) \\ &= \frac{-r}{\partial_r \psi(r)} && (2.55) \end{aligned}$$

So

$$h(\psi) = -q. \tag{2.56}$$

Eq. (2.37) can then be rewritten as

$$\arctan\left(\frac{y + \Delta y}{x + \Delta x}\right) = \arctan\left(\frac{y}{x}\right) - \frac{\Delta z}{q} \tag{2.57}$$

where

$$\begin{aligned} x + \Delta x &= r\cos(\theta + \Delta\theta) && (2.58) \\ y + \Delta y &= r\sin(\theta + \Delta\theta) && (2.59) \\ \theta + \Delta\theta &= \arctan\left(\frac{y + \Delta y}{x + \Delta x}\right) && (2.60) \end{aligned}$$

From Eq. (2.60) one gets

$$\Delta\theta = \frac{-\Delta z}{q} \tag{2.61}$$

Leading to the following final map for a given increment Δz:

$$\begin{cases} x + \Delta x & = x\cos(\Delta z/q) - y\sin(\Delta z/q) \\ y + \Delta y & = y\cos(\Delta z/q) + x\sin(\Delta z/q) \end{cases} \tag{2.62}$$

Special case, X-point configuration

As an example of an X-point configuration one can assume $\psi = \psi_0(x) + A\cos(k_y y)$. If ψ_0 has an extremum at $x = 0$, A is not too big and a k_y is chosen judiciously, one gets a configuration used in magnetic island theory. The angle χ is obtained in terms of elliptic functions by solving numerically Eqs. (2.38) and (2.38).

2.2.2 3D coordinate transformations

Consider, as before, a magnetic field given by

$$\mathbf{B} = \boldsymbol{\nabla} \times (\psi\hat{\mathbf{z}}) + \hat{\mathbf{z}} \tag{2.63}$$

with a flux function $\psi(x, y, z)$. The parallel derivative operator is given by

$$\nabla_{\|} = -[\psi, .] + \partial/\partial z \tag{2.64}$$

Look for a transformation of coordinates of the form:

$$\begin{cases} \xi^\alpha & = V^\alpha + C^\alpha(z - z_k) \\ s & = z - z_k \end{cases} \tag{2.65}$$

for each toroidal sector centered around z_k, where V^α and C^α are functions of x, y and z to be determined. Then the parallel derivative is given by

$$\nabla_\| = \nabla_\| \xi^\alpha \frac{\partial}{\partial \xi^\alpha} + \nabla_\| s \frac{\partial}{\partial s} \tag{2.66}$$

$$= \nabla_\| \xi^\alpha \frac{\partial}{\partial \xi^\alpha} + \frac{\partial}{\partial s} \tag{2.67}$$

In order to get $\nabla_\| = \partial/\partial s$, the following condition should be satisfied:

$$\nabla_\| \xi^\alpha = 0 \tag{2.68}$$

Equivalently,

$$\nabla_\| V^\alpha + C^\alpha + \nabla_\| C^\alpha (z - z_k) = 0 \tag{2.69}$$

One wants then

$$\begin{cases} C^\alpha & = -\nabla_\| V^\alpha \\ \nabla_\| C^\alpha & = \nabla_\| (\nabla_\| V^\alpha) = 0 \end{cases} \tag{2.70}$$

Functions that satisfy these conditions exist in the integrable case. Assume that a function ψ^* exists such that

$$\nabla_\| \psi^* = 0 \tag{2.71}$$

Explicitly this means

$$\frac{\partial \psi^*}{\partial z} = [\psi, \psi^*] \tag{2.72}$$

Note that ψ^* is like a conserved quantity of the particle motion in the (x, y) plane, z being the time and ψ being the time-dependent Hamiltonian.

Special case, Helical configuration in slab geometry

$$\psi = \psi(x, y - \lambda z) \tag{2.73}$$

then

$$\psi^* = \psi + \lambda x \tag{2.74}$$

Special case, Helical configuration in cylindrical geometry

$$\psi = \psi(r, m\theta - n\varphi) \tag{2.75}$$

then

$$\psi^* = \psi + \frac{n}{m} r^2 \tag{2.76}$$

Take

$$V^\alpha = f^\alpha(\psi^*) + g^\alpha(\psi^*)\,\chi, \tag{2.77}$$

Then

$$C^\alpha = \nabla_\| V^\alpha = g^\alpha(\psi^*)\nabla_\| \chi. \tag{2.78}$$

Choose χ such that $\nabla_\| \chi = 1$ then $\nabla_\| C^\alpha = 0$ so condition (2.70) and $\nabla_\| = \partial/\partial s$ are satisfied, but χ exists only in the integrable case where it satisfies a 1^{st} order linear PDE in two variables. In conclusion, the transformation writes

$$\begin{cases} \xi^\alpha & = f^\alpha(\psi^*) + g^\alpha(\psi^*)\,\chi + g^\alpha(\psi^*)(z - z_k) \\ s & = z - z_k \end{cases} \tag{2.79}$$

Note that one can easily prove that the Jacobian of the transformation is nonzero for arbitrary f^α and g^α. Similarly to the 2D case, to compute the parallel derivative by finite differences, one has to find Δx corresponding to a given increment Δs along s with $\xi^\alpha = cst$. The following finite difference equation results for the unknown increments Δx

$$[f^\alpha(\psi^*) + g^\alpha(\psi^*)\chi]_{\mathbf{x}+\Delta\mathbf{x},z_k+\Delta z} - [g^\alpha(\psi^*)]_{\mathbf{x}+\Delta\mathbf{x},z_k+\Delta z}\Delta z = [f^\alpha(\psi^*) + g^\alpha(\psi^*)\chi]_{\mathbf{x},z_k} \tag{2.80}$$

Solutions to these FD equations exist if the following conditions are satisfied

$$\psi^*(\mathbf{x} + \Delta\mathbf{x}, z_k + \Delta z) = \psi^*(\mathbf{x}, z_k) \tag{2.81}$$

$$\chi(\mathbf{x} + \Delta\mathbf{x}, z_k + \Delta z) = \chi(\mathbf{x}, z_k) - \Delta z. \tag{2.82}$$

Now Δx are solutions of the field line equations for a displacement Δz. The proof consists of taking the derivative of x with respect to z. This gives:

$$\frac{d\mathbf{x}}{dz} \cdot \boldsymbol{\nabla}_\mathbf{x}\psi^* + \partial_z\psi^* = 0 \tag{2.83}$$

$$\frac{d\mathbf{x}}{dz} \cdot \boldsymbol{\nabla}_\mathbf{x}\psi^* + \partial_z\chi = -1 \tag{2.84}$$

The increments Δx and Δy then simply derive from the field-line equations:

$$\frac{dx}{dz} = [\partial_y\psi^*]_{\mathbf{x}+\Delta\mathbf{x},z_k+\Delta z} \tag{2.85}$$

$$\frac{dy}{dz} = -[\partial_x\psi^*]_{\mathbf{x}+\Delta\mathbf{x},z_k+\Delta z} \tag{2.86}$$

which satisfy the system (2.83)-(2.84) above, since $\nabla_\| \psi^* = 0$ and $\nabla_\| \chi = 1$.

The direct calculation of $\nabla_\|$ at a given point is done by considering an arc of field-line passing through a point (x, y, z). Use a parametrization $x(\tau), y(\tau), z(\tau)$ to get the following system:

$$\begin{aligned} \frac{dx}{d\tau} &= \partial_y\psi^* \\ \frac{dy}{d\tau} &= -\partial_x\psi^* \\ \frac{dz}{d\tau} &= 1 \end{aligned} \tag{2.87}$$

For any differentiable function $f(x, y, z)$, one can compute the derivative along the field-line with respect to τ as follows:

$$\begin{aligned} \frac{d}{d\tau} f[x(\tau), y(\tau), z(\tau)] &= \frac{dx(\tau)}{d\tau}\partial_x f + \frac{dy(\tau)}{d\tau}\partial_y f + \frac{dz(\tau)}{d\tau}\partial_z f && (2.88)\\ &= \partial_y\psi\, \partial_x f - \partial_x\psi\, \partial_y f + \partial_z f && (2.89)\\ &= (\nabla_\| f)_\tau && (2.90) \end{aligned}$$

Since $dz/d\tau = 1$, one can choose to parametrize $z = z_k + 1$ for each toroidal sector ($\Delta z = \Delta\tau$). This shows that $(\nabla_\| f)_{z=z_k}$ can be computed by finite differences as follows with increments Δz along the field line:

$$\nabla_\| f = \frac{f(\tau + \Delta\tau) - f(\tau - \Delta\tau)}{2\,\Delta\tau} \tag{2.91}$$

Special case, Toroidal geometry

In polar coordinates, (R, φ, Z), the infinitesimal displacements are $(dR, Rd\varphi, dZ)$. These must be proportional to the components of $\mathbf{B}$. Thus,

$$\begin{aligned} dR &\propto B_R d\tau\\ Rd\varphi &\propto B_\varphi d\tau\\ dZ &\propto B_Z d\tau \end{aligned} \tag{2.92}$$

where τ is a parameter for the position along the field line. It is convenient to fix τ such that $d\varphi/d\tau = 1$ (case for toroidal sectors). The following field line equations result:

$$\begin{aligned} \frac{dR}{d\tau} &= R\frac{B_R}{B_\varphi}\\ \frac{d\varphi}{d\tau} &= 1\\ \frac{dZ}{d\tau} &= R\frac{B_Z}{B_\varphi} \end{aligned} \tag{2.93}$$

Then for a function $f(R, \varphi, Z)$

$$\begin{aligned} \frac{d}{d\tau} f(R, \varphi, Z) &= \frac{dR}{d\tau}\partial_R f + \frac{d\varphi}{d\tau}\partial_\varphi f + \frac{dZ}{d\tau}\partial_Z f\\ &= \frac{R}{B_\varphi}\left[B_R\partial_R f + \frac{B_\varphi}{R}\partial_\varphi f + B_Z\partial_Z f\right]\\ &= \frac{R}{B_\varphi}(\mathbf{B}.\boldsymbol{\nabla} f) \end{aligned} \tag{2.94}$$

At a given point φ, this leads to the following expression in FD form:

$$(\mathbf{B}.\boldsymbol{\nabla} f)^\varphi = \left(\frac{B_\varphi}{R}\right)^\varphi \left[\frac{f(\varphi + \Delta\varphi - f(\varphi - \Delta\varphi)}{2\,\Delta\varphi}\right] \tag{2.95}$$

where $f(\varphi \pm \Delta\varphi)$ corresponds to the value of $f(R, Z, \varphi)$ points $(R^\pm, Z^\pm, \varphi \pm \Delta\varphi)$ where $R^\pm$ and $Z^\pm$ are obtained by integrating the field-line equations (2.93).

Chapter 3

FENICIA: Description of the code

> إِنَّمَا المَكَارِمُ أَخلَاقٌ مُطَهَّرَةٌ، الدّينُ أَوَّلُهَا
> وَ العَقلُ ثَانيهَا وَ العِلمُ ثَالِثُهَا وَ الحُلمُ رَابِعُهَا
>
> علي بِن أَبِي طَالِب (٦٠٠ م - ٦٦١ م)

Contents

Aquarelle, (F. Hariri, 2007)

Throughout my Thesis, I developed from scratch a new modular code that I call FENICIA: **F**lux indep**EN**dent f**I**eld-aligned **C**oord**I**nate **A**pproach, after the FCI approach described in Sec. 2.2. In this chapter, I first list the main features of the code, then I describe details of the different numerical methods implemented. Since the most immediate application of FENICIA is to problems in plasma physics, present implemented operators are drawn from this field, in particular, operators embedded in models corresponding to the physics of drift waves and ITG turbulence. Later in Chapter 4, a series of test problems is presented to demonstrate the accuracy and flexibility of the code.

3.1 FENICIA: Flux indepENdent fIeld-aligned CoordInate Approach

FENICIA is a generic plasma simulation code written in FORTRAN, aimed at simulating a wide range of geometries and models, involving an arbitrary number of scalar and vector fields. It solves the general class of models (1.19), i.e. any model belonging to (1.19) as discussed in 1.4.2. The specifications of the code include:

- A generic code adapted to evolve a considerable number of scalar and vector fields.

- A modular code designed for easy assembly and flexible arrangement of operators. Each of the routines can be modified without altering the other modules/routines. This allows for the simulation of a wide class of models belonging to (1.19).

- Any coordinate system could be chosen for the discretization of operators in the poloidal plane.

- A flux-independent coordinate system (FCI) is used in the direction parallel to the magnetic field, thus allowing one to decouple the grid of the numerical problem from the magnetic field geometry where the description in the poloidal plane does not employ magnetic coordinates. Information on field lines will only be needed to compute parallel derivatives.

- Operators can be freely discretized using any desired numerical scheme (Finite differences, Finite Volumes, Finite Elements, FFTs...)

- The geometry of the problem can address both straight, toroidal configurations and X-point configurations. In the present version of the code, a magnetic configuration with cylindrical geometry in a rectangular box is considered, leaving the toroidal case for future work.

- Boundary conditions are chosen such that everything outside the predefined plasma radius is set to zero and the points are periodic in the z direction. Generalized implementation of more complicated coupled boundary conditions is a possible future extension.

- Parallel communication in the z direction using the Message Passing Interface (MPI).

- Input and output to Unformatted FORTRAN files and HDF5 file format

FENICIA is designed to automate the common tasks needed for simulation codes, and to separate the complicated details such as differential geometry, parallel communication, and file input/output from the user-specified physics equations to be solved, while remaining as flexible as possible. Thus the physics equations being solved are clearly provided in one place, and can be easily changed with only minimal knowledge of the inner workings of the code. Each of the program components can be modified without altering the other modules. As much as possible, this allows the user to concentrate on the physics, rather than worrying about the numerics. This flexibility, and the ability to code in a general way allows one to tackle a wide range of analytical theories (fluid and kinetic models) and helps in their development. Furthermore, the use of the FCI approach is a new crucial technique that makes the code easily adaptable to any other complicated geometry. It is thus a powerful tool for plasma theory and a necessity for the numerical tokamak turbulence codes in general [Hariri 2013].

3.2 Time Integration Schemes

3.2.1 Semi-discrete time-advancing scheme with operator splitting

A variety of physical phenomena arising in tokamak plasmas is modeled by systems of partial differential equations (PDEs). Computing the solutions of these systems is challenging and requires development of fast, reliable and accurate numerical methods. A conventional Divide and Conquer (D&C) strategy is to decompose the given system of PDEs into simpler subproblems and treat them individually using specialized numerical algorithms and mixed discretization methods. The criterion is to use an operator splitting technique allowing us to decouple the physics effects occurring at different timescales. For instance, one may choose to evolve nonlinear terms explicitly and linear terms implicitly. Furthermore, the use of different time steps for different subproblems is feasible. Exceptions could be made depending on the physics timescale of the terms in question. In this section, I describe the details of the second-order time-advancing scheme and the operator splitting technique implemented in FENICIA. A centered Leapfrog scheme is applied to solve the explicit part of the model. However, the Leapfrog scheme requires a time-filtering because the nonlinearities and the round-off errors lead to a decoupling of the solution between even and odd time steps. A remedy is to use a predictor-corrector scheme to initialize the Leap-frog. Our interest is evolving a general system of the form

$$\partial_t L \cdot S = E(S) + I \cdot S, \tag{3.1}$$

described in Chapter 1. Mathematically, it is equivalent to splitting the vector field on the R.H.S of this equation into integrable parts E and I.

Leap-frog:

The Leap-frog scheme requires the following steps:

Find P such that

$$\partial_t[e^{P(t-t_0)} L\, S] = e^{P(t-t_0)}[\partial_t L\, S - I\, S] \tag{3.2}$$

but,

$$\partial_t[e^{P(t-t_0)} L\, S] = e^{P(t-t_0)}[\partial_t L\, S + P\, L\, S] \tag{3.3}$$

Then $P\, L = -I$ so $P = -I\, L^{-1}$.

Multiplying (3.1) by $e^{P(t-t_0)}$ yields:

$$\partial_t[e^{P(t-t_0)} LS] = e^{P(t-t_0)} E(S) \tag{3.4}$$

where P commutes with $e^{P(t-t_0)}$. Let $t_{n+1} = t_n + \Delta t$ where n is the time index. Then perform a Leap-frog with t_n being the middle point to get

$$e^{P\,\Delta t}\, L\, S_{n+1} - e^{-P\,\Delta t}\, L\, S_{n-1} = E(S_n) \cdot 2\,\Delta t \tag{3.5}$$

Recall that $P = -I\, L^{-1}$, so expression (3.5) becomes

$$LS_{n+1} = \underbrace{e^{2\,\Delta t\, I\, L^{-1}}\, L\, S_{n-1}}_{(3.6\text{-a})} + 2\Delta t\, \underbrace{e^{\Delta t\, I\, L^{-1}}\, E(S_n)}_{(3.6\text{-b})} \tag{3.6}$$

To solve for operators of the form e^{Ht} applied to a given operator, where H is a time-independent matrix and t is a scalar denoting the time, consider the following equation

$$\partial_t f - Hf = 0 \tag{3.7}$$

One can equivalently write

$$\partial_t(e^{-Ht} f) = 0 \tag{3.8}$$

The solution to this differential equation is $f(t) = e^{Ht} f(0)$. Thus, any expression of the form $e^{Ht} S$ can be obtained by solving Eq. (3.7), with an algorithm of choice and to the desired accuracy, for a time t and any initial condition S.

For $H = I\, L^{-1}$, $t = 2\Delta t$ and with initial condition $f(0) = L\, S_{n-1}$, one gets the equation

$$\partial_t f - IL^{-1} f = 0 \tag{3.9}$$

which solution is given by

$$e^{2\Delta t I L^{-1}} L S_{n-1} = f(2\Delta t) \tag{3.10}$$

One notices that (3.6-a) is thus a solution to (3.9). Let $f = Lg$, then g satisfies

$$\partial_t Lg - Ig = 0 \tag{3.11}$$

with initial condition $g(0) = S_{n-1}$. Consequently, $f(2\Delta t) = Lg(2\Delta t)$ where g is the solution of Eq. (3.11). Hence, the numerical scheme (3.6) can be expressed as follows:

$$L\, S_{n+1} = L\, G(2\Delta t, S_{n-1}) + 2\Delta t\, e^{\Delta t\, I\, L^{-1}}\, E(S_n) \tag{3.12}$$

where $G(\tau, g_0)$ indicates the general solution of (3.11) for a time τ and an initial condition $g(0) = g_0$.

Likewise, one can perform the same steps above for (3.6-b) to get

$$e^{\Delta t\, I\, L^{-1}} L^{-1} E(S_n) = LG(\Delta t, L^{-1} E(S_n)) \tag{3.13}$$

Ultimately, the time evolution scheme (3.6) written using the "G" notation (where G is the solver of (3.11) i.e: $G(\Delta t, F) = e^{\Delta t\, I\, L^{-1}}\, F$) becomes

$$S_{n+1} = G(2\Delta t, S_{n-1}) + 2\Delta t\, G(\Delta t, L^{-1} E(S_n)) \tag{3.14}$$

<u>Predictor Corrector:</u>

The Predictor-Corrector scheme requires the following steps:

Multiplying (3.1) by L^{-1} and using $e^{-I\, L^{-1}\, (t-t_0)}$ yields:

$$\partial_t [e^{-L^{-1}\, I\, (t-t_0)} LS] = e^{-L^{-1}\, I\, (t-t_0)}\, L^{-1}\, E(S) \tag{3.15}$$

The explicit predictor step is as follows:

$$e^{-L^{-1}\, I\, \Delta t} S^*_{n+1} - S_n = \Delta t\, L^{-1}\, E(S_n) \tag{3.16}$$

Then a second step corrector $(1/2, 1/2)$ is applied as follows

$$e^{-L^{-1}\, I\, \Delta t} S_{n+1} - S_n = \frac{1}{2}\, \Delta t\, \{e^{-L^{-1}\, I\, \Delta t}\, L^{-1}\, E(S^*_{n+1}) + L^{-1}\, E(S_n)\} \tag{3.17}$$

Again, using the "G" notation the ultimate scheme writes

$$S^*_{n+1} = G(\Delta t, S_n) + \Delta t\, G(\Delta t, L^{-1}\, E(S_n)) \tag{3.18}$$

A necessary second step corrector is to be applied giving

$$S_{n+1} = S^*_{n+1} + \frac{1}{2}\, \Delta t\, \{G(\Delta t, L^{-1}\, E(S^*_{n+1})) - G(\Delta t, L^{-1} E(S_n))\} \tag{3.19}$$

In FENICIA, one can use any scheme in solving for G. Practically, at the first time step, one performs a predictor-corrector. Then a Leap-frog is used to advance the equations for the remaining time steps and the solution is corrected every `ntpc` times that the user defines in the input file.

3.2.2 Calculate explicit operators $E(S)$

The first step into implementing any model belonging to (1.19) is to write it in matrix-vector form as in (1.20) after deciding which operators to evolve explicitly and which to evolve implicitly. The easiest task is calculating the nonlinear operators vector field. The routine `calc_exp_op` takes an input vector S containing all the states (n, $u_\parallel$, $T_\parallel$, etc...) and calculates $E(S)$, a vector field containing all the operators to be solved explicitly.

In general, this vector contains terms pertaining to the frequency range of the physics problem. For example, in (1.20), nonlinearities are embedded in the Poisson bracket term. In this case, $E(S)$ writes:

$$E(S) = \begin{bmatrix} 0 \\ -[\phi, log(n_0)] \\ 0 \end{bmatrix} \tag{3.20}$$

Note that it could be expanded to any desired dimension and it may contain nonlinearities of other types as well.

3.2.3 Solve linear operators $L\,S = E(S')$

The second step is to solve the linear system

$$L\,S = E(S') \tag{3.21}$$

given $E(S)$ and L. This is done by the routine `solv_lin_op` by back substitution. It takes the vector $E(S)$ as input and returns $L^{-1}E(S)$ in output. For example, for model (1.20), the system takes the form

$$\begin{vmatrix} 1-\rho_*^2\nabla_\perp^2 & -1 & 0 \\ 0 & 1 & 0 \\ 0 & 0 & 1 \end{vmatrix} \begin{vmatrix} \phi \\ n \\ u \end{vmatrix} = \begin{vmatrix} 0 \\ -[\phi', log(n_0)] \\ 0 \end{vmatrix} \tag{3.22}$$

By back substitution one solves the following system of equations corresponding to that model:

$$1-\rho_*^2\nabla_\perp^2\phi - n = 0 \tag{3.23}$$

$$n = -[\phi', log(n_0)] \tag{3.24}$$

$$u = 0 \tag{3.25}$$

This reduces to solving the Helmholtz equation

$$(1-\rho_*^2\nabla_\perp^2)\phi = n \tag{3.26}$$

This type of differential operators is solved using Fourier transforms in FENICIA. In other instances, particularly when it comes to solving the entire quasi-neutrality equation, other numerical schemes can be applied. The size of L varies depending on the number of fields in the desired model. The important thing to notice here is that adding a field to the matrix L corresponds to adding an additional diagonal element equals to 1.

3.2.4 Generate derivatives

One routine in the code is concerned with the approximation of derivatives up to fourth order accuracy using finite differences. It is called `generate_deriv`. If nx is the number of points in *x* and ny is the number of points in *y*, then for a given function g, a 5-points stencil is used to compute values of derivatives g_x, g_y in the bulk of the domain delimited by $i = 2, nx - 2$ and $j = 2, ny - 2$ respectively as

$$\Delta x\, g_x(i,j) = \frac{1}{12}\, g(i-2,j) - \frac{2}{3}\, g(i-1,j) + \frac{2}{3}\, g(i+1,j) - \frac{1}{12}\, g(i+2,j) + \mathcal{O}(h^4) \quad (3.27)$$

and

$$\Delta y\, g_y(i,j) = \frac{1}{12}\, g(i,j-2) - \frac{2}{3}\, g(i,j-1) + \frac{2}{3}\, g(i,j+1) - \frac{1}{12}\, g(i,j+2) + \mathcal{O}(h^4) \quad (3.28)$$

with Δx and Δy being the grid sizes in the *x* and y directions, respectively. The first derivative in *x* and *y*, g_{xy}, is computed in the domain delimited by $i = 1, nx-1$ and $j = 1, ny - 1$ as

$$\Delta x \Delta y\, g_{xy}(i,j) = \frac{g(i+1,j+1) + g(i-1,j-1) - g(i-1,j+1) - g(i+1,j-1)}{4} \quad (3.29)$$

Furthermore, g_x, g_y and g_{xy} are all set to zero on the boundary layer where $i \in \{0, nx\}$ and/or $j \in \{0, ny\}$. And non-centered forward 3^{rd} order finite differences are used at the boundary where $i = 1, nx - 1$ and $j = ny - 1$ with the following form

$$\begin{aligned}\Delta x\, g_x(1, 1:ny-1) = &-\frac{11}{6}\, g(1, 1:ny-1) + 3\, g(2, 1:ny-1) \\ &- \frac{3}{2}\, g(3, 1:ny-1) + \frac{1}{3}\, g(4, 1:ny-1) + \mathcal{O}(h^3)\end{aligned} \quad (3.30)$$

$$\begin{aligned}\Delta x\, g_x(nx-1, 1:ny-1) = &\frac{11}{6}\, g(nx-1, 1:ny-1) - 3\, g(nx-2, 1:ny-1) \\ &+ \frac{3}{2}\, g(nx-3, 1:ny-1) - \frac{1}{3}\, g(nx-4, 1:ny-1) + \mathcal{O}(h^3)\end{aligned} \quad (3.31)$$

$$\begin{aligned}\Delta y\, g_y(1:nx-1, 1) = &-\frac{11}{6}\, g(1:nx-1, 1) + 3\, g(1:nx-1, 2) \\ &- \frac{3}{2}\, g(1:nx-1, 3) + \frac{1}{3}\, g(1:nx-1, 4) + \mathcal{O}(h^3)\end{aligned} \quad (3.32)$$

$$\begin{aligned}\Delta y\, g_y(1:nx-1, ny-1) = &\frac{11}{6}\, g(1:nx-1, ny-1) - 3\, g(1:nx-1, ny-2) \\ &+ \frac{3}{2}\, g(1:nx-1, ny-3) - \frac{1}{3}\, g(1:nx-1, ny-4) + \mathcal{O}(h^3)\end{aligned} \quad (3.33)$$

$$\begin{aligned}\Delta x\, g_x(2:nx-2,1) = {} & \frac{1}{12}\, g(0:nx-4,1) - \frac{2}{3}\, g(1:nx-3,1) \\ & + \frac{2}{3}\, g(3:nx-1,1) - \frac{1}{12}\, g(4:nx,1) + \mathcal{O}(h^3)\end{aligned} \tag{3.34}$$

$$\begin{aligned}\Delta x\, g_x(2:nx-2,ny-1) = {} & \frac{1}{12}\, g(0:nx-4,ny-1) - \frac{2}{3}\, g(1:nx-3,ny-1) \\ & + \frac{2}{3}\, g(3:nx-1,ny-1) - \frac{1}{12}\, g(4:nx,ny-1) + \mathcal{O}(h^3)\end{aligned} \tag{3.35}$$

$$\begin{aligned}\Delta y\, g_y(1,2:ny-2) = {} & \frac{1}{12}\, g(1,0:ny-4) - \frac{2}{3}\, g(1,1:ny-3) \\ & + \frac{2}{3}\, g(1,3:ny-1) - \frac{1}{12}\, g(1,4:ny) + \mathcal{O}(h^3)\end{aligned} \tag{3.36}$$

$$\begin{aligned}\Delta y\, g_y(nx-1,2:ny-2) = {} & \frac{1}{12}\, g(nx-1,0:ny-4) - \frac{2}{3}\, g(nx-1,1:ny-3) \\ & + \frac{2}{3}\, g(nx-1,3:ny-1) - \frac{1}{12}\, g(nx-1,4:ny) + \mathcal{O}(h^3)\end{aligned} \tag{3.37}$$

3.2.5 Solve parallel operations $I.S$

The parallel operation routine, *parallel_operation*, calculates the product $I.S$ given a vector of states S. For example, for model (1.20), this is equivalent to the following operation

$$I.S = \begin{vmatrix} 0 & 0 & 0 \\ 0 & 0 & A\nabla_{\|} \\ A\nabla_{\|} & \frac{1}{\tau}A\nabla_{\|} & 0 \end{vmatrix} \begin{vmatrix} \phi \\ n \\ u \end{vmatrix} \tag{3.38}$$

Note that I may contain terms pertaining to the perpendicular dynamics as well.

The parallel gradient of any function f is computed along the field lines by 2^{nd} order centered finite differences in the *grad_parall_centered* routine as follows

$$\nabla_{\|} f(i,j,k) = \frac{f_{i,j,k+1} - f_{i',j',k-1}}{2\,\Delta\varphi} \tag{3.39}$$

where i, j and k respectively indicate the indices along the x, y and z directions. More precisely, k is the index of toroidal planes where the parallel gradient needs to be calculated. Note that the Forward and Backward finite difference schemes were implemented as well. Similarly, the parallel Laplacian is calculated using the *grad_parall_squared* routine by

$$\nabla_{\|}^2 f(i,j,k) = \frac{f_{i,j,k+1} - 2\, f_{i',j',k} + f_{i'',j'',k-1}}{\Delta\varphi^2} \tag{3.40}$$

Eventually, a Lagrangian scheme could be applied instead of any other higher order appropriate scheme like Runge-Kutta. However, I demonstrate in the next Chapter that the centered FD scheme is good enough for the physics to be tackled.

3.2.6 Solve reduced equation $\partial_t L\, S = I.S$

As a third step, one needs a solver for the reduced equation

$$\partial_t L\, S = I.S \tag{3.41}$$

With the choice of the scheme discussed in Sec. 3.2.1, the "G" solver of Eq. (3.11) becomes a general solver of reduced equations of the type (3.41). This is done by the routine `solv_red_eq`. It applies the G solver to $L^{-1}E(S)$ and returns $G(\Delta t, L^{-1}E(S))$. For example, for model (1.20), this reduces to solving

$$\partial_t \begin{vmatrix} 1-\rho_*^2\nabla_\perp^2 & -1 & 0 \\ 0 & 1 & 0 \\ 0 & 0 & 1 \end{vmatrix} \begin{vmatrix} \phi \\ n \\ u \end{vmatrix} = \begin{vmatrix} 0 & 0 & 0 \\ 0 & 0 & A\nabla_\parallel \\ A\nabla_\parallel & \frac{1}{\tau}A\nabla_\parallel & 0 \end{vmatrix} \begin{vmatrix} \phi \\ n \\ u \end{vmatrix} \tag{3.42}$$

The "G" solver can thus embed any numerical scheme of choice. In particular, in FENICIA, since this solver is concerned with the operators to be solved implicitly with terms that have short timescales with respect to the physics, an iterative scheme is implemented to solve this part. The steps of the iterative scheme to predict the solution to Eq. (3.41) are as follows: Knowing S_n, one can calculate $I.S_n$ using the `parallel_operation` routine and $L^{-1}(\Delta t\, I.S_n)$ using the `solv_lin_op` routine. The predictor step to find S_{n+1}^* is as follows

$$L\, S_{n+1}^* - L\, S_n = \Delta t\, I.S_n \tag{3.43}$$

Then the corrector step writes

$$L\, S_{n+1} - L\, S_n = \frac{\Delta t}{2} I.S_n + \frac{\Delta t}{2} I.S_{n+1}^* + \mathcal{O}(\Delta t^3) \tag{3.44}$$

Note that the corrector is applied twice to this routine in order to get $\mathcal{O}(\Delta t^4)$ accuracy. Using a fully implicit scheme is plausible. However, this might be time consuming knowing that computing the matrix I requires interpolation, something that could be handled in future versions of the code.

3.2.7 Operator Splitting of the reduced equation

Assume $H = A + B$, solve

$$\partial_t f - Hf = 0 \tag{3.45}$$

by splitting. The solution to this equation can be written as

$$f = \mathrm{e}^{H\tau} f_0. \tag{3.46}$$

The operator $\mathrm{e}^{H\tau}$ can be split with third order accuracy either as

$$\mathrm{e}^{H\tau} = \mathrm{e}^{\frac{1}{2}A\tau}\, \mathrm{e}^{B\tau}\, \mathrm{e}^{\frac{1}{2}A\tau} + \mathcal{O}(\tau^3) \tag{3.47}$$

or as

$$\mathrm{e}^{H\tau} = \frac{1}{2}(\mathrm{e}^{A\tau}\, \mathrm{e}^{B\tau} + \mathrm{e}^{B\tau}\, \mathrm{e}^{A\tau}) + \mathcal{O}(\tau^3) \tag{3.48}$$

The first choice requires 3 operations and the second choice requires 4. One needs separate solvers for

$$\partial_t f - Af = 0 \tag{3.49}$$

and

$$\partial_t f - Bf = 0. \tag{3.50}$$

Call $G(\tau, f_0)$ the solution with initial value f_0 and a time τ. Use the most effective solver in either case respectively as follows

$$G_A(\frac{\tau}{2}, .) \circ G_B(\tau, .) \circ G_A(\frac{\tau}{2}, f_0), \tag{3.51}$$

or,

$$G_B(\frac{\tau}{2}, .) \circ G_A(\tau, .) \circ G_B(\frac{\tau}{2}, f_0). \tag{3.52}$$

Thus, any expression of the form $\mathrm{e}^{H\tau}F$ is obtained by solving Eq. (3.45), to the desired accuracy, for a time $t = \tau$, an initial condition $f(0) = F$. The solver G can be applied as much as needed using only one routine in the code.

In FENICIA, this splitting technique is used when the operator I is equal to the sum of two column operators $P+D$ where P includes parallel dynamics along with parallel diffusion terms and D contains perpendicular diffusion terms. For example, for the more complex model that will be presented in Chapter 5 we have

$$P = \begin{vmatrix} 0 & 0 & 0 & 0 & 0 \\ 0 & 0 & C_{\|}\nabla_{\|} & 0 & 0 \\ C_{\|}\nabla_{\|} & \frac{C_{\|}}{\tau}\nabla_{\|} & 0 & 0 & C_{\|}\nabla_{\|} \\ 0 & 0 & 0 & -\chi_{\|\perp}\nabla_{\|}^2 & 0 \\ 0 & 0 & \frac{2\,C_{\|}}{\tau}\nabla_{\|} & 0 & -\chi_{\|\|}\nabla_{\|}^2 \end{vmatrix} \tag{3.53}$$

and

$$D = \begin{vmatrix} 0 \\ D_n\nabla_{\perp}^2\tilde{n} \\ D_u\nabla_{\perp}^2 u_{\|} \\ D_{T_\perp}\nabla_{\perp}^2 T_{\perp} \\ D_{T_\|}\nabla_{\perp}^2 T_{\|} \end{vmatrix} \tag{3.54}$$

Finally, a new routine `solv_red_eq_parallel` equivalent to `solv_red_eq` has been added to solve only

$$\partial_t L \cdot S = P \cdot S \tag{3.55}$$

and another one called `solv_red_eq_dissipation` has been added to solve

$$\partial_t L \cdot S = D \cdot S \tag{3.56}$$

So when the model contains both parallel and perpendicular dissipation, `solv_red_eq_dissipation` is called first at $\tau = \Delta t/2$ then `solv_red_eq_parallel` is called at $\tau = \Delta t$ and at last `solv_red_eq_dissipation` is called again at $\tau = \Delta t/2$ as detailed earlier in (3.51).

3.2.8 A second order accurate Predictor-corrector scheme

Below is a sketch of how the predictor-corrector scheme is used to stabilize the Leap-frog:

1. Save the state S_n
2. Calculate $E(S_n)$ and $L^{-1}E(S_n)$
3. Solve $G(\Delta t, S_n)$ and $G(\Delta t, L^{-1}E(S_n))$
4. Predict $S^*_{n+1} = G(\Delta t, S_n) + \Delta t\, G(\Delta t, L^{-1}E(S_n))$
5. Calculate $E(S^*_{n+1})$ and $L^{-1}E(S^*_{n+1})$
6. Solve $G(\Delta t, L^{-1}E(S^*_{n+1}))$
7. Correct $S_{n+1} = G(\Delta t, S_n) + \frac{1}{2}\Delta t\ \left\{G(\Delta t, L^{-1}E(S^*_{n+1}) + G(\Delta t, L^{-1}E(S_n))\right\}$

3.2.9 A second order accurate Leap-frog scheme

Below is a sketch of how the Leap-frog scheme works to advance the general set of equations:

1. Save the state S_n
2. Calculate $E(S_n)$ and $L^{-1}E(S_n)$
3. Solve $G(\Delta t, L^{-1}E(S_n))$ and $G(2\Delta t, S_{n-1})$
4. Calculate $S_{n+1} = G(2\Delta t, S_{n-1}) + 2\Delta t\, G(\Delta t, L^{-1}E(S_n))$

3.3 Data handling and Optimization

3.3.1 Data Storage

Data storage is time-consuming and error-prone. In FENICIA, this is handled by a set of workspace Pointer arrays which manage memory dynamically, allowing the code to be written in a much more concise manner, and making the source code much easier to read. Pointers are used in the code to tailor the storage requirements exactly to the size of the problem in hand. Those are variables which are dynamically associated with (or aliased to) some target data. As well as pointing to existing variables which have the TARGET attribute, pointers may be associated with blocks of dynamic memory. This memory is allocated through the ALLOCATE statement which creates an un-named variable or array of the specified size, and with the data type, rank, etc. of the pointer. However care must be taken to avoid programming errors. This was indeed possible by making sure that all pointers to a defunked target are deallocated.

Several data classes have been implemented: 3D scalar and vector fields, and 2D scalar and vector fields which are constant in the z-coordinate. Scalar operations include addition, multiplication, exponentiation by real values or scalar fields. In addition to arithmetic operations, standard mathematical functions such as $sqrt()$ and $abs()$ are also used. This allows all operations on scalar and vector fields to be written very clearly and concisely.

The number of states and workspaces to be used are set by the user depending on the target physics model. There are global parameters and variables that are unchanged in the code and that the user will not have to worry about. Input parameters, likely to change at runtime, should be entered by the user in a file called "`input_file`" that should be included in the runtime directory.

All aspects of a simulation can be set at run-time except the equations solved which are set in a compiled physics module. This includes the number of steps, run-time limits, data and restart output period, differencing methods, field initialization and boundary conditions. Instead, by keeping all options in one file and assigning default values to new options, simulations can be easily restarted at a later time.

Binary data input and output (grid input, data and restart file output) can be to both unformatted format files and the Hierarchical Data Format (HDF5) file format. Furthermore, I have written post-processing MATLAB scripts in order to view and analyze the results. Those can be found in the folder "`scripts`". t

3.3.2 Optimization

Since flexibility is an aim of FENICIA, and performance is a concern for large-scale simulations, optimization must be addressed. A major optimization used in the data objects to speed up the code execution is memory recycling, which eliminates allocation and freeing of memory. This is done by memory recycling, which can be used because all the scalar fields are the same size. Each routine implements a global stack of available memory blocks. When an object is assigned a value, it attempts to grab one of these memory blocks, and if none are available then a new block is allocated. When an object is destroyed, its memory block is not freed, but is put onto the stack. Since the evaluation of the time-derivatives involves the same set of operations each time, this system means that memory is only allocated the first time the time-derivatives are calculated, after which the same memory blocks are re-used. This eliminates the slow system calls needed to allocate and free memory, replacing them with fast pointer manipulation. This mechanism is handled internally, and is invisible to the programmer.

3.4 Differential Operators Discretization

In FENICIA, differential operators are divided into two classes: those which are independent of any coordinate system, specifically operators pertaining to the perpendicular dynamics; and those which are intended for use in a flux-independent field-aligned coordinate system, specifically operators pertaining the parallel dynamics. In the present version of the code, one defines any field at nodes in the Cartesian (x, y, z) grid. Derivatives in the poloidal plane are computed in this reference frame by holding z constant, and only parallel derivatives need to know about the magnetic field geometry and are computed using the new FCI coordinate system.

3.4.1 Perpendicular dynamics

Nonlinear Advection Operators

Nonlinear operators belonging to $E(S)$ can be discretized with a scheme of choice. In the models considered in this thesis, the Poisson brackets are the main nonlinearities driving instabilities. Those are time consuming and may lead to undesirable effects due to the superposition of frequencies higher than the Nyquist frequency. Those are called aliasing effects in signal theory [Max 1977, Press 2007]. In the actual implementation, I use Arakawa's finite difference scheme, Eq.(45) of [Arakawa 1966], to guarantee the conservation of mean kinetic energy and mean square vorticity and to get rid of aliasing effects. In fact, it was shown in [Arakawa 1966] that in two-dimensional incompressible flow some of the integral constraints on quantities of physical importance, such as the conservation of mean kinetic energy, mean square vorticity, can be maintained if the finite difference analogue for the advection term is properly designed. Since the required constraints are on the advection term, which has the form of a Jacobian operator for the flow considered, the finite difference scheme for the Jacobian must have a certain restricted form. Based upon a consistent interaction between grid points, a general form of finite difference Jacobian, which maintains the integral constraints, was derived by Arakawa [Arakawa 1966]. When the quadratic quantities are conserved in a finite difference scheme, nonlinear computational instability cannot occur. This follows from the fact that if the square of a quantity is conserved with time when summed up over all the grid points in a domain, the quantity itself will be bounded, at every individual grid point, throughout the entire period of integration. The demonstration that advection terms can be written into a Jacobian form is given in Appendix C. Tests have been done using FENICIA to prove the conservation of the quadratic quantities for a 2-D Navier-Stokes equation. These will be shown in Chapter 4.

The Laplace Operator

Calculating the Laplace operator or inverting it are common operations in solving turbulent models. For instance, one needs to solve typical operations like the Helmholtz operator

$$H = (1 - \rho_*^2 \nabla_\perp^2)\phi, \tag{3.57}$$

and the diffusion equation

$$\partial_t n = D_n \nabla_\perp^2 n. \tag{3.58}$$

Other models might have other operators. But those are the common ones considered in our physics models. They're all examples of the Poisson equation

$$W = \nabla_{\perp}^{2}\phi, \tag{3.59}$$

where the Laplace operator $\nabla_{\perp}^{2}$ is defined by

$$\nabla_{\perp}^{2}\phi = \partial_x^2\phi(x,y) + \partial_y^2\phi(x,y). \tag{3.60}$$

In order to calculate the discrete Laplacian, consider an approximation of the latter operator using the two-dimensional five-point stencil finite difference method. For each $1 \leq i \leq nx-1$ and $1 \leq j \leq ny-1$ with suitable extensions at $i = (0, nx)$ and $j = (0, ny)$, this results in the following expression:

$$\begin{aligned}\nabla_{\perp}^{2}\phi_{ij} = {} & \frac{\phi_{i+1,j} - 2\phi_{i,j} + \phi_{i-1,j}}{\Delta x^2} \\ & + \frac{\phi_{i,j+1} - 2\phi_{i,j} + \phi_{i,j-1}}{\Delta y^2}\end{aligned} \tag{3.61}$$

where Δ_x and Δ_y are the respective increments in the x and y directions and $\phi(x,y)$ vanishes on the boundary layer of the lattice grid. Consequently, a sine Fourier transform should be used. Furthermore, to ensure the continuity of the first order derivatives, symmetry is imposed around $i = 0$ and $i = nx$ such as

$$\phi_{-1,j} = -\phi_{1,j} \tag{3.62}$$

and

$$\phi_{nx+1,j} = -\phi_{nx-1,j} \tag{3.63}$$

This results in a vanishing Laplacian at the edges

$$(\partial_x^2\phi)_{i=0} = (\partial_x^2\phi)_{i=nx} = 0. \tag{3.64}$$

Similarly,

$$(\partial_y^2\phi)_{j=0} = (\partial_y^2\phi)_{j=ny} = 0. \tag{3.65}$$

This means, if $\phi_{i,j}$ represents an odd function, then $(\partial_x^2\phi)_{ij}$ and $(\partial_y^2\phi)_{ij}$ must represent odd functions.

In FENICIA, Sine Discrete Fourier Transforms (DFT)s are used to solve for ϕ. Let ϕ_i be the discrete set of values corresponding to ϕ where $0 \leq i \leq n$ and $\phi_0 = \phi_n = 0$. Then ϕ can be written as a sum of Sinus functions

$$\phi_i = \sum_{l=0}^{n} \hat{\phi}_l \sin\left(\frac{i\pi l}{n}\right) \tag{3.66}$$

One can verify that we indeed get

$$\phi_0 = \sum_{l=0}^{n} \hat{\phi}_l \sin(0) = 0 \tag{3.67}$$

and

$$\phi_n = \sum_{l=0}^{n} \hat{\phi}_l \, \sin(\pi l) = 0 \tag{3.68}$$

The expression of the second order derivative using second order finite differences becomes

$$\begin{aligned}
\partial_x^2 \phi_i \quad &\approx \frac{1}{\Delta_x^2}\left(\phi_{i+1} - 2\phi_i + \phi_{i-1}\right) &(3.69)\\
&= \frac{1}{\Delta_x^2} \sum_{l=0}^{n} \hat{\phi}_l \left\{ \sin\left[\frac{(i+1)\pi l}{n}\right] - 2\sin\left[\frac{i\pi l}{n}\right] + \sin\left[\frac{(i-1)\pi l}{n}\right] \right\} &(3.70)\\
&= \frac{1}{\Delta_x^2} \sum_{l=0}^{n} \hat{\phi}_l \left\{ 2\sin\left[\frac{i\pi l}{n}\right] \cos\left[\frac{\pi l}{n}\right] - 2\sin\left[\frac{i\pi l}{n}\right] \right\} &(3.71)\\
&= \sum_{l=0}^{n} \hat{\phi}_l \, \sin\left[\frac{i\pi l}{n}\right] \underbrace{\frac{2}{\Delta_x^2}\left(\cos\left[\frac{\pi l}{n} - 1\right]\right)}_{= -k_x^2} &(3.72)
\end{aligned}$$

So formally

$$\partial_x^2 \phi_i \longrightarrow -k_x^2 \, \hat{\phi}_l \tag{3.73}$$

where $-k_x^2 = 2\,\cos\left[\frac{\pi l}{n} - 1\right]/\Delta_x^2$.

Practically, $\hat{\phi}$ is calculated using the FFTW library routines (see manual [Johnson 2005]). Depending on the boundary conditions of the problem, one can choose among different types of multi-dimensional transforms. For instance, in a magnetic island geometry, Direct Fourier Transforms (DFTs) are employed in the direction where ϕ is periodic. In a circular magnetic surfaces geometry, the boundary conditions are such that the function ϕ vanishes at both ends and both ϕ_{ij} and $\nabla^2\phi_{ij}$ represent odd functions. Consequently, Discrete Sine Transforms (DST) of type FFTW_RODFT00 can be applied. An inverse Fourier transform is then employed to get the values of ϕ in real space.

Since the operations involving the inversion of the Laplacian have all the same form, only one routine is needed in the code to solve this problem. Tests are to be shown in Chapter 5 where ϕ is periodic in the y direction when considering an island geometry, and ϕ satisfies Dirichlet boundary conditions when considering circular magnetic surfaces geometry.

3.4.2 Parallel dynamics

Discretization of $\nabla_{\parallel}$

The FCI approach derived in Chapter 2 is employed to find the coordinates of a point that follows the field lines and it is implemented in the routine *map*. The grid considered in the present version of the code is shown in Fig. 3.1. As discussed in Sec. 2.2.1, one needs to find end points along field lines for a given displacement Δz along z from the finite difference equations for the unknown increments Δx given by (2.35) in Sec. 2.2.1. Points following a field line are not necessarily nodes of the mesh. Consequently, an interpolation technique is required at end points of each field line to find the function values and thus to calculate $\nabla_{\parallel}$. Knowing that the FCI transforms points of coordinates (x, y) in $z = 0$ to a new set of coordinates (x_t, y_t) in $z = \Delta z$, what remains is to find where does every point fall in the plane $z = \Delta z$ so that we use the values of the function at its neighboring points for interpolation. For this we calculate first

$$i' \equiv INT\left(\frac{x_t}{\Delta x}\right)(i, j) \tag{3.74}$$

$$j' \equiv INT\left(\frac{y_t}{\Delta y}\right)(i, j) \tag{3.75}$$

where INT represents the integer part. Then we compute

$$t_x = \frac{x_t - x(i', j')}{\Delta x} \tag{3.76}$$

$$t_y = \frac{y_t - y(i', j')}{\Delta y} \tag{3.77}$$

Now we know the coordinates of the points neighboring the transformed points, and the value of the function there. Finally, we can interpolate using values of the function at those nodes, and ultimately calculate $\nabla_{\parallel}$. Then second order centered finite differences are used to compute parallel derivatives using the routine *generate_deriv* and `parallel_operation`. Note that the use of finite differences is not a limitation. In particular, in the case of a kinetic model, the implementation of a Semi-Lagrangian scheme for the parallel dynamics exploiting the same ideas is also possible.

In FENICIA, a 2D Hermite spline interpolation is used. Details are presented in the following section.

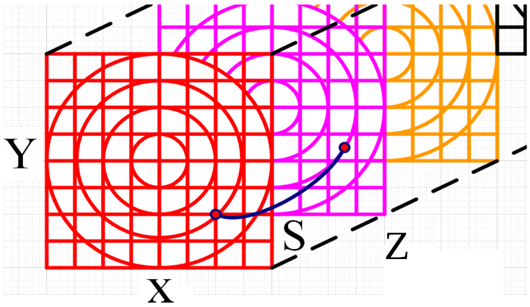

Figure 3.1: The grid used in the code showing a point following the field line going from the poloidal plane at z_k to the poloidal plane at $z_k + \Delta z$. The point does not hit any node of the mesh. An interpolation is needed to know the value of the function at that point.

3.5 Cubic Hermite Spline Interpolation

Interpolation provides a means of estimating the function at intermediate points. Cubic Hermite splines are third degree piecewise polynomials with each polynomial in Hermite form. The Hermite form in 1D consists of two control points and two control tangents for each polynomial.

Consider a 1D function $f(x)$ defined in the interval $0 \leq x \leq 1$, hereby assumed of unit length. The interpolation formula is:

$$f(x) = a(x)f_0 + a(1-x)f_1 + b(x)f_0' - b(1-x)f_1' \tag{3.78}$$

where $a(x) = (1-x)(1+x-2x^2)$, $b(x) = x(1-x)^2$ and explicit use of symmetries has been made.

Moreover,

$$f'(x) = a'(x)f_0 + a'(1-x)f_1 + b'(x)f_0' - b'(1-x)f_1' \tag{3.79}$$

with $a'(t) = -6t(1-t)$ and $b'(t) = (1-t)(1-3t)$. Thus,

$$\lim_{x \to 0^+} f'(x) = f_0' \tag{3.80}$$

and

$$\lim_{x \to 1^-} f'(x) = f_1' \tag{3.81}$$

Continuity:

Continuity is ensured since

$$\lim_{x \to 0^-} f(x) = f_0 \tag{3.82}$$

and

$$\lim_{x \to 1^+} f(x) = f_1 \tag{3.83}$$

Differentiability:

Also differentiability is ensured since for $-1 \leq x \leq 0$ one has

$$f(x) = a(x+1)f_{-1} + a(-x)f_0 + b(x+1)f_{-1}' - b(-x)f_0' \tag{3.84}$$

Leading to

$$f'(x) = a'(x+1)f_{-1} - a'(-x)f_0 + b'(x+1)f_{-1}' + b'(-x)f_0' \tag{3.85}$$

So

$$\lim_{x \to 0^-} f'(x) = f_0'. \tag{3.86}$$

On the other hand, for $1 \leq x \leq 2$ one has

$$f(x) = a(x-1)f_1 + a(2-x)f_2 + b(x-1)f_1' - b(2-x)f_2' \tag{3.87}$$

Leading to

$$f'(x) = a'(x-1)f_1 - a'(2-x)f_2 + b'(x-1)f_1' - b'(2-x)f_2' \tag{3.88}$$

So

$$\lim_{x\to 1^+} f'(x) = f_1'. \tag{3.89}$$

Order of approximation:

Given a function $g(x)$ defined in $0 \le x \le 1$ such that

$$g(0) = f(0); g(1) = f(1); g'(0) = f'(0); g'(1) = f'(1),$$

one can show that

$$g(x) - f(x) = \mathcal{O}(h^4) \tag{3.90}$$

with h being the interval length.

• **Proof:** Use Taylor expansion of g around 0 and 1 as follows

$$g(x) = f_0 + f_0'x + \frac{1}{2}g_0''x^2 + \frac{1}{6}g_0'''x^3 + \mathcal{O}(h^4) \tag{3.91}$$

and

$$g(x) = f_1 + f_1'(x-1) + \frac{1}{2}g_1''(x-1)^2 + \frac{1}{6}g_1'''(x-1)^3 + \mathcal{O}(h^4) \tag{3.92}$$

with $f^n = g^n = \mathcal{O}(h^n)$.

Equating (3.91) and (3.92) yields the following system of 4 equations in 4 unknowns

$$f_0 = f_1 - f_1' + \frac{g_1''}{2} - \frac{g_1'''}{6} \tag{3.93}$$

$$f_0' = f_1' - g_1'' + \frac{g_1'''}{2} \tag{3.94}$$

$$\frac{g_0''}{2} = \frac{g_1''}{2} - \frac{g_1'''}{2} \tag{3.95}$$

$$\frac{g_0'''}{6} = \frac{g_1'''}{6} \tag{3.96}$$

The 4 unknowns g_0'', g_0''', g_1' and g_1''' can then be expressed as a function of f_0, f_0', f_1 and f_1' as

$$g_1''' = 6\left[2(f_0 - f_1) + f_0' + f_1'\right] \tag{3.97}$$

$$g_1' = 6\left(f_0 - f_1\right) + 2f_0' + 4f_1' \tag{3.98}$$

$$g_0'' = -6\left(f_0 - f_1\right) - 4f_0' - 2f_1' \tag{3.99}$$

$$g_0''' = g_1''' = 6\left[2(f_0 - f_1) + f_0' + f_1'\right] \tag{3.100}$$

Plugging these expressions in (3.91) gives

$$\begin{aligned} g(x) &= f_0 + x f_0' - \frac{x^2}{2}\left[6\left(f_0 - f_1\right) + 4f_0' + 2f_1'\right] + x^3\left[2\left(f_0 - f_1\right) + f_0' + f_1'\right] \quad (3.101)\\ &= f_0(1 - 3x^2 + 2x^3) + f_0'(x - 2x^2 + x^3) + f_1(3x^2 - 2x^3) + f_1'(-x^2 + x^3) \end{aligned}$$

The result is expression (3.78) up to $\mathcal{O}(h^4)$.

The formula given by (3.78) is a third order accurate representation of the function if the control points and tangents are given with sufficiently high accuracy. The error is then $O(h^4)$ where h is the interval length. In the case of a two-dimensional function $f(x, y)$ one can write

$$f(x,y) = a(y)f(x,0) + a(1-y)f(x,1) + b(y)f_y(x,0) - b(1-y)f_y(x,1) \quad (3.102)$$

For any point (x, y) in the square $0 \leq x \leq 1$ and $0 \leq y \leq 1$, the $1D$ interpolation at x for $y^* = 0, 1$, i.e: along the red lines illustrated in Fig. 3.2, gives:

$$f(x,y^*) = a(x)f(0,y^*) + a(1-x)f(1,y^*) + b(x)f_x(0,y^*) - b(1-x)f_x(1,y^*) \quad (3.103)$$

For this, one needs to compute the x-derivative at $(0, 0)$, $(0, 1)$, $(1, 0)$ and $(1, 1)$ by a non-centered 5-points stencil scheme as follows:

$$f_x(0,y^*) = -\frac{1}{3}f(-1,y^*) - \frac{1}{2}f(0,y^*) + f(1,y^*) - \frac{1}{6}f(2,y^*) + \mathcal{O}(h^3) \quad (3.104)$$

$$f_x(1,y^*) = \frac{1}{6}f(-1,y^*) - f(0,y^*) + \frac{1}{2}f(1,y^*) + \frac{1}{3}f(2,y^*) + \mathcal{O}(h^3) \quad (3.105)$$

Then interpolate along the green line of Fig. 3.2 by keeping x fixed to get:

$$f_y(x,y^*) = a(x)f_y(0,y^*) + a(1-x)f_y(1,y^*) + b(x)f_{xy}(0,y^*) - b(1-x)f_{xy}(1,y^*) \quad (3.106)$$

where f_{xy} can be evaluated with four control points

$$f_{xy}(0,0) = \frac{1}{4}\left[f(1,1) + f(-1,-1) - f(-1,1) - f(1,-1)\right] + \mathcal{O}(h^4) \quad (3.107)$$

$$f_{xy}(1,0) = \frac{1}{4}\left[f(2,1) + f(0,-1) - f(0,1) - f(2,-1)\right] + \mathcal{O}(h^4) \quad (3.108)$$

$$f_{xy}(1,1) = \frac{1}{4}\left[f(2,2) + f(0,0) - f(2,0) - f(0,2)\right] + \mathcal{O}(h^4) \quad (3.109)$$

$$f_{xy}(0,1) = \frac{1}{4}\left[f(1,2) + f(-1,0) - f(1,0) - f(-1,2)\right] + \mathcal{O}(h^4) \quad (3.110)$$

Or, one may choose to use a centered 5-points stencil scheme in the bulk and non-centered scheme only at the boundaries where the centered scheme is not defined. In that case the centered derivatives write:

$$f_x(0,y^*) = \frac{1}{12}f(-2,y^*) - \frac{2}{3}f(-1,y^*) + \frac{2}{3}f(1,y^*) - \frac{1}{12}f(2,y^*) + \mathcal{O}(h^4) \quad (3.111)$$

$$f_x(1,y^*) = \frac{1}{12}f(-1,y^*) - \frac{2}{3}f(0,y^*) + \frac{2}{3}f(2,y^*) - \frac{1}{12}f(3,y^*) + \mathcal{O}(h^4) \quad (3.112)$$

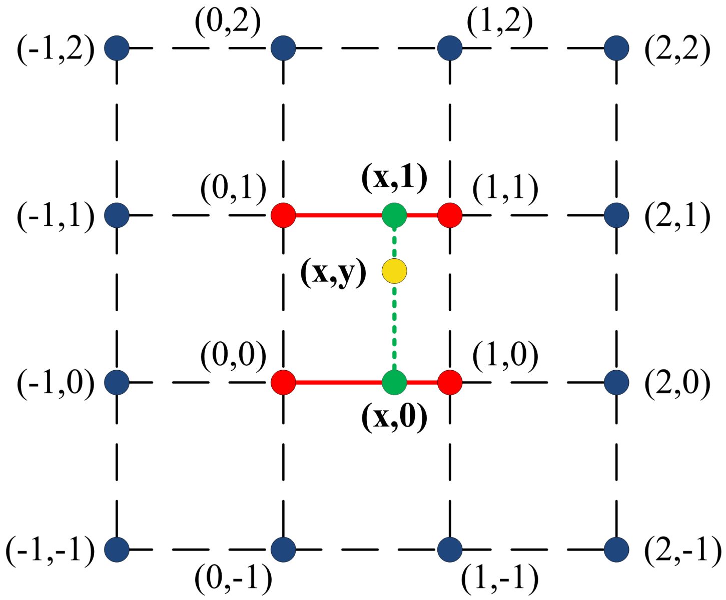

Figure 3.2: The stencil of 16 control points needed for estimating the value of the function at an intermediate point (x, y)

Similarly for f_y and f_{xy}. Hence, the resulting interpolation given by Eq. (3.102) at the yellow point (x, y) requires 16 control quantities as illustrated in Fig. 3.2 and it is 4^{th} order accurate if these quantities are known to sufficiently high accuracy; the error is again $\mathcal{O}(h^4)$ for a unit square of side h. In the code, derivatives are computed using the routine `generate_deriv` described in Sec. 3.2.4, and this interpolation scheme is embedded in the routine `interp`. This procedure is faster than the usual spline approach which requires the solution of a linear problem, and not less accurate. Accuracy also depends on the scale length of the function. For a function characterized by a wavenumber k and represented by N points in a given box, a simple scaling argument based on replicating the number of boxes shows that the actual error scales like $(k/N)^4$.

We compared the maximum error given by the above interpolation scheme to the one given by linear interpolation, by a MATLAB cubic spline interpolation routine, by a 4^{th} order Hermite interpolation with non-centered evaluation of derivatives and a 4^{th} order Hermite interpolation with an exact value of the derivatives. The errors given by the different interpolation schemes are presented in Fig. 3.3. We show that the 4^{th} order Hermite cubic interpolation with 4 points centered derivatives (solid red line with no marks) is as accurate as the 4^{th} order MATLAB cubic spline interpolation.

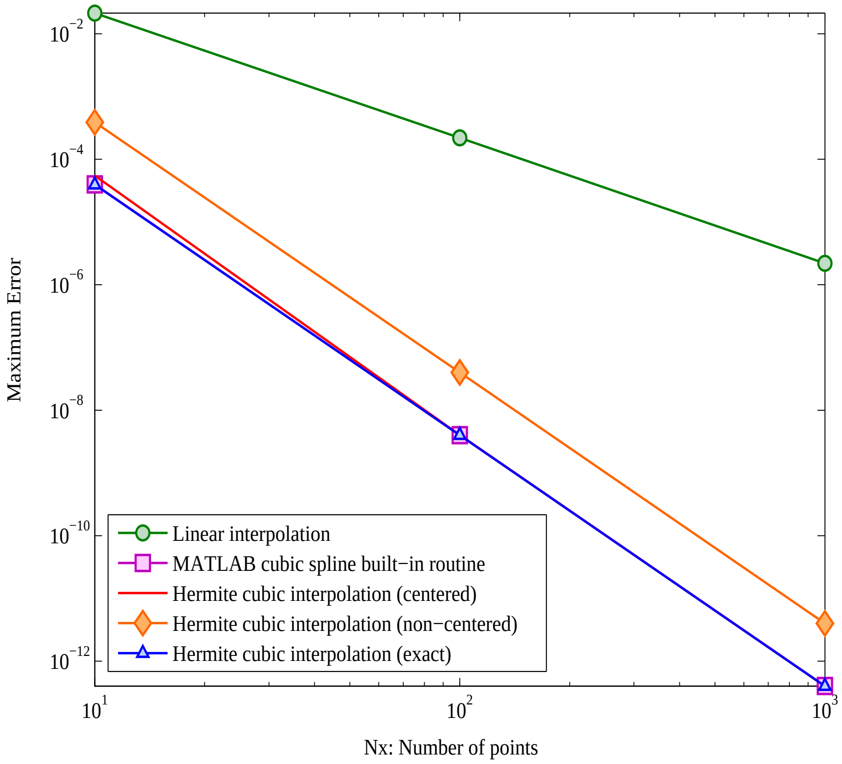

Figure 3.3: The errors given by the different interpolation schemes show that the 4^{th} order Hermite cubic interpolation is as good as the 4^{th} order cubic spline interpolation

3.6 Summary of the FENICIA scheme

A general scheme of FENICIA is shown in Fig .3.4. The code relies on an operator splitting general scheme defined as

$$\partial_t L\, S = E(S) + I.S$$

This is intended to show the generality of the scheme implemented in FENICIA and the possibility to easily change/replace existing numerical techniques. In the present version of the code, this class is advanced with a Leap-frog time advancing scheme, stabilized by a predictor corrector. The G solver for the reduced equation discussed in section 3.2.6 uses an iterative scheme. Alternatively, in future work, one may swap those schemes out for other explicit, implicit or iterative numerical methods. Furthermore, the FCI coordinate system is used in the parallel direction whereas in the transverse plane, Cartesian coordinates are considered. Once again, other coordinate systems may be implemented with minimal changes in the code affecting only one routine. In the perpendicular direction, a polar coordinate system is plausible. In what concerns the mesh, finite differences with uniform meshing are implemented. Any other grid-type can be implemented as well. This is indeed possible because the mesh is totally decoupled from the magnetic field geometry. Mainly, circular concentric surfaces, sheared slab and island geometries are considered in the present version of the code. However, non-axisymmetric geometries are also possible cases that could be handled. Further investigations need to be done in this regard (see Chapter 2). Many physics problems have been studied and implemented so far to test the code and validate it. Among them, a 2D Navier-Stokes model, a wave equation model, a drift-wave model and an ITG nonlinear model. Nonetheless, it is important to mention that any other model belonging to (1.19) can be implemented. Finally, boundary conditions for the cylindrical case are such that the fields are set to zero outside the plasma radius rc and the rectangular box is periodic in the z direction. In the island case, with a slab geometry, periodicity is also applied in the y direction. An important aspect of FENICIA is that it's very modular, thus allowing easy swaping out of numerical techniques. Modularity is better seen through the Flowchart presented in Fig. 3.5.

In order to start a run, one needs to create a test file in the directory `FENICIA/tests` along with an `input_file` containing the different physical parameters of the simulation. At the start of a simulation, the program makes use of several modules. The module `parameters` contains all the parameters and variables that are initialized and not changed during the execution. The module `pputils` contains subroutines for dealing with the MPI parallel processing (Thanks to P. Hill who parallelized the code in the z direction. Scaling studies are still ongoing). Solvers for the time integration scheme are in the module `solvers`. Two main solvers are considered: `time_pc` for advancing the system using predictor-corrector, and `time_lf` for advancing the system using Leap-frog. In addition, the module `setup` is concerned with setting up equilibrium profiles and initialization of the geometry including the map to follow the field lines. The module `ITG_Physics` contains subroutines of the ITG problem. Another separate module contains physics of a drift-wave model called `DW_Physics`. The module `readinput` contains subroutines to read input parameters and initial states from the `input_file` and sets the various global parameters not defined in the `input_file`. The diagnostics routines are in the module `diagnostics`, particularly the file `output`. Finally the module `restarts` reads and writes the restart files.

Let it be the time loop index, nt the number of time steps and $ntpc$ is how often to use predictor-corrector. After initializing the run, the main loop starts at $it = 1$ and repeats itself as long as $it < nt$. IThe predictor-corrector is used every nt steps, otherwise the Leap-frog is used. At the end of each iteration, the data is saved either in unformatted file format or in HDF5 file format. Then, depending on whether the user wishes or not to restart the simulation at a certain it, the program either saves the restart files or not. The final step is closing all the open files and finishing the mpi process. At the end of the simulation, the data is saved into the file `output.h5` in HDF5 format. As an option, each state can be also saved in separate `.dat` unformatted format files.

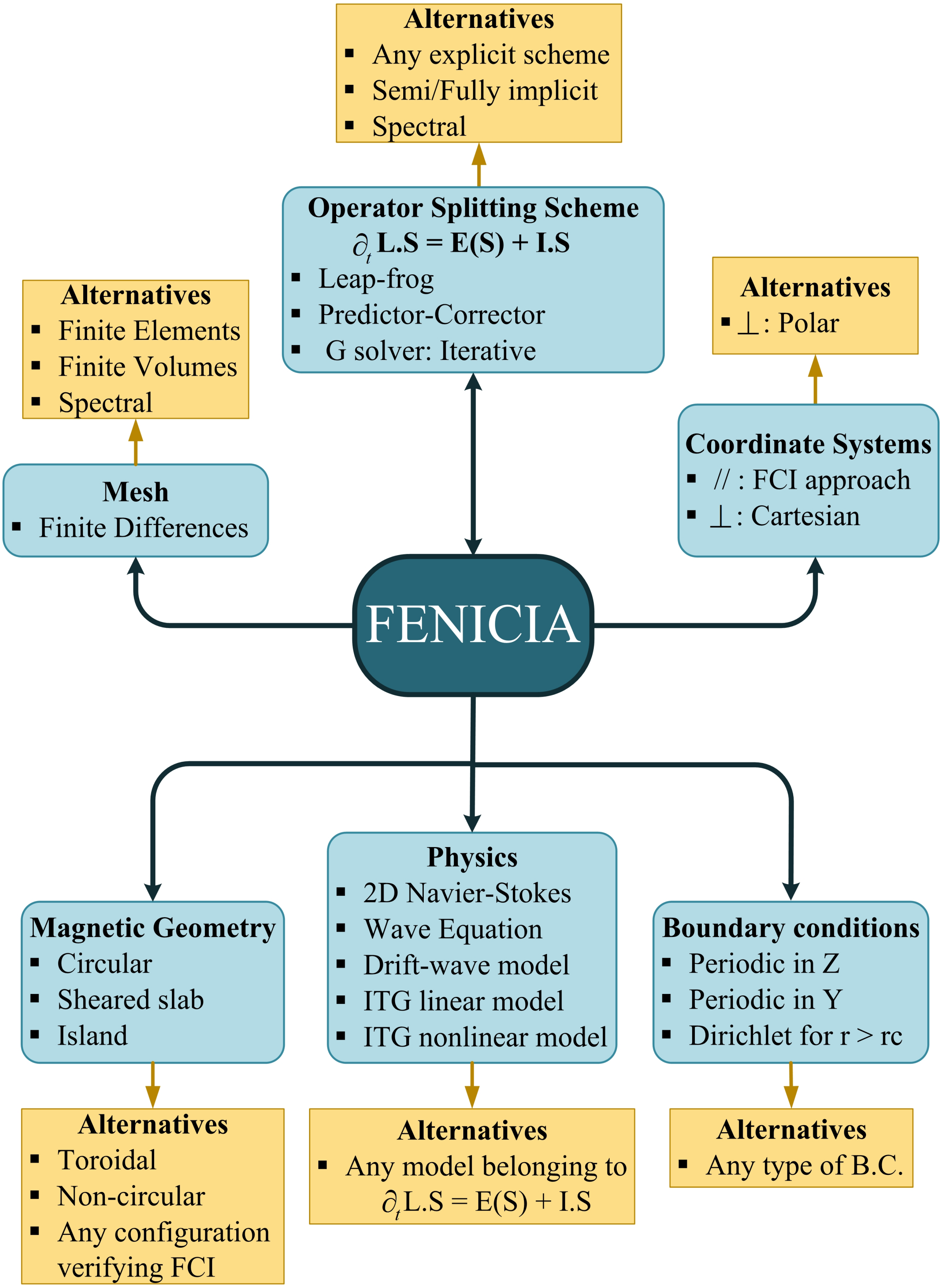

Figure 3.4: scheme

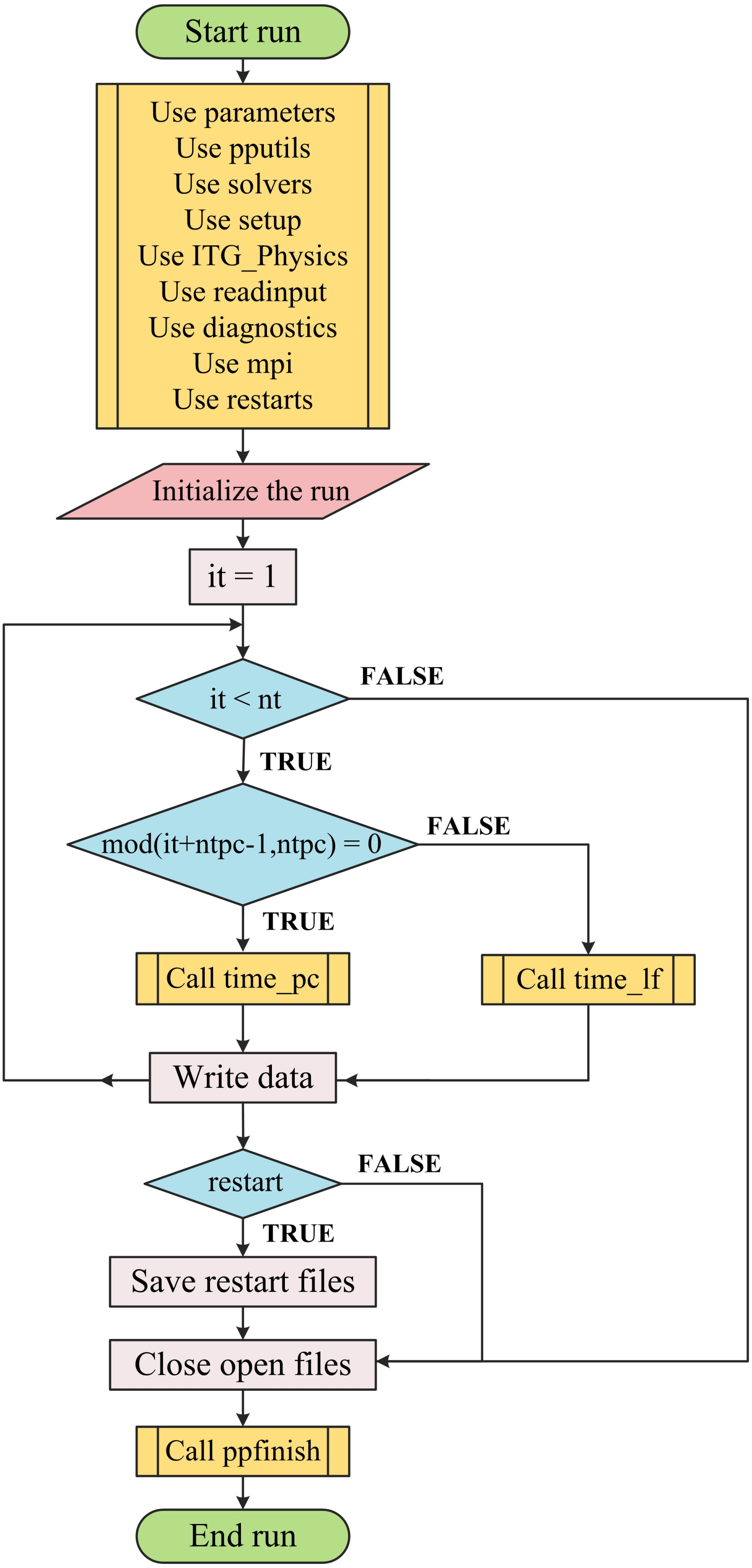

Figure 3.5: Flowchart

Chapter 4

Implementation and Qualification of the FCI Approach

يَا جَامِعَ العِلمِ نِعمَ الذُّخرُ تَجمَعُهُ،

لَا تَعدِلَنَّ بِهِ دُرًّا وَ لَا ذَهَبَا

مُؤَيِّد الدّين الأَصبَهَاني (. - ٥١٣ ٥)

Contents

Aquarelle et Craie de cire, (F. Hariri, 2004)

The FCI approach discussed in Chapter 2 has been implemented in FENICIA [Hariri 2013]. In this Chapter, I present several numerical tests carried out with FENICIA to qualify the new method and the code using various models belonging to the general class, Eq. 1.19. These are of three types: a) tests to validate the Hermite interpolation scheme discussed in Section 3.5 by showing that numerical diffusion can be kept to the desired level at a minimum computational cost, b) tests to validate the FCI approach by demonstrating the capability of the new method to simulate wave propagation accurately even when the toroidal mode number exceeds the Nyquist cut-off (half the number of toroidal points) at the given toroidal resolution. This is precisely the situation where the straightforward approach that computes the parallel derivative as a combination of the toroidal and poloidal derivatives would fail, and c) tests that validate the code FENICIA: efficiency of operators in the poloidal plane is tested using a 2D Navier-Stokes model and properties of a linear ITG instability are verified using a 3D reduced ITG slab model. The main result is that the growth rate obtained from analytical perturbation theory and the numerical growth rate are consistent. All the tests were carried out with a safety factor profile $q(r) = 1 + 2r^2$. The nonlinear results will be discussed more fully in Chapter 5.

4.1 Validation of the interpolation scheme

4.1.1 Estimate of the numerical diffusion

The use of interpolation in the perpendicular plane introduces unavoidable numerical diffusion, in particular in the radial direction. It is then important to assess whether numerical diffusion can be kept to the desired low level such that transport coming from actual physical mechanisms is not substantially affected.

In order to quantify numerical diffusion, it is convenient to set up initial conditions such that the physical diffusion is theoretically zero. This can be done by working directly with model (1.20) and choosing an initial condition such that all the fields depend only on the radial coordinate r (zonal fields). Since the action of the parallel gradient on such fields is null, any such initial condition should not evolve in time. Thus, any measured radial diffusion in such a system can be attributed to numerics.

For convenience, we initially choose a special case describing the propagation of the sound wave in one direction only:

$$\partial_t n + \frac{c_s}{R}\nabla_\parallel n = 0 \tag{4.1}$$

where $\nabla_\parallel = \partial_\varphi + 1/q(r)\partial_\theta$, c_s is the ion sound speed and R is the major radius. In the actual tests of the code, c_s/R is set to 1 with the time t normalized to R/c_s.

For a simple upwind scheme, one can estimate the effective numerical $\nabla_\parallel$ to be

$$\nabla_\parallel^{eff} = \frac{n(s+\Delta s) - n(\Delta s)}{\Delta s} \approx \frac{E_{interp}}{\Delta \varphi}, \tag{4.2}$$

where E_{interp} is the interpolation error and $\Delta s = \Delta\varphi = 2\pi/Nz$ is the distance along the field-aligned coordinate. Note that, numerically, $n(s+\Delta s)$ differs from $n(\Delta s)$ even for zonal fields because of the interpolation error.

As discussed previously in Sec. 3.5, $E_{interp} \approx (k/N_x)^\alpha$ where k is the number of waves in a grid of $N_x \sim N_y$ points in the perpendicular plane and α depends on the interpolation scheme, with $\alpha = 4$ for cubic Hermite interpolation employed here.

The rate γ_{num} associated with the numerical diffusion can be estimated as

$$\gamma_{\text{num}} \approx \frac{c_s}{R}\nabla_\parallel^{eff} \approx \frac{c_s}{R}\left(\frac{k}{N_x}\right)^\alpha \frac{1}{\Delta\varphi} \tag{4.3}$$

This diffusion rate must be compared to the rate γ_{phys} of the physical phenomenon one wants to study. We consider two possible physical timescales of interest. One is the energy confinement time given by the gyro-Bohm estimate

$$\tau_E \sim \rho_*^{-2}\frac{a}{c_s}, \tag{4.4}$$

which must be compared to (4.3) computed at the profile scale length, that is at $k = 1$.

Another is the turbulence characteristic time at a given wavelength, which is of the order of the drift-wave period

$$\tau_w \sim \frac{a}{c_s}\frac{2\pi}{k_\perp \rho_s}, \tag{4.5}$$

where a is the minor radius, $\rho_* = \rho_s/a$, and $k_\perp$ is related to the number of waves by $k_\perp = 2\pi/\lambda = \pi k/a$. Thus,

$$\tau_w \sim \frac{a}{c_s}\frac{\pi}{k\rho_*} \tag{4.6}$$

Moreover, any sensible simulation must resolve ρ_s. This puts a constraint on N_x. If one stipulates that at least four points are needed to resolve ρ_s one has

$$N_x \geq \frac{8}{\rho *} \tag{4.7}$$

Numerical diffusion is negligible when $\gamma_{\text{num}} \ll \gamma_{\text{phys}}$, that is when the following two conditions hold:

$$\gamma_{num}\tau_E \ll 1, \tag{4.8}$$

and

$$\gamma_{num}\tau_w \ll 1. \tag{4.9}$$

An estimate of $\gamma_{num}\tau_E$ is given by

$$\gamma_{num}\tau_E \approx \left(\frac{a}{R}\right)\left(\frac{1}{N_x}\right)^{\alpha}\left(\frac{1}{\Delta\varphi}\right)\left(\frac{N_x}{2}\right)^{2} \leq \frac{1}{4\Delta\varphi}\frac{a}{R}\left(\frac{\rho_*}{8}\right)^{\alpha-2}, \tag{4.10}$$

showing that condition (4.8) is easily satisfied since $\alpha = 4$ and $\rho*$ is small. Moreover, an estimate of $\gamma_{num}\tau_w$ is given by

$$\gamma_{num}\tau_w \approx \left(\frac{a}{R}\right)\left(\frac{k}{N_x}\right)^{\alpha-1}\left(\frac{N_z}{2\pi}\right) \tag{4.11}$$

One can foresee that, for well resolved waves, k/N_x is sufficiently small that (4.11) is much less than one. A test is presented in the following section.

4.1.2 Testing numerical diffusion with a zonal field

The first test is carried out on Eq. (4.1) and a zonal field as an initial condition (see Fig. 4.1):

$$n_0 = cos(7k\pi r) + 1 \tag{4.12}$$

with this initial condition, $\nabla_{\|} = 0$. Thus any diffusion observed in the test must be attributed to numerical diffusion. In Fig. 4.2, we plot the product $\gamma_{num}\tau_w$ as a function of the number of points per wavelength Nx/k. One notes that for points in the rightmost part of the abscissas, corresponding to well resolved waves, the numerical diffusion is negligible $\sim 10^{-10}$. However, even for cases that are badly resolved (leftmost part of the abscissas) and that one would not consider adequate for simulations, the numerical diffusion is nearly $\sim 10^{-2}$. Thus, condition (4.9) is always satisfied for any practical purposes.

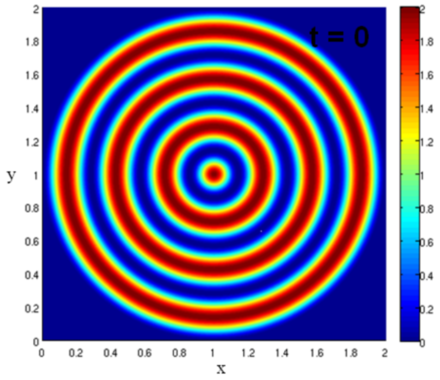

Figure 4.1: A zonal flow to test numerical diffusion

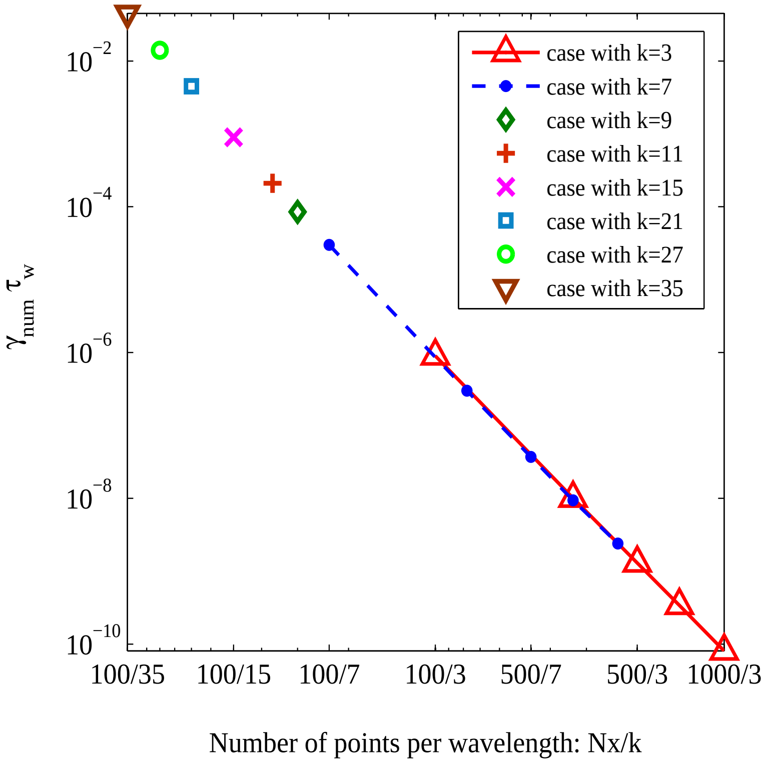

Figure 4.2: The evolution of $\gamma_{num}\,\tau_w$ as a function of the number of points N_x per wavelength k. The slope is indeed equal to -3 as expected given that $\alpha = 4$

4.2 Validation of the FCI approach

4.2.1 Testing the ability of the code to simulate sound waves with a small toroidal resolution

We now show that the code FENICIA is able to simulate drift-wave propagation with high accuracy even when the mode number in the toroidal (z) direction exceeds the Nyquist cutoff $N_z/2$. Tests were carried out for both Eq. (4.1) and the full model of Eq. (1.20). In the latter case, setting ρ_* to zero allows one to obtain analytic solutions of the wave propagation, which turns out useful for testing purposes. For the density, we employ initial conditions of the form:

$$N_0 = g_0(r) \times cos(m\theta - n\varphi), \tag{4.13}$$

with

$$g_0(r) = \exp\left[-\frac{(r-r_s)^2}{r_s^2}m^2\right] \times \left(\frac{r}{r_s}\right)^m \times \left(\frac{r-a}{r_s-a}\right)^2 \tag{4.14}$$

where r_s is the position of the rational surface such that $q(r_s) = m/n$. Notice that the Gaussian can be recast as follows: $\exp\left(-k_\parallel L_s\right)^2$ with $k_\parallel = (n + m/q)/R$ and $L_s = s/qR$. Indeed, one finds by Taylor expansion that

$$k_\parallel(r) \approx (r - r_s)\left.\frac{d\,k_\parallel}{d\,r}\right|_{r_s} = -(r - r_s)\frac{m}{r_s\,L_s}$$

The latter expression ensures that the magnitude of the mode almost vanishes for large wave vectors such that $k_\parallel L_s > 1$.

The equilibrium density profile is such that

$$\log(n_0) = -\frac{1}{2L_n}(r^2 - a^2), \tag{4.15}$$

in the full model (1.20). This corresponds to a class of drift-waves with uniform drift frequency $\omega_{*n} = m/L_n$. The analytic solutions are superpositions of waves propagating with frequencies

$$\omega_\pm = \frac{m}{2L_n} \pm \sqrt{\left(\frac{m}{2L_n}\right)^2 + A^2\left(1+\frac{1}{\tau}\right)\left(\frac{m}{q(r)} - n\right)^2} \tag{4.16}$$

For the tests shown here the box size is $400 \times 400 \times 20$ and $m/n = 2$, with (m, n) ranging from $(4, 2)$ to $(30, 15)$. I start by showing results obtained from Eq. (1.20) with $\log(n_0) = 0$ (zero drift frequency). The initial velocity is such that there is a single wave propagating at frequency $\omega = A(1 + 1/\tau)^{1/2}(m/q(r) - n)$.

Figure 4.3 shows the density pattern obtained with $m = 8$ and $n = 4$ at $t = 0$ and $t = 0.5$. One observes that initially the vortices are round, whereas later they are sheared by the differential rotation due to the radial dependence of the wave frequency. Next, we consider a case with finite drift frequency and $L_n = 0.25$.

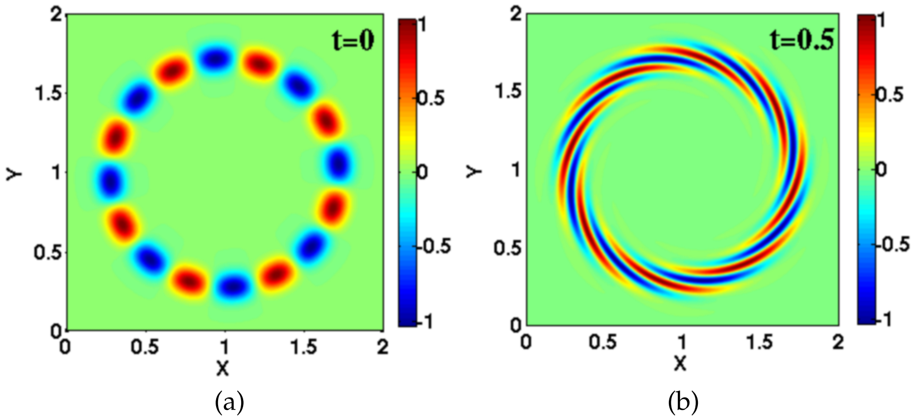

(a) (b)

Figure 4.3: For the sound wave case: (a) Density at $t = 0$; (b) Density at $t = 0.5$

Note that in the version of the code employed for these tests, the drift frequency term is computed directly in its Poisson bracket form with the Arakawa scheme as if it was a nonlinear term as discussed in Appendix A.

Figure 4.4 shows that after a while the potential develops the characteristic pattern with two lobes which one finds also in the slab branch of ITG instability. This occurs when the frequency has a local extremum at the rational surface, as in Eq. (4.16) when the density gradient is nonzero. We now assess the overall accuracy of the algorithms by measuring the cumulative error per unit time.

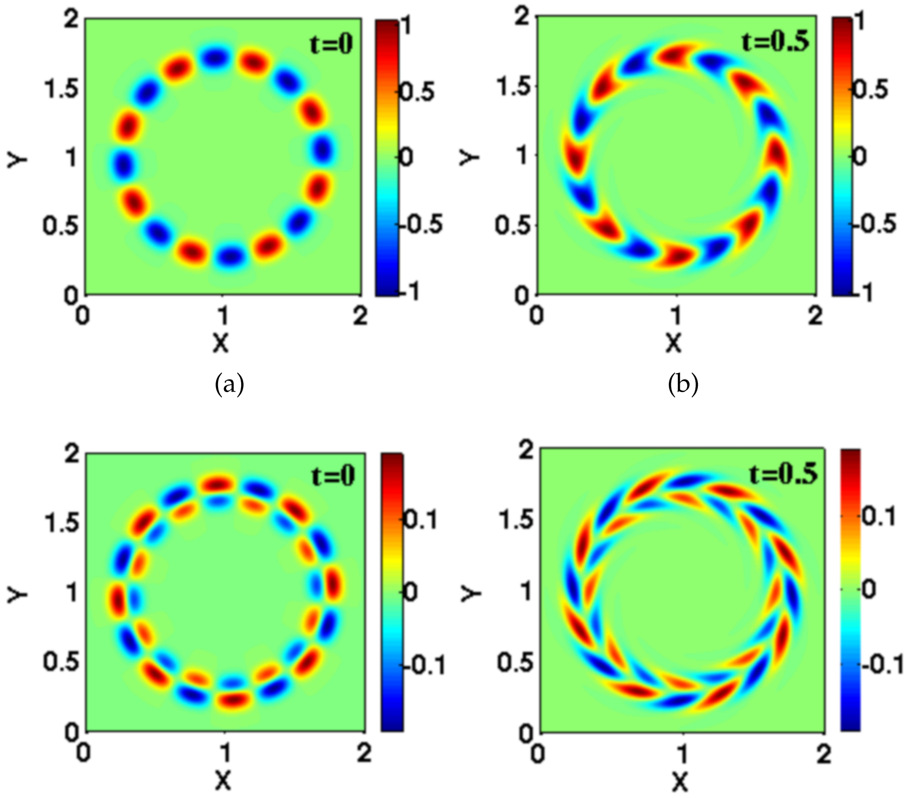

(a) (b)

(c) (d)

Figure 4.4: For the drift-wave case: (a) Density at $t = 0$; (b) Density at $t = 0.5$; (c) Velocity at $t = 0$ and (d) Velocity at $t = 0.5$

This is obtained by computing the norm of the difference between the numerical solution and the exact solution obtained analytically. It turns out that this norm grows linearly with time, so its time derivative is a reliable measure of the error. The overall algorithms are adequate if this quantity, which has the dimensions of a rate (time^{-1}), is much smaller than the rate of the physics processes one wants to study.

The results are summarized in Fig. 4.5 where the error per unit time $E = (<(n_{exact} - n_i)^2 > / < (n_{exact})^2 >)^{1/2}$ is plotted as a function of the poloidal mode number for three cases: 1) the full model (1.20) with $L_n = 1/4$ and $A = 12.5$, 2) the same model with $1/L_n = 0$ (no density gradient), and 3) the model with $A = 0$. The latter case tests the effect of switching off the parallel dynamics so that the system reduces effectively to

$$\partial_t n + [n, log(n_0)] = 0 \tag{4.17}$$

The first thing to notice is that all the tests give an error per unit time much less than one. We remark that the relative difference between case **1** and case **3** is less than 10^{-3}, which explains why the data points for the two cases look almost superposed in Fig. 4.5. Since the model is normalized to the Bohm timescale $a^2/(\rho_s c_s)$, any physics effect occurring on a shorter time scale is treated accurately.

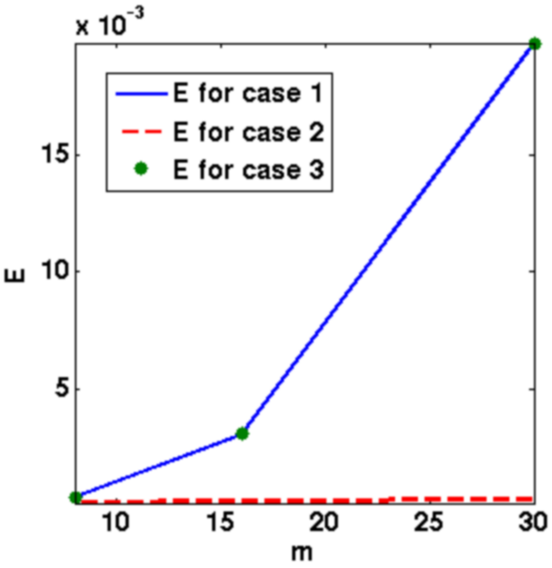

(a)

Figure 4.5: The relative error between the exact and the numerical solution as a function of the poloidal wavenumber m. For case **1**: full model with finite drift frequency, we get the blue solid line; For case **2**: full model with zero drift frequency, we get the red dashed line; For case **3**: reduced model of Eq. (4.17) without sound wave terms, we get the green bullets

This is the case, in particular, of plasma micro-turbulence, whose characteristic frequency ranges from the drift frequency (evaluated at the Larmor radius scale length), down to about a tenth of it, still much larger than one in Bohm units.

It is also apparent that the best results are obtained when the density gradient is switched off (case **2** in the red dashed line). Thus the error associated with the computation of the parallel dynamics is negligible with respect to the error due to the perpendicular dynamics. This is not difficult to understand as discussed below. Note also that the dependence on m of the error associated with the parallel dynamics is weak, and that one obtains accurate results even when $m = 30$, such that $n = 15$ exceeds the Nyquist cutoff. This proves the capability of the method to deal with microscopic vortices, such as those produced by plasma turbulence, with a limited number of points in the toroidal (z) direction.

There are two sources of error in the parallel dynamics algorithm, one coming from the interpolation in the perpendicular plane, which is small as discussed in Sec. 3.5, and the other coming from the discretization along the field lines. This can be kept to the desired accuracy, but the results shown here demonstrate that second order finite differences are adequate even with a moderate number of points along z, as a consequence of weak gradients along the field lines.

By comparison, one can see that the second order accurate Arakawa scheme produces errors that scale like m^3. Indeed Eq. (4.17) describes advection of the field n in the flow of the stream function $\log(n_0)$. It is shown in Appendix B that treating with a second order algorithm the problem of the propagation of a wave with large wavenumber k gives an error of $O(k^3 \Delta x^2)$ as obtained here. Note that the Arakawa scheme is commonly used in numerical simulations of plasma turbulence and it is often considered adequate. Thus, the fact that the parallel dynamics scheme developed in this work contributes little to the overall algorithmic error, which is dominated by the Arakawa discretization in the perpendicular plane, makes it a safe choice for further code development.

4.3 Validation of the code FENICIA

Code validation is important for it ensures that the code is correct. Numerous tests focusing on specific physics problems can be considered and used to prove that the numerical results comply with the analytical calculations. Thus, allowing an efficient validation of the output. In the first place, we chose to perform a test on a two-dimensional Navier-Stokes model in order to assess the efficiency and accuracy of the 2D operators.

4.3.1 Testing the efficiency of 2D operators

The focus was firstly on testing the efficiency of operators in the poloidal plane. For that purpose, the Navier-Stokes 2D problem was implemented

$$\begin{cases} \partial_t \omega + [\phi, \omega] = \nu \, \nabla^2 \omega \\ \\ \omega = \nabla^2 \phi \end{cases} \tag{4.18}$$

which describes the evolution of the vorticity denoted by ω over time with ν being the viscosity and ϕ the electrostatic potential. This model contains both the Laplace operator solved by FFTs and the Poisson bracket nonlinear term discretized using the Arakawa finite differences scheme. We start the simulation at $t = 0$ by an array of vortices and we try to study the evolution of the vorticity with/without viscosity. The vorticity is initialized by

$$\omega = sin(\pi x) \, \times \, sin(\pi y) \tag{4.19}$$

on a domain defined by $nx = ny = 100$ grid points in both the x and y directions. Boundary conditions are such that $\phi = 0$ outside the plasma radius $rc = 1$. Figure 4.6 shows the vorticity at $t = 0$ and at $t = 5$. Where the time scale corresponds to one eddy turn over time of the largest vortex. It is normalized by L/v where L is the system's size and v is the velocity at large scales. One observes that vortices are carried around over time and sheared by the flow.

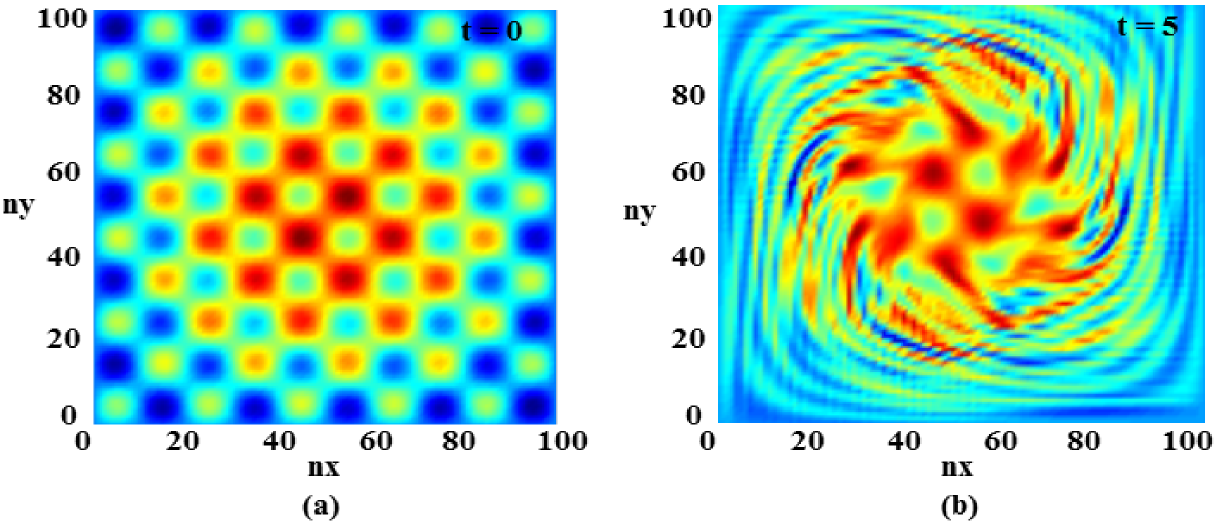

Figure 4.6: **(a)**: vorticity at $t = 0$; **(b)**: vorticity at $t = 5$

We then test the efficiency of the Jacobian expression of the advection term by checking the conservation of the mean kinetic energy defined by

$$E = \frac{1}{2}\int v^2 \mathrm{d}x\,\mathrm{d}y \tag{4.20}$$

or equivalently

$$E = \frac{1}{2}\sum_k k^2|\phi_k|^2 \tag{4.21}$$

and the mean square vorticity written as

$$U = \frac{1}{2}\int \omega^2 \mathrm{d}x\,\mathrm{d}y \tag{4.22}$$

or equivalently

$$U = \frac{1}{2}\sum_k k^4|\phi_k|^2 \tag{4.23}$$

where $\omega = \vec{\nabla} \times \vec{v}$ and k is the wavenumber. It is expected that the conservation of the latter quantities will be guaranteed by the use of the Arakawa FD scheme. That is, both E and U are conserved quantities in the absence of any dissipation $\nu = 0$. To verify it, we start by setting $E = U = 1$ then we plot the relative variation of each of the quantities over a time scale breaking at $t = 10$. The result in Fig. 4.7 shows that energy is conserved up to 10^{-7} and enstrophy is conserved up to 10^{-4}. The non-conservation of these quantities comes from the excitiation of small scales in the nonlinear regime, up to the Nyquist cut-off. This results from the shearing of eddies by vortex flows, as discussed earlier.

The second test on this model is performed with viscosity $\nu = 10^{-3}$ with the same initial condition and parameters as the previous test. We notice that when

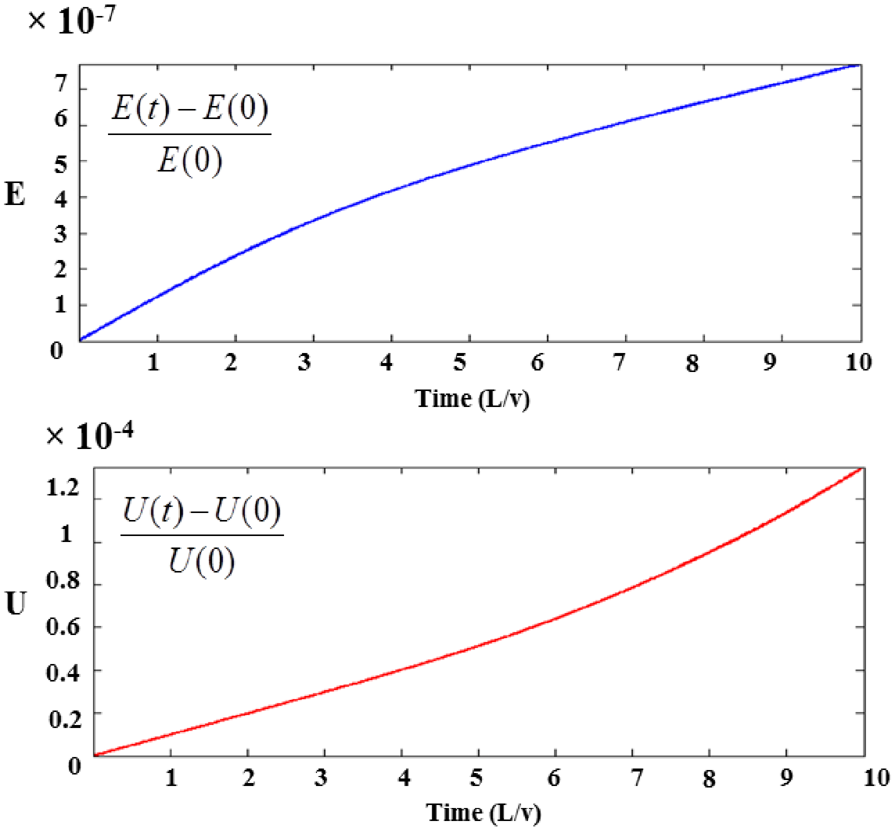

Figure 4.7: Testing the advection operator (Arakawa's scheme) shows conservation of Energy(E) and Enstrophy(U)

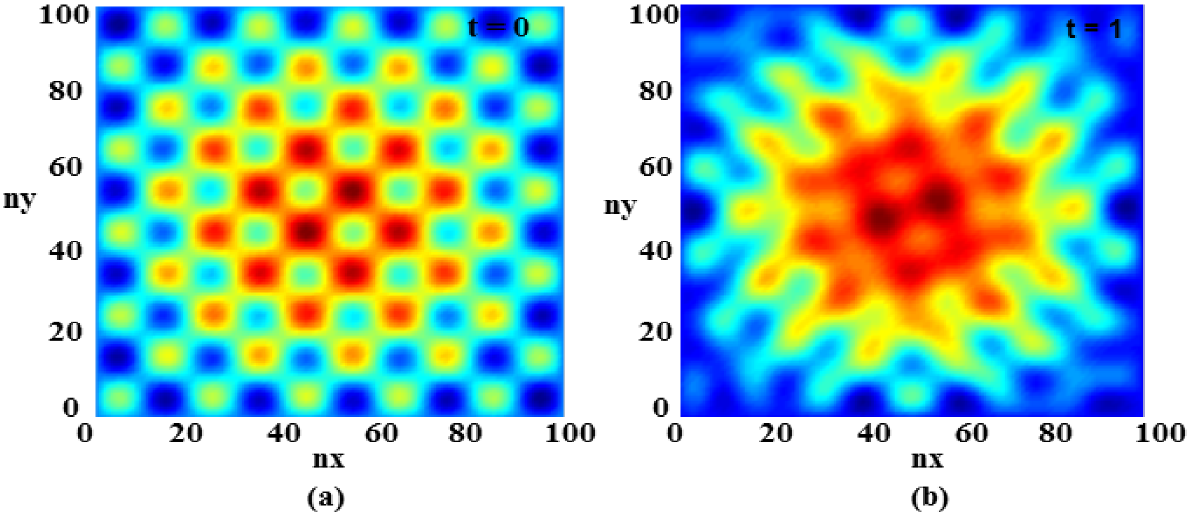

Figure 4.8: (a): vorticity at $t = 0$; (b): vorticity at $t = 1$

viscosity is added, fast dissipation of small scales occurs as shown in Fig. 4.8 where vortices at $t = 1$ are already dissipated.

This is reflected in Fig. 4.9 by a fast decay of enstrophy until $t = 1$ when all small vortices have been dissipated. After $t = 1$, energy and enstrophy decay at the same rate. Expressions 4.21 and 4.23 explain this behavior. Enstrophy is mainly dominated by small scale ($\sim k^4$) whereas energy is dominated by large scales ($\sim k^2$). So gradients are much more steep in enstrophy than in energy which explains why adding viscosity affects mainly the enstrophy. Therefore, dissipative terms are also validated through this test.

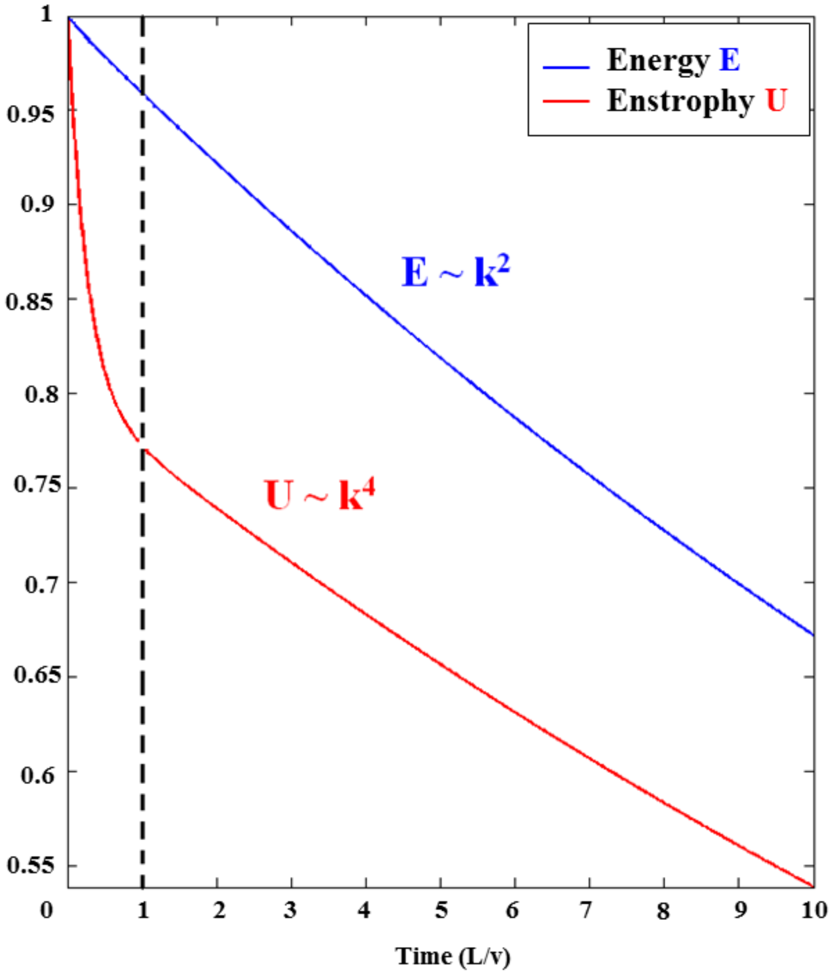

Figure 4.9: Decay of Energy(E) and Enstrophy(U) over time due to the addition of viscosity

4.3.2 Verifying properties of a linear ITG instability

To fully check the forgoing 3D version of the code, what is left is to assess the feasibility of the parallel gradient. It is useful to consider a simplified linear ITG slab model belonging to (1.19) and verify whether the numerical results are in accordance with the analytical properties of a linear ITG instability. For that purpose, the following linear model was considered

$$\begin{cases} \partial_t\tilde{\phi} + C_\parallel \nabla_\parallel u_\parallel = 0 \\ \partial_t u_\parallel + C_\parallel \nabla_\parallel T_\parallel = 0 \\ \partial_t T_\parallel + \vec{v}_E.\vec{\nabla}_\perp T_{\parallel 0} = 0 \end{cases} \tag{4.24}$$

In Fourier space this system leads to

$$\begin{cases} \omega\,\tilde{\phi} = k_\parallel C_\parallel u \\ \omega\, u = k_\parallel C_\parallel T_\parallel \\ \omega\, T_\parallel = -\tilde{\phi}\,\frac{m\,\partial T_{\parallel 0}}{r\,\partial r} \end{cases} \tag{4.25}$$

One can then deduce the linear dispersion relation

$$\omega^3 = (k_\parallel C_\parallel)^2 \omega_{*T} \tag{4.26}$$
$$\Longrightarrow \omega = \mathrm{e}^{i(\pi+2\ell\pi)/3}\omega_R \quad \text{with} \;\; \ell \in \mathbb{Z}$$

where I refer to the linear frequency obtained from this dispersion relation with the notation $\omega = \omega_R + i\gamma_{theory}$. ω_R being the real frequency and γ_{theory} being the theoretical growth rate. Furthermore,

$$\omega_{*T} = -\frac{m\,\partial T_{\parallel 0}}{r\,\partial r} \tag{4.27}$$

and

$$\omega_R = \mid (k_\parallel C_\parallel)^2 \omega_{*T} \mid^{1/3} \tag{4.28}$$

The equilibrium parallel temperature profile is given by

$$T_{\parallel 0}(r) = \begin{cases} -\frac{1}{2}(r^2 - r_c^2) & \text{if } r < r_c \\ 0 & \text{if } r > r_c \end{cases} \tag{4.29}$$

Note that here $C_\parallel = 1/\rho_*$ with $\rho_* = 8 \times 10^{-2}$ and $r_c = Lx/2$, that is half the box length in the *x*-direction. We then consider the following parameters: The number of points in the *x*, *y* and *z* directions are chosen as $nx = 100$, $ny = 100$, $nz = 20$. The lengths in each direction are given by $Lx = 2$, $Ly = 2$, $Lz = 1$. And the poloidal and toroidal wavenumbers (m, n) are respectively set to $(4, 2)$. Once again, we employ initial conditions of the form:

$$T_\parallel(t=0) = g_0(r) \times cos(m\theta - n\varphi), \tag{4.30}$$

$$\tilde{\phi}(t=0) = g_0(r) \left(\frac{k_\parallel C_\parallel}{\omega_0}\right)^2 cos(m\theta - n\varphi + \frac{2\pi}{3}) \tag{4.31}$$

$$u_\parallel(t=0) = g_0(r) \left(\frac{k_\parallel C_\parallel}{\omega_0}\right) cos(m\theta - n\varphi - \frac{2\pi}{3}) \tag{4.32}$$

with

$$g_0(r) = \exp\left[-\frac{(r-r_s)^2}{r_s^2}m^2\right] \times \left(\frac{r}{r_s}\right)^m \times \left(\frac{r-a}{r_s-a}\right)^2 \tag{4.33}$$

where $r_s = \sqrt{(m/n-1)\, r_c^2/2}$ is the position of the rational surface such that $q(r_s) = m/n$, q being the safety factor written as $q = 1 + 2(r/rc)^2$. Upon using these parameters, the theoretical growth rate given by the imaginary part of the frequency $\sim e^{\gamma_{theory} t}$ writes

$$\gamma_{theory} = \frac{\sqrt{3}}{2}\omega_R \tag{4.34}$$

For the sake of testing the code, we chose a constant q profile equal to 1, thus setting $k_{\parallel} = m/q - n = 2$. In that case, the resulting growth rate is

$$\gamma_{theory} \approx 11.7 \tag{4.35}$$

The numerical growth rate γ_{num} obtained with the above parameters is given by the graph in Fig. 4.10 which describes the evolution of the energy over time on a logarithmic scale. Comparing $\gamma_{theory} = 11.7$ to $\gamma_{num} = 11.4$ allows one to conclude that the match between theoretical and numerical growth rates is indeed very good.

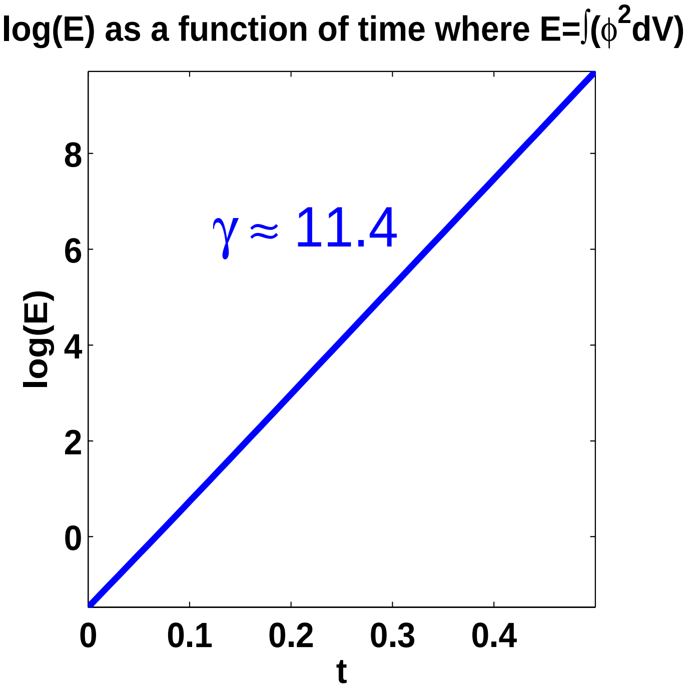

Figure 4.10

In addition, the real frequency ω_R given by Eq.(4.28) scales with $k_{\parallel}^{2/3}$. Hence, at the resonant surface, eigenmodes are not expect to undergo any rotation. However, in regions outside the resonant surface where $k_{\parallel} \neq 0$, rotation frequency should lead to rotation and stretching. The simulation run with the former parameters and an initial condition for temperature taken as in Fig. 4.11 (a), provides evidence regarding the validity of the results. In part (b) of this figure, it is shown that at the position of the resonant surface, the initial mode does not rotate and stands unchanged. Conversely, in regions of nonzero $k_{\parallel}$ we observe deformations and rotation due to the rotation frequency. Hence, the numerical results correspond to the appropriate theoretical calculations. This enabled us to validate the computed results provided by the code and to guarantee that the tests produce the concerned physics.

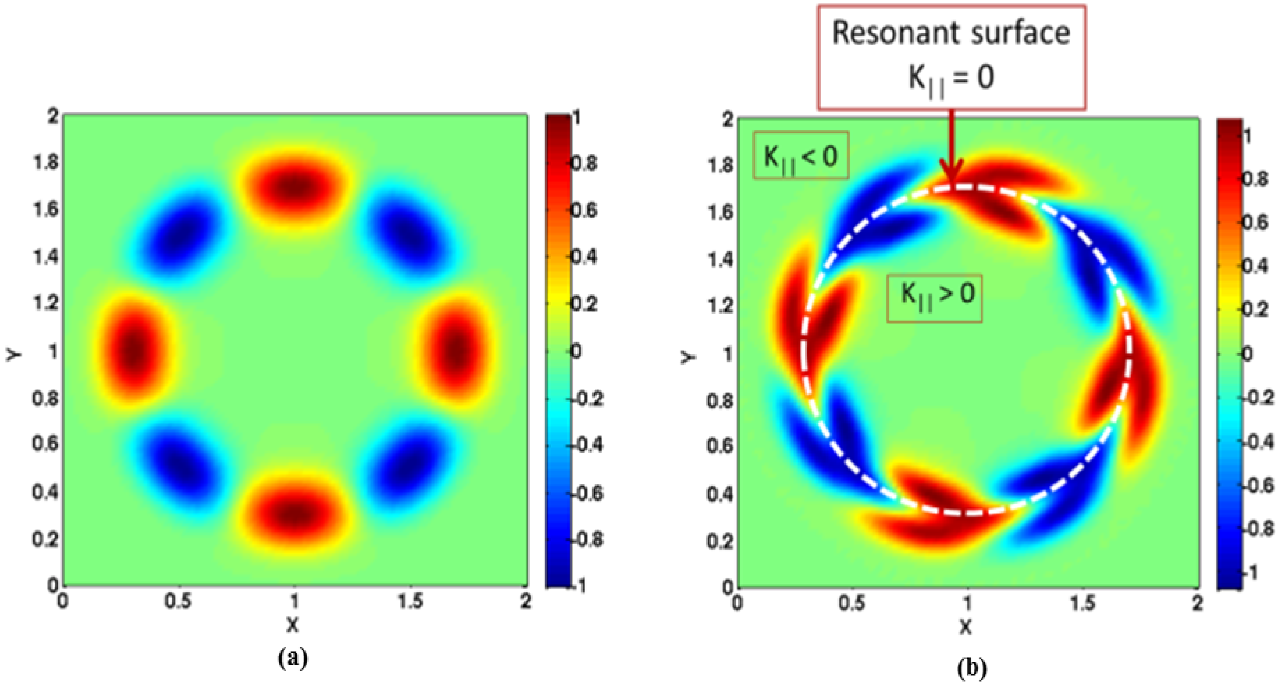

Figure 4.11

Chapter 5

Nonlinear Simulations of Turbulence

وَ كَم يَرفَعُ العِلمُ أَشخَاصًا إِلَى رُتَبٍ
وَ يُخفِضُ الجَهلَ أَشرَافًا بِلَا أَدَبِ

الإِمَام الشَّافِعي (١٥٠ هـ - ٧٦٧ م)

Contents

Acrylique, (F. Hariri, 2008)

As extensively discussed in Chapter 2, FENICIA code is based on a modular numerical scheme specially designed to address anisotropic transport of any set of equations which can be recast in the form of (1.19) presented in Chapter 1. The aim of this chapter is primarily to highlight the special advantages underlying the use of the Flux Coordinate Independent (FCI) field-aligned method for turbulence simulations. To this end, a 3-dimensional 4-field fluid system, which models the slab branch of the ITG instability, serves as a testbed for this study. In the first section, some of the linear properties of the drift-instability in magnetized plasmas are recalled. In the second section, convergence tests are performed in the nonlinear turbulent regime, showing fast convergence achieved at $nz = 15$. Thus, with the new method, one needs only a few tens of toroidal points to get a good result, regardless of the toroidal mode number, provided that adequate resolution is available in the poloidal plane. Finally, the last section addresses the implementation of an island slab geometry, with a special focus on the treatment of the X-point region. The ultimate result is showing that the FCI approach allows, in particular, not only a more natural treatment of the operations in the poloidal plane as discussed in Chapter 2, but it also deals without difficulty with X-point configurations and with O-points such as the magnetic axis, since it is constructed on coordinate systems with non-singular metric.

5.1 ITG model implemented in FENICIA

The most complete system of equations which has been implemented in the framework of this thesis is explicitly shown here:

$$\begin{cases} \partial_t \tilde{n} + [\phi, log(n_0)] - [\phi, \rho_*^2 \nabla_\perp^2 \phi] + C_\parallel \nabla_\parallel u_\parallel = D_n \nabla_\perp^2 \tilde{n} \\ \partial_t u_\parallel + [\phi, u] + C_\parallel (\frac{1}{\tau} \nabla_\parallel \tilde{n} + \nabla_\parallel \phi + \nabla_\parallel T_\parallel) = D_u \nabla_\perp^2 u_\parallel \\ \partial_t T_\perp + [\phi, T_\perp] - \chi_{\parallel\perp} \nabla_\parallel^2 T_\perp = D_{T_\perp} \nabla_\perp^2 T_\perp \\ \partial_t T_\parallel + [\phi, T_\parallel] + \frac{2}{\tau} C_\parallel \nabla_\parallel u_\parallel - \chi_{\parallel\parallel} \nabla_\parallel^2 T_\parallel = D_{T_\parallel} \nabla_\perp^2 T_\parallel \\ \tilde{n} = \phi \end{cases} \tag{5.1}$$

As we shall see in the next section 5.2, the system (5.1) captures faithfully well the slab branch of the Ion Temperature Gradient instability. The first equation stands for the continuity (or mass conservation) equation, the second one for the parallel momentum balance, and the last two for transverse and parallel heat transport equations, respectively.

Notice that, in the present version of the model, the variable $T_\perp$ appears only in one equation. It has the vocation to be a *passive scalar*, in the sense that it is sensitive to the turbulent field, namely ϕ, but it does not back-react on it. This quantity can be considered as a tracer of the turbulent field.

All quantities are dimensionless. $\tilde{n}$ is the relative perturbed ion guiding center density, n_0 is the equilibrium density profile, $u_\parallel$ is the ion parallel velocity normalized to the thermal speed v_{th}, $T_\perp$ and $T_\parallel$ the transverse and parallel ion temperatures normalized to the constant electron temperature T_e, and ϕ is the electrostatic potential normalized to T_e/e. Both transverse coordinates (x, y) involved in the Poisson bracket are normalized to the tokamak minor radius a. We define two dimensionless parameters: $C_\parallel = a/R \times 1/\rho_*$ where R is the tokamak major radius, $\rho_* = \rho_s/a$ is the reduced gyro-radius with $\rho_s = (mT_e)^{1/2}/eB$ being the ion sound Larmor radius. Moreover τ is the ratio of electron temperature to ion temperature T_e/T_i. Time is normalized to the Bohm timescale $a^2/(\rho_s c_s)$, where $c_s = (T_e/m)^{1/2}$ is the ion sound speed. The explicit expression of the parallel derivative operator $\nabla_\parallel$ depends on the magnetic field structure. In the case of a cylindrical geometry one can write

$$\nabla_\parallel = \partial_\varphi + 1/q(r)\,\partial_\theta$$

with (r, θ) the polar coordinates in the poloidal plane and $q(r)$ the safety factor.

Finally, D_n, D_u, $D_{T_\perp}$ and $D_{T_\parallel}$ are dissipative transverse transport coefficients which account for the weak collisional transport and ensure the damping of small scales. $\chi_{\parallel\perp}$ and $\chi_{\parallel\parallel}$ are the collisional parallel transport coefficients of transverse and parallel temperature, respectively. They can be approximated as follows:

$$\chi_\parallel \sim v_{th}^2/\nu_{coll} \approx 3.10^{10}\mathrm{m}^2 \cdot \mathrm{s}^{-1}$$

and

$$D_\perp \sim q^2 \rho_s^2 \nu_{coll} \approx 5.10^{-3}\mathrm{m}^2 \cdot \mathrm{s}^{-1}$$

for a Deuterium plasma at $T = 20\mathrm{keV}$, $n = 10^{20}\mathrm{m}^{-3}$, $B = 3\mathrm{T}$ and $q = 2$. Here, ν_{coll} is the ion collision frequency, and the high collisionality regime has been considered for $D_\perp$ (so-called Pfirsch-Schlütter regime). Typically, the ratio of the parallel to the transverse transport coefficient is $\chi_\parallel/D_\perp \approx 10^{12}$. This ratio is quite large, however. But it is essential for two reasons:

- Physically, this explains the strong anisotropy of transport in magnetized plasmas; the particles' parallel motion being almost free while the transverse one is constrained by the gyro-motion and by magnetic surfaces.
- It ensures that the ratio of parallel to transverse wave vectors remains small ($k_\parallel/k_\perp \sim \rho_i/R \ll 1$) which permits the use of efficient coordinate systems allowing one to simulate the smallest relevant volume of real space by taking advantage of the short perpendicular correlation lengths while still allowing for long parallel wavelengths and rapid parallel motions.

Note that one does not use these values of parallel transport and dissipation coefficients. Conversely, ad hoc values are used with a much smaller ratio $\chi_\parallel/D_\perp$ than the one expected in tokamaks (see section 5.3.1). In particular, $D_\perp$ is chosen so as to ensure the damping of the smallest scales that one can resolve at a given grid size.

The quasi-neutrality constraint is the relationship between guiding-center density fluctuations $\tilde{n}$ and the electric potential. It is given by: $\tilde{n} = \phi - \langle\phi\rangle - \rho_*^2\nabla_\perp^2\phi$. The first two terms on the right hand side come from the assumption that electrons have an adiabatic response, with $\langle\phi\rangle$ the flux surface averaged potential. The last term accounts for the ion polarization density in the long wavelength (with respect to the ion Larmor radius) limit. In the upcoming nonlinear simulations, it has been simply considered that $\tilde{n} = \phi$. The implementation of the complete quasi-neutrality equation into FENICIA should be investigated further. As a matter of fact, computing the flux-surface average and inverting the 2D Laplacian (to obtain ϕ out of $\tilde{n}$) would have required additional, although not critical, developments and time. Note that the polarization term can be safely ignored in the long wavelength limit, i.e. when $k_\perp\rho_s \ll 1$. Upon dropping the $\langle\phi\rangle$ term, one is left with a large inertia of zonal flows, which are then expected to remain at a fairly low level. Still, part of the polarization contribution has been taken into account in the continuity equation via the Poisson bracket $[\phi, \rho_*^2\nabla_\perp^2\phi]$. In particular, through the divergence of the (r,θ) component of the Reynolds stress tensor.

5.2 Linear ITG modes properties

Ultimately, one is interested in a reduced description of plasma turbulence to the extent that it is economical and accurate. The system (5.1) models the slab branch of the ITG instability. The driving terms of the linear instability are first the temperature gradient (departure from thermodynamical equilibrium) and the phase shift between the fluctuations of the advected fields and that of the electric potential. In the later case, the phase shift is provided by the finite motion of the ions along the field lines. This corresponds to the terms proportional to $C_\parallel$ in (5.1). It is instructive to state that the model derived by Akira Hasegawa and Masahiro Wakatani (H-W) in 1983 and presented in [Hasegawa 1983] consistently represents the simplest model for this type of instability. It was initially derived for plasma edge turbulence. What we mean here is that the instability present in the H-W model relies on the same mechanism as the one discussed in (5.1). More precisely, the instability's critical driving terms are (i) the existence of equilibrium gradients, density in H-W model or parallel temperature in the slab ITG model, *and* (ii) the existence of a phase shift between the electric potential fluctuations and the fluctuations of the transported quantity: density or temperature, respectively. In the H-W model, this phase shift results from the finite parallel resistivity (the so-called adiabaticity parameter), while it is due to parallel transport $\chi_\parallel$ in the present model.

5.2.1 Dispersion Relation

In the remainder of this section, we perform a simplified linear analysis. To do so, we decompose each field into its equilibrium and fluctuating parts, the former one being defined as the flux surface average of the given quantity, and is denoted by the "0" subscript. One then gets:

$$n = n_0 + \tilde{n}; \qquad u_\parallel = u_{\parallel 0} + \tilde{u}_\parallel; \qquad T_\parallel = T_{\parallel 0} + \tilde{T}_\parallel; \qquad T_\perp = T_{\perp 0} + \tilde{T}_\perp; \qquad \phi = \tilde{\phi}$$

We shall consider the following static equilibria: $u_{\parallel 0} = 0$, $T_{\perp 0} = cst$ and $T_{\parallel 0}(r) \neq 0$. Notice that this equilibrium is actually non-stationary. Indeed, in the absence of heat source for the parallel temperature, $T_{\parallel 0}(r)$ will evolve under the action of the transverse dissipation coefficient $D_{T_\parallel}$, until its gradient completely vanishes. Provided $D_{T_\parallel}$ is small enough, such a relaxation of the equilibrium profile can be considered as adiabatic with respect to the development of the instability (this requires $D_{T_\parallel}/L^2_{T_\parallel}$ to remain small with respect to the growth rate of the instability, with $L_{T_\parallel}$ the transverse gradient of $T_{\parallel 0}$).

We then investigate the limit in which small amplitude fluctuations with respect to equilibrium quantities are considered. All nonlinear terms can thus be dropped at leading order and one is led to the following linearized system:

$$\begin{cases} \partial_t \tilde{\phi} - \partial_r log(n_0) \frac{1}{r} \partial_\theta \tilde{\phi} + C_\parallel \nabla_\parallel \tilde{u}_\parallel = D_n \nabla^2_\perp \tilde{\phi} \\ \partial_t \tilde{u}_\parallel + C_\parallel \left(1 + \frac{1}{\tau}\right) \nabla_\parallel \tilde{\phi} + C_\parallel \nabla_\parallel \tilde{T}_\parallel = D_u \nabla^2_\perp \tilde{u}_\parallel \\ \partial_t \tilde{T}_\perp - \chi_{\parallel\perp} \nabla^2_\parallel \tilde{T}_\perp = D_{T_\perp} \nabla^2_\perp \tilde{T}_\perp \\ \partial_t \tilde{T}_\parallel - \partial_r T_{\parallel 0} \frac{1}{r} \partial_\theta \tilde{\phi} + \frac{2}{\tau} C_\parallel \nabla_\parallel \tilde{u}_\parallel - \chi_{\parallel\parallel} \nabla^2_\parallel \tilde{T}_\parallel = D_{T_\parallel} \nabla^2_\perp \tilde{T}_\parallel \end{cases} \tag{5.2}$$

The usual scale separation assumption is then used to proceed further. The characteristic perpendicular wavelengths of the fluctuations $k_\perp^{-1}$ are assumed to be much smaller than those of the equilibrium density and the parallel temperature, i.e: L_n and L_T: $k_\perp L_n \sim k_\perp L_T \gg 1$. In this framework, the Fourier transform can be applied to the fluctuating fields only, with the implicit assumption that results remain valid provided the above inequalities are fulfilled.

Following the standard Fourier transform approach, each 3D scalar field F can then be decomposed as follows: $F = \sum \hat{F}_k(r) \exp\{i(m\theta + n\varphi - \omega t)\}$. Eq. (5.2) consequently writes:

$$\begin{pmatrix} -i\omega - ik_\theta\partial_r \log(n_0) + D_n k_\perp^2 & iC_\parallel k_\parallel & 0 \\ iC_\parallel k_\parallel \left(1 + \frac{1}{\tau}\right) & -i\omega + D_u k_\perp^2 & iC_\parallel k_\parallel \\ -ik_\theta \partial_r T_{\parallel 0} & i\frac{2iC_\parallel k_\parallel}{\tau} & -i\omega + \chi_{\parallel\parallel} k_\parallel + D_{T_\parallel} k_\perp^2 \end{pmatrix} \begin{pmatrix} \hat{\phi}_k \\ \hat{u}_k \\ \hat{T}_{\parallel k} \end{pmatrix} = 0 \tag{5.3}$$

Here, $k_\theta = m/r$ and $k_\perp^2 = k_r^2 + k_\theta^2$, with $k_r^2 \equiv -\partial_r^2 \log(\hat{F}_k)$. Since the linearized system involves only the parallel temperature (but not $T_\perp$), some of the $\parallel$ subscripts can be safely dropped in the following calculations. $D_{T_\parallel}$ and $\chi_{\parallel\parallel}$ will be replaced by D_T and $\chi_\parallel$, respectively.

The expression of the dispersion relation may be found for nontrivial solutions such that the determinant of the system vanishes. It is given by

$$\begin{aligned} &\omega^3 + i\omega^2 \left\{(D_n + D_u + D_T)k_\perp^2 + \chi_\parallel k_\parallel^2 - i\omega_n^*\right\} \\ &-\omega \left\{(D_n D_u + D_u D_T + D_n D_T)k_\perp^4 + \chi_\parallel (D_n + D_u) k_\parallel^2 k_\perp^2 + C_\parallel^2 k_\parallel^2 \left(1 + \frac{3}{\tau}\right)\right. \\ &\left.-i\omega_n^* \left[\chi_\parallel k_\parallel^2 + (D_u + D_T)k_\perp^2\right]\right\} \\ &-i \left\{D_n D_u D_T k_\perp^6 + \chi_\parallel D_n D_u k_\perp^4 k_\parallel^2 + C_\parallel^2 k_\parallel^2 \left(\frac{2D_n + D_T}{\tau} + D_T\right) + \chi_\parallel C_\parallel^2 k_\parallel^4 \left(1 + \frac{1}{\tau}\right)\right\} \\ &-\omega_n^* \left\{D_u D_T k_\perp^4 + \left(\chi_\parallel D_u k_\perp^2 + \frac{2C_\parallel^2}{\tau}\right) k_\parallel^2\right\} + C_\parallel^2 k_\parallel^2 \omega_T^* = 0 \end{aligned} \tag{5.4}$$

with $\omega_n^* \equiv k_\theta \partial_r \log(n_0)$ and $\omega_T^* \equiv k_\theta \partial_r T_{\parallel 0}$ the diamagnetic frequencies. It is third order, consistently with the fact that only 3 fields were considered. Following the nomenclature proposed in the book of D. B. Melrose [Melrose 1989], this is a so-called *kinetic instability*, in the sense that the dispersion relation (5.4) contains both real and imaginary coefficients[1].

Note that dissipative coefficients (D_n, D_u and D_T) and the parallel diffusivity $\chi_\parallel$ are essential to dissipate the energy at small scales. Hence, preventing the unavoidable and intractable development of small scales, down to the grid resolution, in the nonlinear regime.

5.2.2 Threshold and growthrate

The linear properties of the above model described by (5.1) are best understood by first considering their parallel and perpendicular effects separately, and then looking at the combination which results from their interaction. Much intuition can be developed by evaluating Eq. (5.4) in two limits: the inviscid limit for which

---

[1] This is usually the case in kinetic theory, where the imaginary coefficients of the dispersion relation account for wave-particle resonant interactions, as first noticed by L. Landau.

$D_n = D_u = D_T = 0$ and the inviscid limit without parallel transport for which $\chi_\parallel = 0$. In the first case, Equation (5.4) appropriately reduces to:

$$\omega^3 + i\omega^2\left(\chi_\parallel k_\parallel^2 - i\omega_n^*\right) - \omega k_\parallel^2\left\{C_\parallel^2\left(1+\frac{3}{\tau}\right) - i\chi_\parallel\omega_n^*\right\}$$
$$-i\chi_\parallel C_\parallel^2 k_\parallel^4\left(1+\frac{1}{\tau}\right) + C_\parallel^2 k_\parallel^2\left(\omega_T^* - \frac{2}{\tau}\omega_n^*\right) = 0 \tag{5.5}$$

leading to two separate cases to be considered.

We start by studying the inviscid case without parallel transport, that is in the limit where $\chi_\parallel = 0$. One then finds:

$$\mathcal{D}(k,\omega) \equiv \omega^3 + \omega^2\omega_n^* - \omega C_\parallel^2 k_\parallel^2\left(1+\frac{3}{\tau}\right) + C_\parallel^2 k_\parallel^2\left(\omega_T^* - \frac{2}{\tau}\omega_n^*\right) = 0 \tag{5.6}$$

According to this expression, we are left with a *reactive instability*, for which all coefficients of the dispersion relation are real. Possible complex conjugate solutions of ω may then be found. In particular, this means that linearly damped $(\Im(\omega) < 0)$ and excited $(\Im(\omega) > 0)$ waves appear at the same time. At the linear threshold, above which the instability develops, all solutions are real, by definition. It can be obtained by looking for those real solutions of both the dispersion relation $\mathcal{D}(k,\omega_0) = 0$, and of $\partial_\omega\mathcal{D}(k,\omega)|_{\omega_0} = 0$, namely:

$$\partial_\omega\mathcal{D}(k,\omega) = 3\omega^2 + 2\omega\omega_n^* - C_\parallel^2 k_\parallel^2\left(1+\frac{3}{\tau}\right) = 0 \tag{5.7}$$

From the expression of the derivative $\mathcal{D}$, one can know the maxima and the minima of the function. And upon calculating the discriminant of Eq. (5.7) one knows how many solutions there exists. Typically, for a 3^{rd} order degree polynomial admitting 3 real solutions on gets the graph in Fig. 5.1 In the inviscid case without parallel transport, the linear threshold is obtained from the system made of Eq. (5.6) and of Eq. (5.7). As a result, the real frequency of the waves at the threshold writes:

$$\omega_{0\pm} = -\frac{\omega_n^*}{3} \pm \frac{1}{3}\left\{\omega_n^{*2} + 3C_\parallel^2 k_\parallel^2\left(1+\frac{3}{\tau}\right)\right\}^{1/2} \tag{5.8}$$

By plugging these $\omega_{0\pm}$ solutions in Eq. (5.6), one obtains the implicit relationship between temperature and density gradients at the threshold. Thus, two fundamental limits are distinguished:

- In the limit where $\omega_n^* = 0$: $\omega_{T,crit}^* = \pm 2C_\parallel k_\parallel\left(\frac{1}{3}+\frac{1}{\tau}\right)^{3/2}$
- In the limit where $\omega_n^* \to \pm\infty$, two branches are to be distinguished: either $\omega_{T,crit}^* = \frac{2}{\tau}\omega_n^*$ or $\omega_{T,crit}^* = -\frac{4}{27}\,\omega_n^{*3}\left(C_\parallel k_\parallel\right)^{-2}$

Rather than delve into much unpleasant algebra here, we will instead rely upon Fig. 5.2 to show a few important features of the local limit. It is clear that the

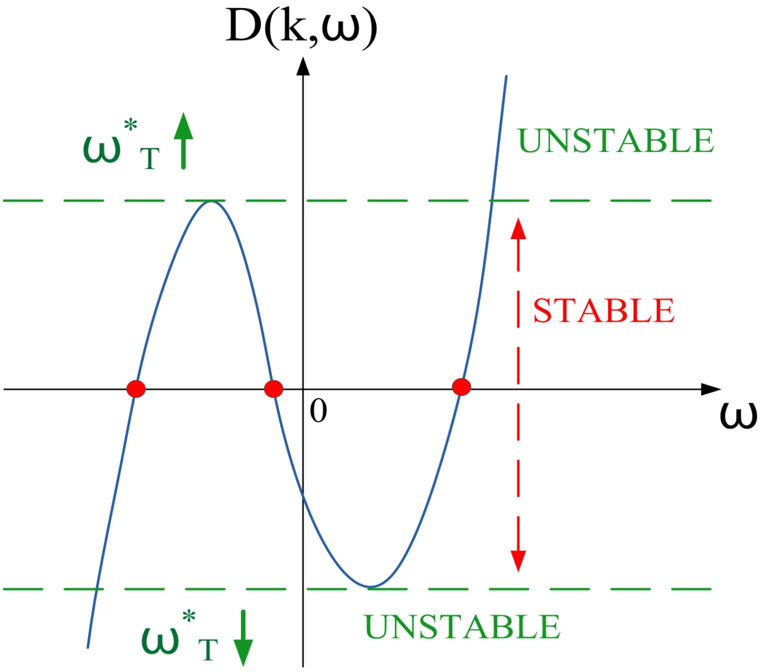

Figure 5.1: Graph of a 3^{rd} order polynomial having 3 real solutions where the regime is stable. Above or below the critical gradient, that is the threshold, there exists at least one unstable mode

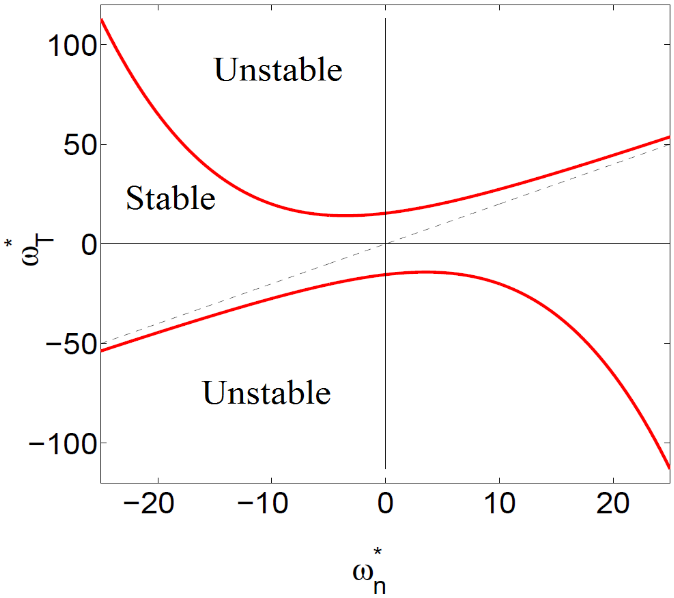

Figure 5.2: Critical temperature gradient as a function of the density gradient in the inviscid ITG case without parallel transport, Eq. (5.6) ($k_{\|}$ is taken equal to 0.4).

density gradient is stabilizing. That is, at constant temperature gradient, the system becomes stable when the density gradient increases.

Let us then study the inviscid case with vanishing density gradient, namely in the limit where $\partial_r \log(n_0) = 0$. Accordingly, one obtains:

$$\begin{aligned}\mathcal{D}(k,\omega) \equiv \omega^3 + i\omega^2\chi_\parallel k_\parallel^2 - \omega C_\parallel^2 k_\parallel^2\left(1+\frac{3}{\tau}\right)\\ -i\chi_\parallel C_\parallel^2 k_\parallel^4\left(1+\frac{1}{\tau}\right) + C_\parallel^2 k_\parallel^2 \omega_T^* = 0 \qquad (5.9)\end{aligned}$$

In this case, the linear threshold is obtained by looking for real solutions which separately cancel the real and imaginary parts of the dispersion relation given by Eq. (5.9). The real frequency of the waves at the threshold is simply expressed as:

$$\omega_{0\pm} = \pm\sqrt{1+\frac{1}{\tau}}\, C_\parallel k_\parallel \qquad (5.10)$$

Then, the critical temperature gradient for the inviscid ITG case at vanishing density gradient reads, for each of these waves[2]:

$$\omega_{T,crit}^* = \pm\frac{2C_\parallel k_\parallel}{\tau}\sqrt{1+\frac{1}{\tau}} \qquad (5.11)$$

It readily appears that small scales in the parallel direction are stabilized by parallel transport, as expected. Indeed, the linear instability threshold $\omega_{T,crit}^*$ tends to infinity in the limit $k_\parallel \to \infty$.

At this point, the algebra for solving the complete dispersion relation Eq. (5.4) becomes tedious. It is thus solved numerically to look for unstable solutions. This has been done[3] for a set of parameters characterizing the nonlinear simulations that will be discussed later in Sec. 5.3.

The equilibrium parallel temperature profile is such that $\partial_r T_{\parallel 0} = \nabla T_M\, r^2(1-r)[(1-2r_M)r - (2-3r_M)r_M]/[r_M^2(1-r_M)^2]$, with $r_M = 0.5$ and $\nabla T_M = -2$ if $r \leq r_c$, and $T_{\parallel 0} = 0$ otherwise. Here, $r_c = 1$ refers to the outer radial boundary of the confined plasma. A vanishing value of the logarithmic density gradient is considered, which maximizes the growth rate. For simplicity, $k_\perp$ is replaced by the poloidal wave number $k_\theta = m/r$ (with m the poloidal wavenumber), therefore assuming that the radial gradient length of the fluctuations is much bigger than the poloidal one. Finally, the normalized parallel wave vector is either considered as a free parameter, or set to be equal to $k_\parallel = \frac{m}{q(r)} - n$, with n the toroidal wavenumber and $q = 1 + 2(r/r_c)^2$ the safety factor. The other parameters are $D_n = D_u = D_T = 2.10^{-3}$, $\chi_\parallel = 12.5$, $C_\parallel = 12.5$ and $\tau = 1$.

---

[2] It can be shown that the other solutions of the dispersion relation are stable at the threshold: they have a negative imaginary part.
They read: $\omega'_\pm = -\omega_0/2 - i\chi_\parallel k_\parallel^2/2\left\{1 \mp \left[1 - (C_\parallel/\chi_\parallel k_\parallel)^2(1+9/\tau) + 2i\omega_0/(\chi_\parallel k_\parallel^2)\right]^{1/2}\right\}$.
Small modes with $k_\parallel \to 0$ have the largest imaginary part, which is still negative:
$\lim_{k_\parallel \to 0} \omega'_\pm = -\chi_\parallel k_\parallel^2/2\left\{1 - [(1+\tau)/(9+\tau)]^{1/2}\right\} < 0$.

[3] A simple routine, written in Matlab, has been developed for this purpose.

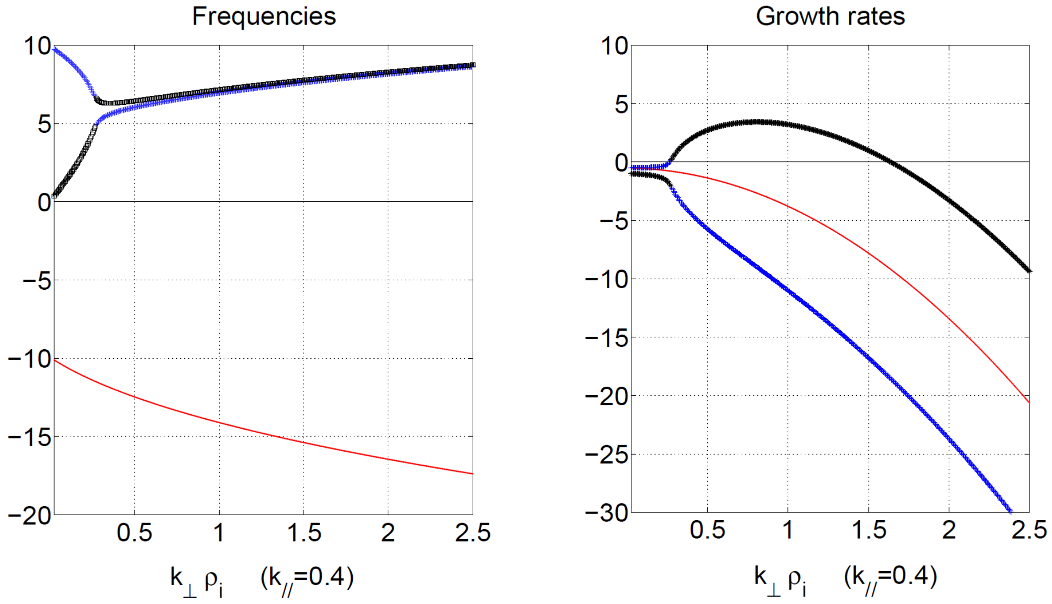

Figure 5.3: Real and imaginary parts of the 3 solutions of Eq. (5.4) as a function of $k_\perp = k_\theta$ for the set of parameters detailed in the text (at $r = 0.5$) and for $k_\parallel = 0.4$.

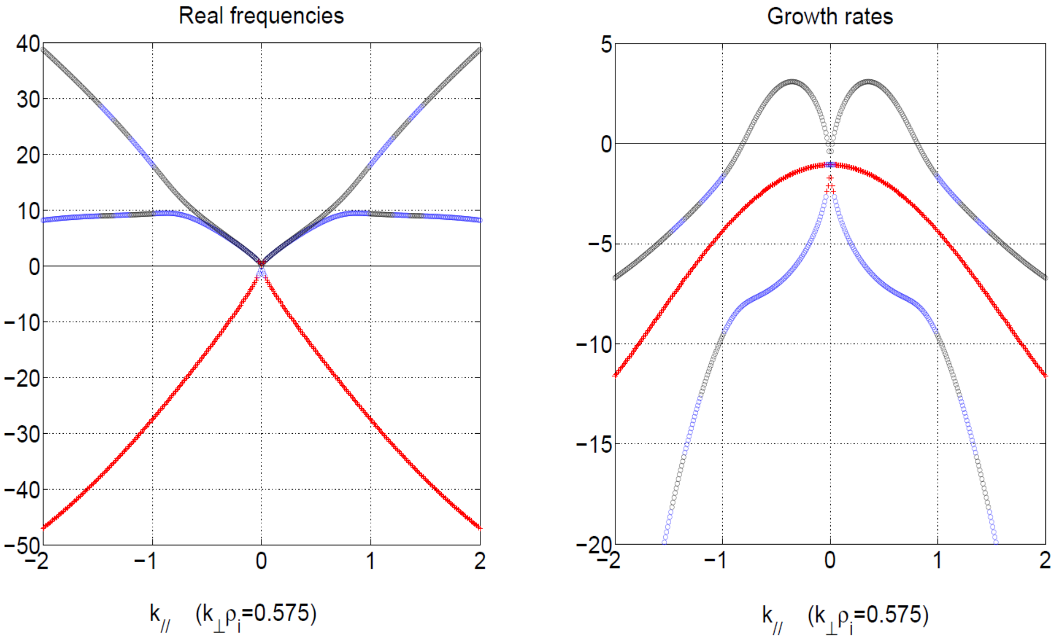

Figure 5.4: Real and imaginary parts of the 3 solutions of Eq. (5.4) as a function of $k_\parallel$ for the set of parameters detailed in the text (at $r = 0.5$) and for $k_\perp = 23$.

Figure 5.3 (resp. Fig. 5.4) shows the real and imaginary parts of the three solutions of Eq. (5.4) as a function of $k_\perp$ (resp. $k_\parallel$) at fixed $k_\parallel = 0.4$ (resp. $k_\perp = 20$). Notice that, as expected, there is at most one single unstable branch. All branches are stable at both small and large $k_\perp$ values. The damping at small scales is governed by the diffusion coefficients, $D_\perp$ and $\chi_\parallel$. For these parameters, unstable

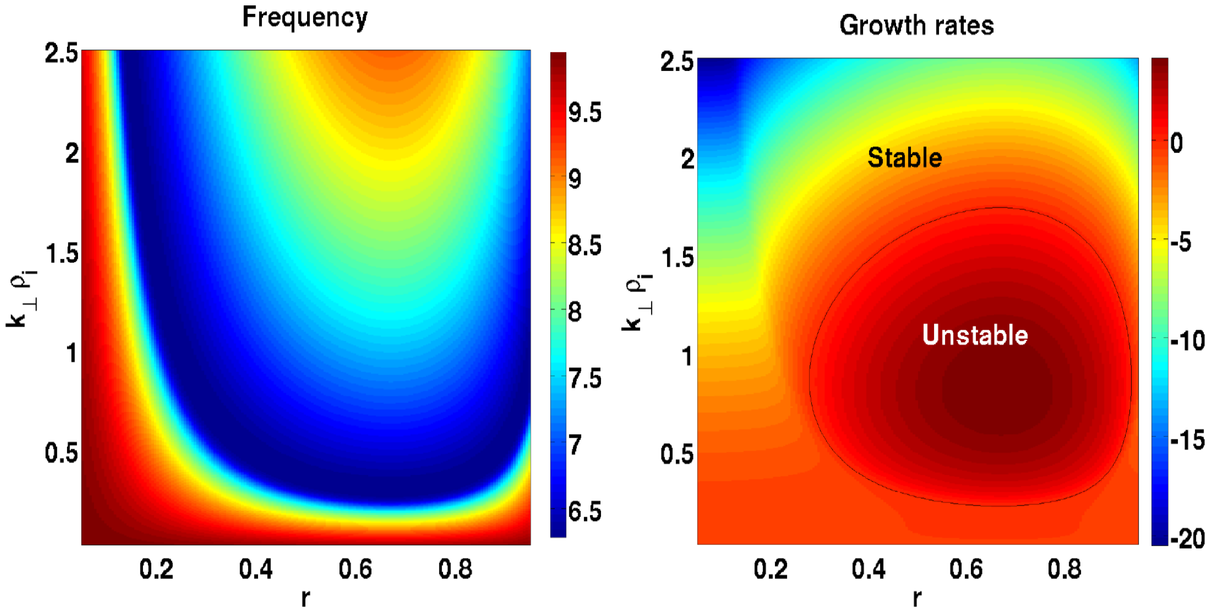

Figure 5.5: Real (left) and imaginary (right) parts of the most unstable solution of Eq. (5.4) for a mode with $(m, n) = (9, 6)$.

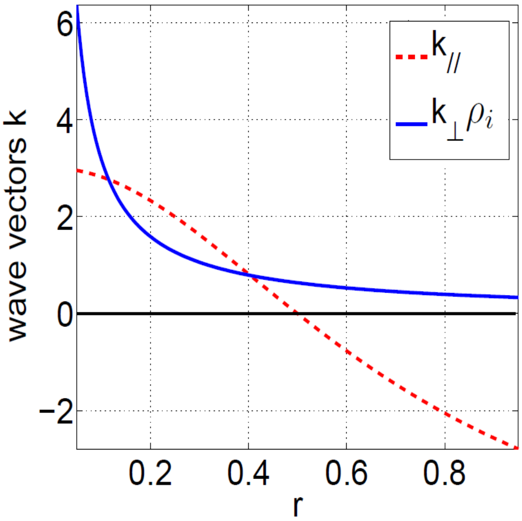

Figure 5.6: Profiles of $k_\perp$ and $k_\|$ for the mode having $(m, n) = (9, 6)$.

modes are characterized by $0.3 \lesssim k_\perp \rho_i \lesssim 1.6$ and $0 \lesssim k_\| \lesssim 0.6$ at mid radius values.

Alternatively, by considering a single mode (m, n), one can look at the radial locations at which it becomes unstable. This is examined more closely in Fig. 5.5. It is apparent as a result of the parabolic q profile, that most of the changes come from the variations of the $k_\|$ wave vector relative to the chosen mode as a function of radius. The range of the variation of $k_\|$ is also plotted in Fig. 5.6. Beyond these cursory investigations, it is of great interest to understand and discuss in the coming section the processes which set the nonlinear dynamics.

5.3 Nonlinear Simulations of Turbulence

5.3.1 Basic properties of slab-ITG turbulence with FENICIA

In general, fully developed ITG turbulence is difficult to describe analytically. In the absence of analytic insights, it is difficult to know how well the numerical code is performing, especially when the number of lines of code is large. Nonlinear turbulence is herein studied numerically by solving model (5.1). It is convenient to first start with a preliminary discussion on the properties of the turbulent regime embedded in the model described by (5.1).

The main parameters used for the nonlinear simulations presented in this chapter are chosen as follows: the code is run 6000 times with a time step equals to $dt = 10^{-3}$. We recall here that time is normalized to the Bohm time scale $a^2/(\rho_s c_s)$, and lengths to the minor radius a. The differential operators are evaluated on a grid of size $(nx, ny, nz) = (200, 200, 20)$ (a parameter scan is performed over different values of nz in the convergence test discussed in section 5.3.2), with $\rho_* = 0.08$. It follows that the transverse grid increment is equal to $\rho_s/16$. The transverse dissipative coefficients and the parallel transport coefficient are set to $D_\perp = 10^{-3}$ and $\chi_\parallel = 12.5$. Periodic boundary conditions are used in the z direction and the vector of states is set to zero outside the plasma radius. We consider a density profile expressed as $log(n_0) = -(r^2 - a^2)/2L_n$ and a q profile defined by $q = 1 + 2r^2$. The perturbed density is initialized by

$$\tilde{n}(t = 0, r) = \sum g_0(r) \times \cos(m\theta - n\varphi)$$

where

$$g_0(r) = \exp\left[-\frac{(r - r_s)^2}{r_s^2} m^2\right] \times \left(\frac{r}{r_s}\right)^m \times \left(\frac{r - a}{r_s - a}\right)^2 .$$

and the sum involves only two modes $(m, n) = (9, 6)$ and $(m, n) = (10, 7)$. The radial envelope of the initial modes retains a Gaussian centered on their rational surface r_s (where $q(r_s) = m/n$, so that $k_\parallel(r_s) = 0$), and is chosen sufficiently narrow so as to minimize their parallel wave vector.[4] The poloidal cross section of the perturbed initial density field is plotted in Fig. 5.9 (top-left graph). As far as the initial equilibrium profiles are concerned, parallel velocity is such that $u_\parallel(t = 0, r) = 0$ and both the parallel and perpendicular temperatures are chosen to be equal at $t = 0$. The initial profile for both of the temperatures is plotted in Fig. 5.7a (dashed line).

---

[4] Indeed, a Taylor expansion of the parallel wave vector around the resonance position r_s leads to: $k_\parallel(r) \simeq (r - r_s)\, dk_\parallel/dr|_{r_s} = -(r - r_s)k_\theta/L_s$, with the poloidal wave vector equals to $k_\theta = m/r_s$ and the magnetic shear length defined by $L_s = qR/s$.

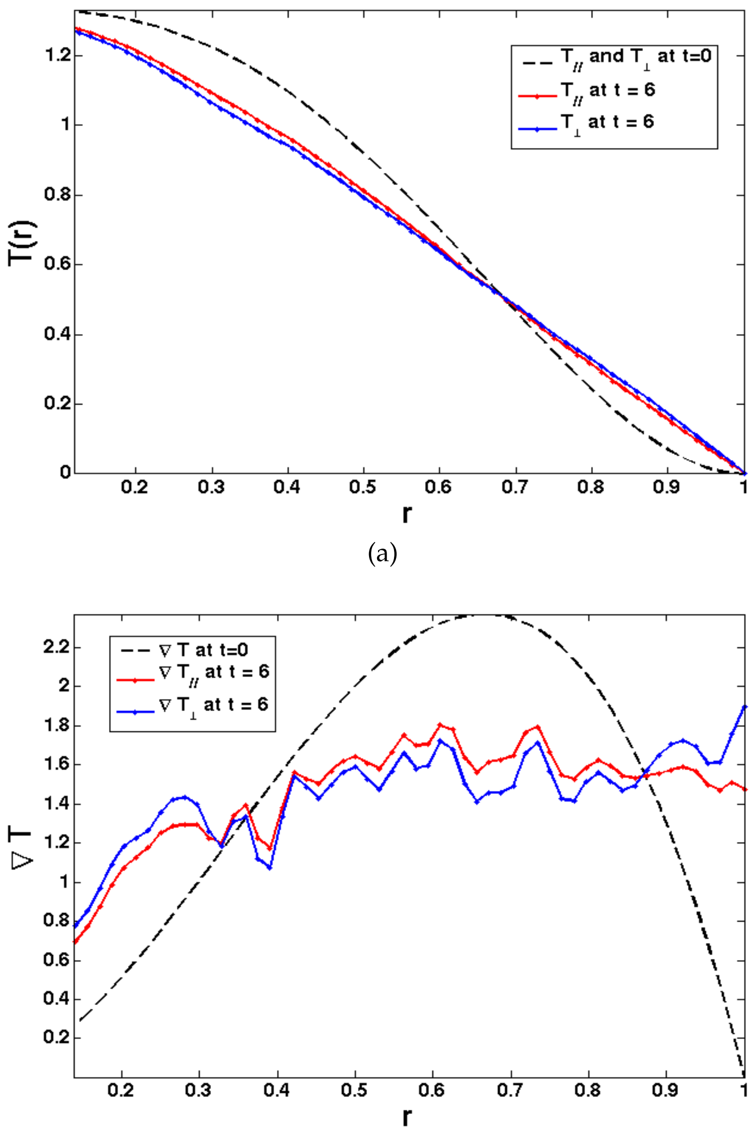

(a)

(b)

Figure 5.7: Parallel and perpendicular temperature profiles at $t = 0$ and at the $t = 6$, the time at the end of the simulation

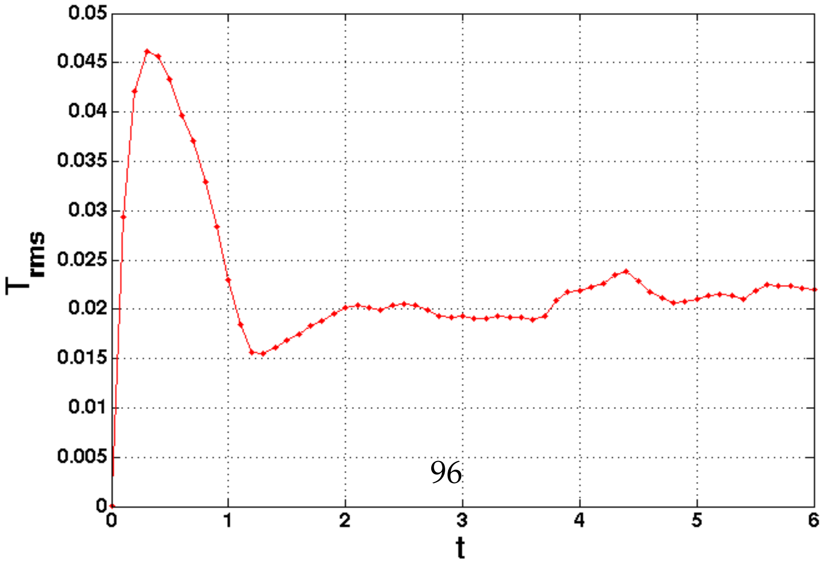

Figure 5.8: Plot of T_{rms} as a function of time

Recall that the code is global, i.e. that there is no scale separation between equilibrium and fluctuating quantities, including temperatures. Since no heat source is added to sustain the profiles so far, one expects the initial temperature profiles to relax under the action of heat turbulent transport. The result is actually clearly visible in Fig. 5.7a and Fig. 5.7b, where the final temperature profiles and temperature gradients are plotted. The gradient at the initial stage exceeds its critical value at the position were the perturbations were initiated (at roughly a mid-radius position on the simulation domain). Fluctuations then become unstable, and grow exponentially during the linear phase and eventually saturate as evidenced in the time evolution of the root mean square of the temperature fluctuations Fig. 5.8. The magnitude of the fluctuations exhibits an overshoot to reach a peak value at $t \sim 0.3$, which results from the dynamical balance between the linear excitation and nonlinear saturation mechanisms. The latter refer to dissipation via mode-mode coupling, which involves energy cascade towards linearly stable modes, and profile relaxation leading to the reduction of the linear growth rate. Considering the fairly large ρ_* value of the reported simulation, the energy confinement time is quite small, so that the time scale for profile relaxation – which is of the order of the energy confinement time for the entire profile – competes with that of nonlinear energy transfer. On one hand, assuming a Bohm-like scaling for τ_E leads to $\omega_c \tau_E \sim \rho_*^{-2}$ and on the other hand, nonlinear energy transfer typically occurs on an eddy turn-over time $\omega_c \tau_{eddy} \sim (k_\theta v_E)^{-1} \sim [(k_r \rho_s)(k_\theta \rho_s)(e\phi/T)]^{-1}$. Using a mixing length type of argument, then $e\phi/T \sim \rho_*$, and $k_r \rho_s \sim k_\theta \rho_s < 1$. It readily appears that, in this type of regime, both times are of the same order of magnitude: $\tau_E \sim \tau_{eddy}$. Therefore, both nonlinear mechanisms are likely to be effective in this case, and efficiently contribute to the nonlinear saturation of turbulence.

A good amount of information is shown hereafter in figures 5.9,5.10 and 5.11 of nonlinear simulations carried out using FENICIA with the previously chosen parameters. From the time sequence of the 2D snapshots of both fluctuating density and velocity fields, respectively in figures 5.9 and 5.10, turbulence progressively covers the whole radial domain of the cylinder but the center where temperature gradient vanishes for symmetry reason. The entire domain has become fully turbulent before the end of the simulation. The full temperature field, including both equilibrium and fluctuations, is plotted in Fig. 5.11. It is dominated by the equilibrium part, i.e. the flux-surface average component, the fluctuations being of the order of a few percents only in the saturated regime. 3D snapshots of density fluctuations allow one to highlight the fact that turbulent eddies are elongated along the magnetic field lines, Fig. 5.12. When propagating outwards, they encounter regions with larger safety factor values, hence looking more aligned to the z direction. The presence of corrugations in the parallel direction, characterized by finite $k_\parallel$ values, will be discussed in section 5.3.2.

By looking at Fig. 5.13a where we plot the T_{rms} values as a function of radius over time, we observe a quasi-ballistic propagation of the fluctuations towards

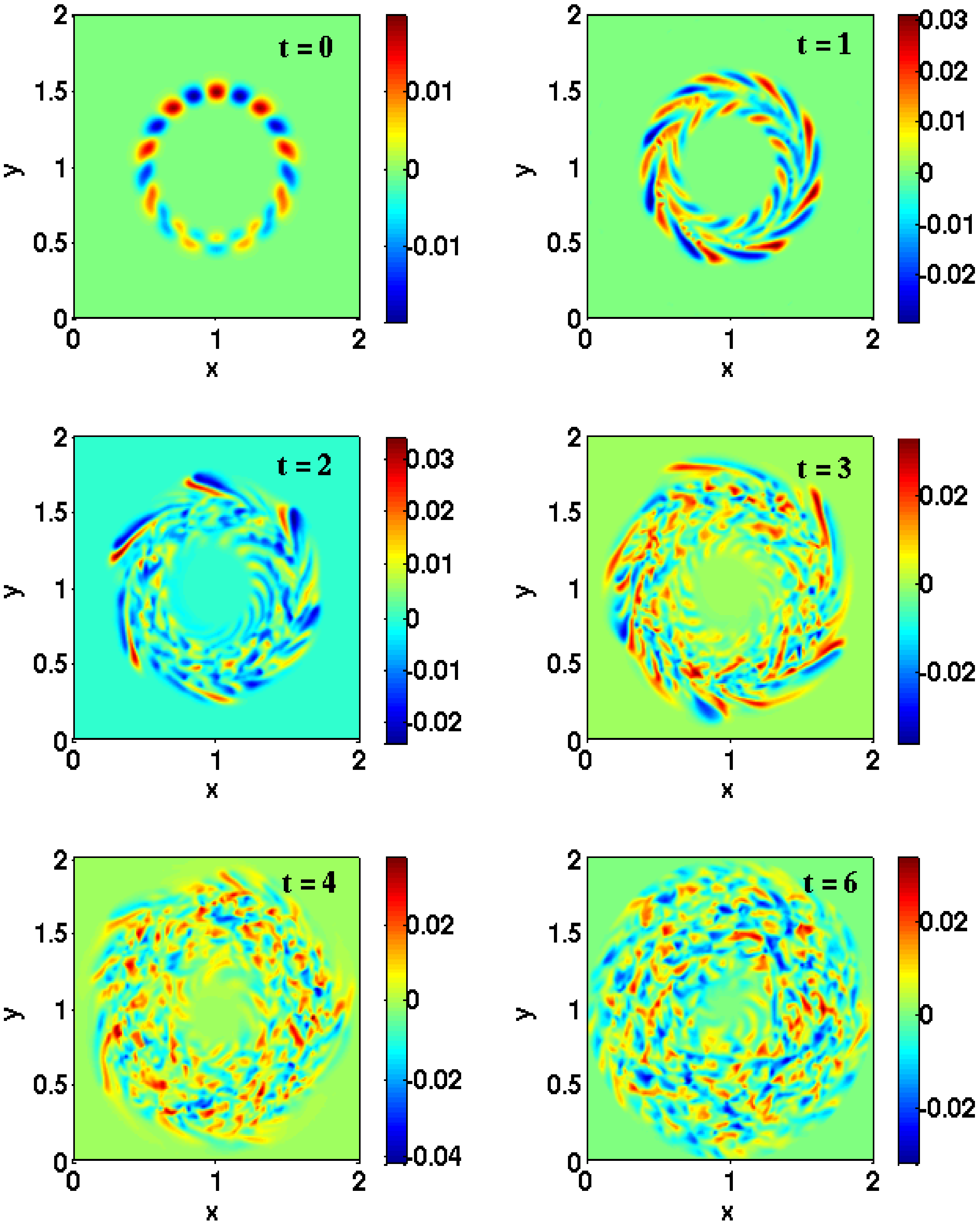

Figure 5.9: Snapshots of density fluctuations at different simulation times

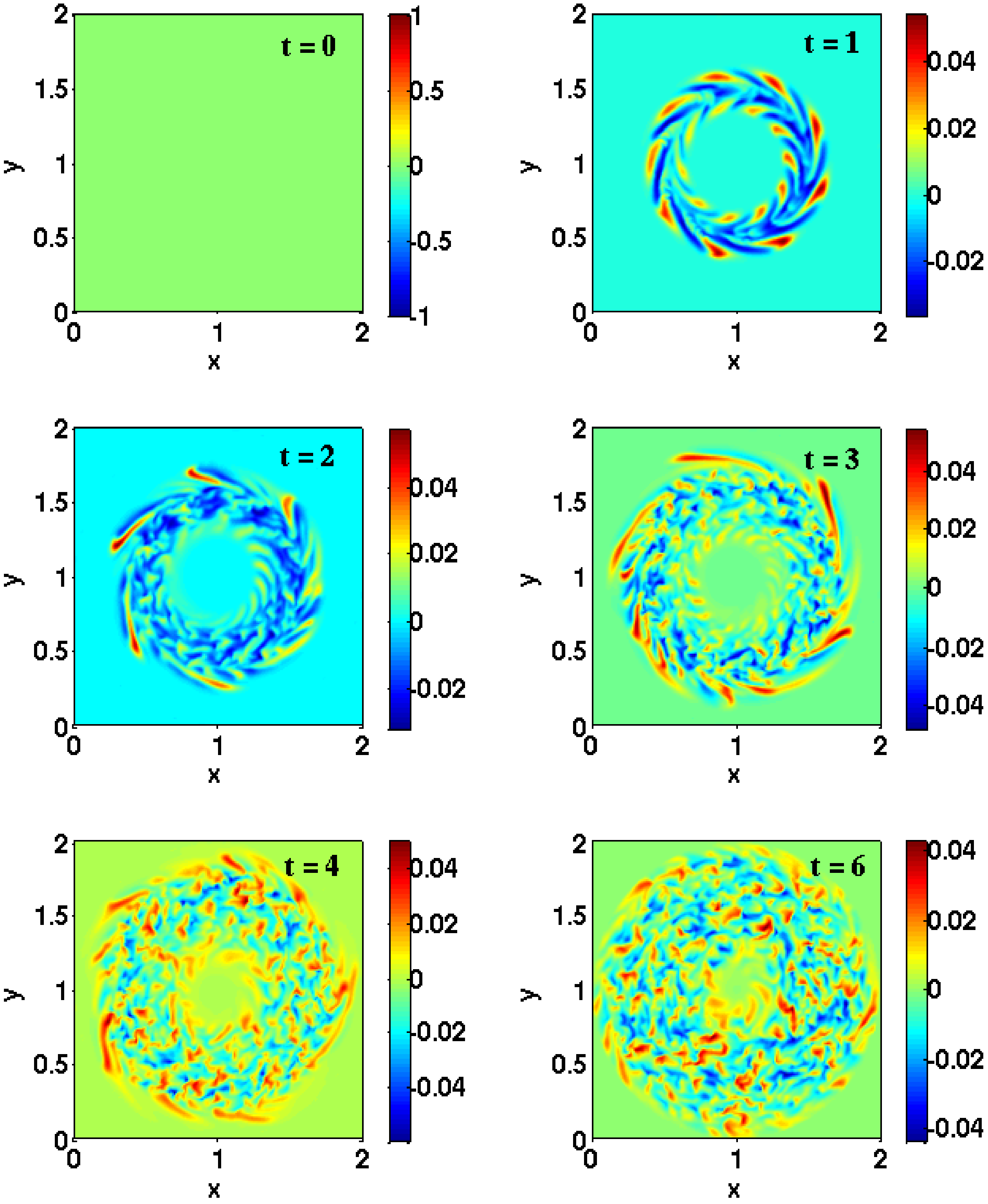

Figure 5.10: Snapshots of velocity fluctuations at different simulation times

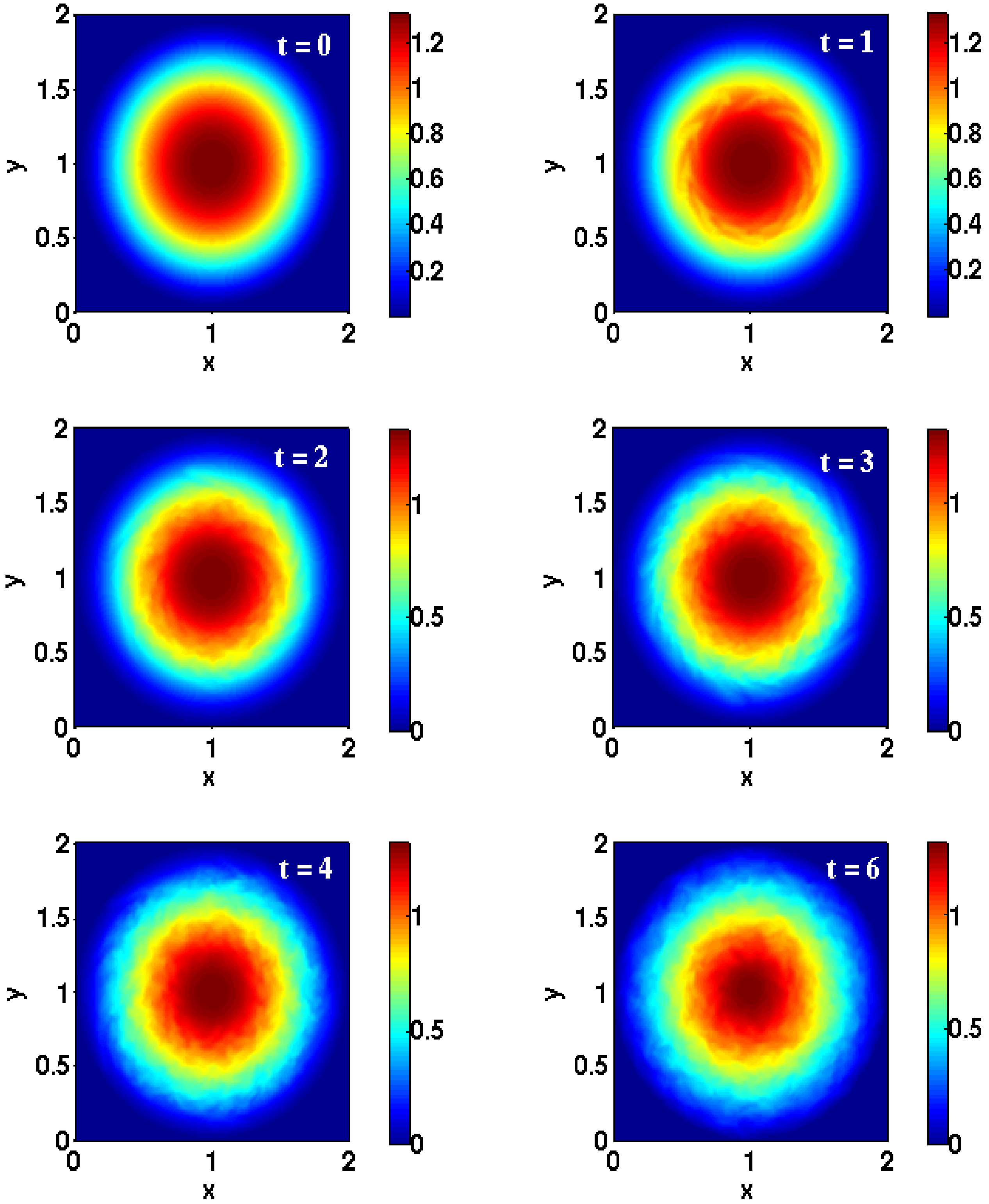

Figure 5.11: Snapshots of parallel temperature fluctuations at different simulation times

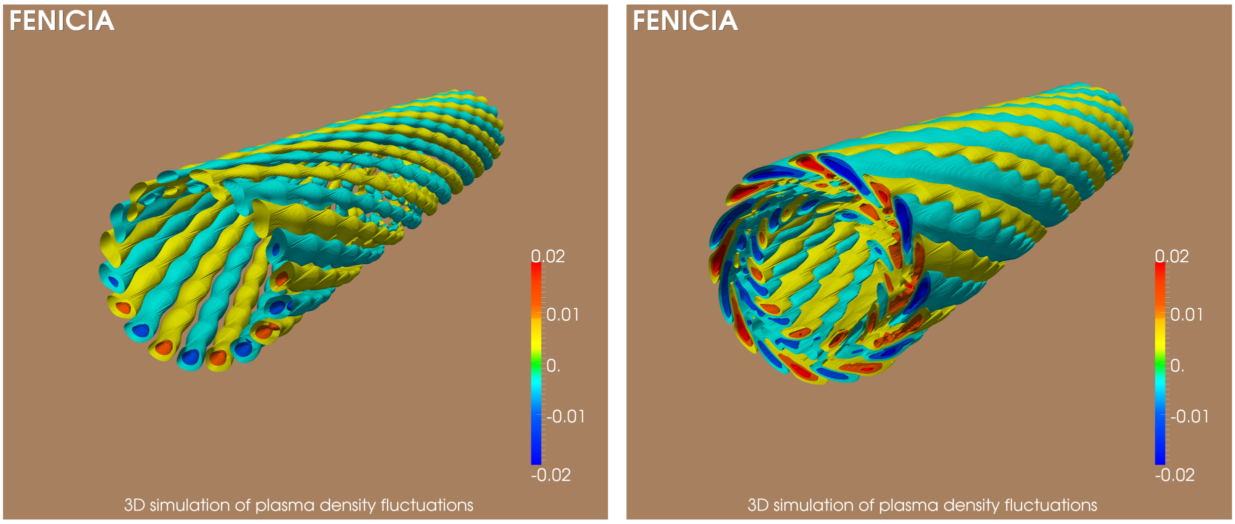

(a) t=0 (b) t=0.9

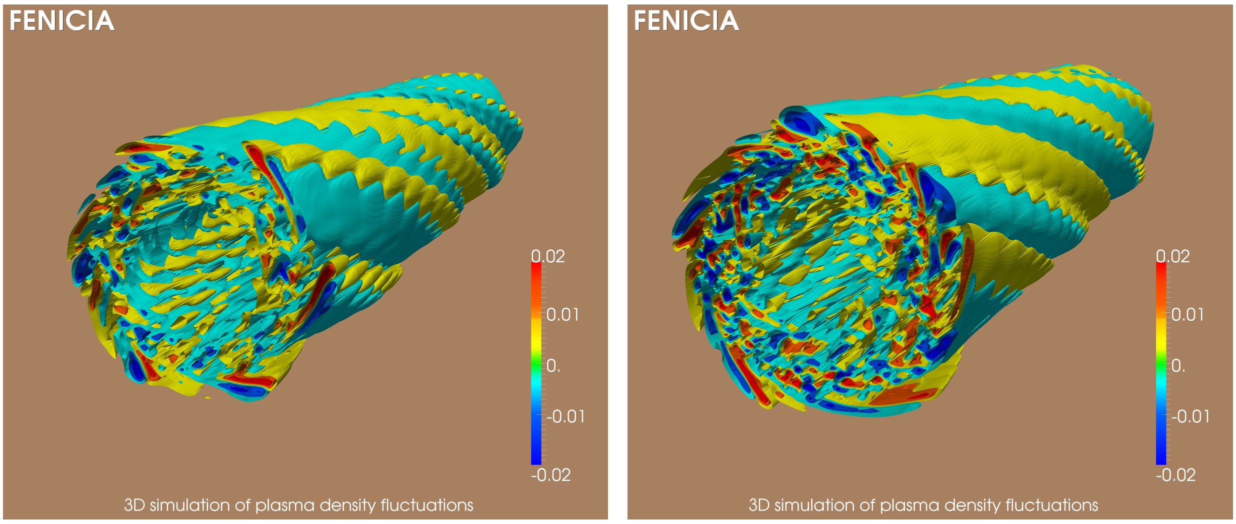

(c) t=2 (d) t=3

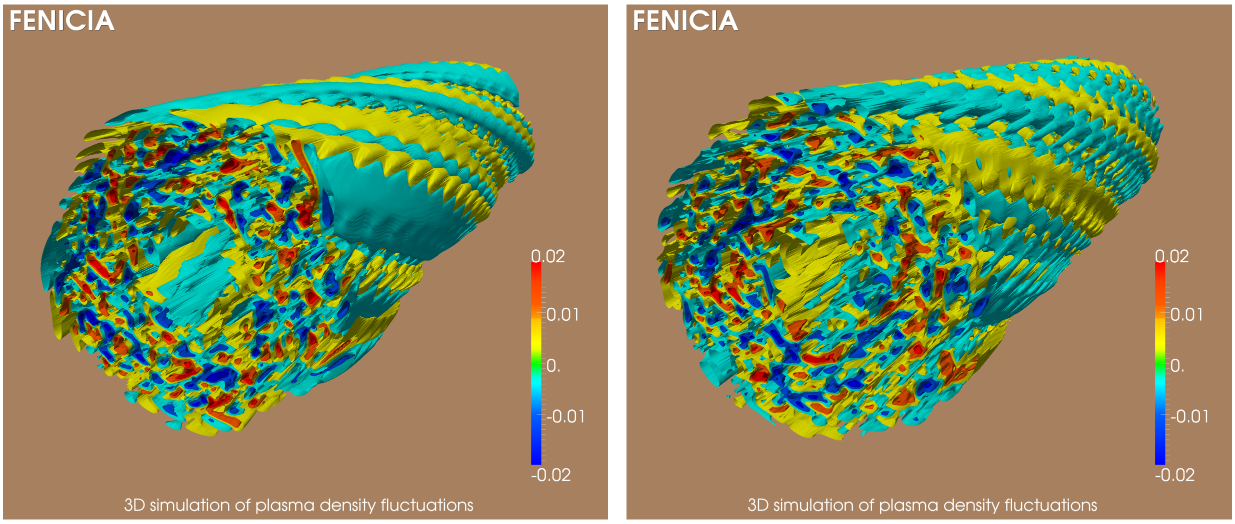

(e) t=4 (f) t=6

Figure 5.12: 3D snapshots of density fluctuations at different simulation times

the core and the edges of the domain until saturation is reached at the end of the simulation. Such a phenomenon is sometimes reported as turbulence spreading. It is also reminiscent of avalanche-like transport. The front velocity propagation is of the same order as the diamagnetic velocity, $v_* \sim (k_\theta \rho_s) c_s / L_T$, with L_T being the temperature gradient length. One may note that the motion is slightly faster when moving left towards the core than when moving right towards the edge. This is due to the small values of temperature at the edge. Front propagation of the fluctuations is accompanied by fronts of equilibrium temperature gradient as well, as illustrated in Fig. 5.13b. Interestingly, the gradient also steepens when moving outward: it is maximal at $r \approx 0.65$.

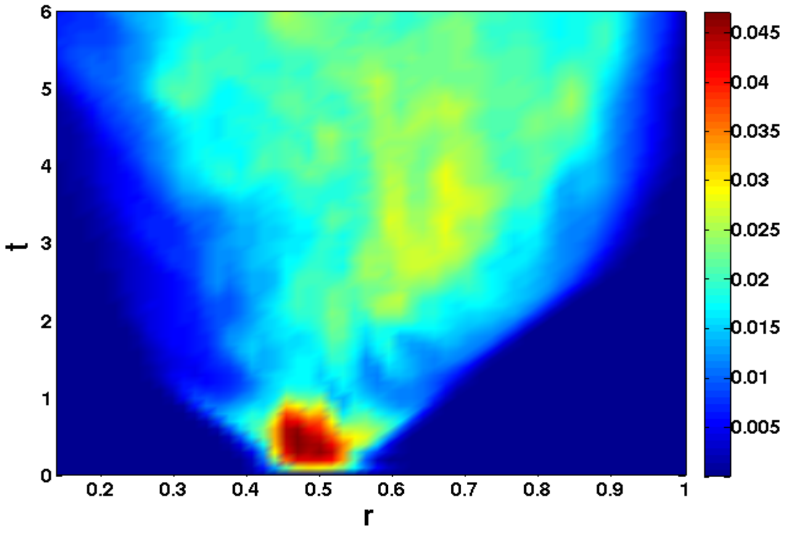

(a)

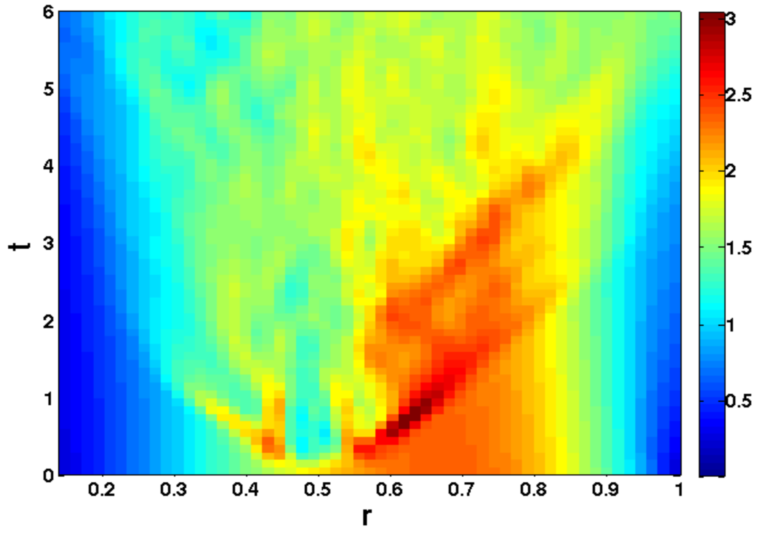

(b)

Figure 5.13: 2D plots of the root mean square of temperature fluctuations T_{rms} in (a) and the equilibrium temperature gradient ∇T_{eq} in (b) as a function of the radius r and the time t.

5.3.2 The strength of field-aligned coordinates

Here I study the convergence properties of the ITG model presented in Sec. 5.1 with respect to the spatial resolution. A test of spatial convergence on a $3D$ ITG nonlinear model showing the electric potential fluctuations level over time for different number of grid points in the **z** direction.

Consider a 3D field ϕ in the torus. It can be expressed as a sum of Fourier components along the periodic directions, θ and φ the respective poloidal and toroidal angles, as follows:

$$\phi(r,\theta,\varphi) = \sum_{m,n} \hat{\phi}_{m,n}(r,t)\mathrm{e}^{i(m\theta+n\varphi)} \tag{5.12}$$

When applied to this field, the parallel gradient given by $\nabla_\parallel = \partial_\varphi + q(r)^{-1}\partial_\theta$ in the large aspect ratio limit leads to the following expression:

$$\nabla_\parallel \phi(r,\theta,\varphi) = \sum_{m,n} i(n+m/q)\hat{\phi}_{m,n}(r,t)\mathrm{e}^{i(m\theta+n\varphi)} \tag{5.13}$$

Thus, the parallel wave vector is simply expressed as $k_\parallel(r) = n + m/q(r)$ and is dependent on the magnetic surface via the safety factor profile $q(r)$. It is apparent that if the field is characterized by almost vanishing parallel gradients $k_\parallel \sim 0$, and small scales are to be resolved in a chosen direction (for instance the poloidal direction), then even smaller scales should be captured in the toroidal direction, i.e: a factor q^{-1} times smaller. Indeed, if $\pm m_{max}$ stands for the highest poloidal wave number of interest for the problem to be addressed, then the highest toroidal wave number should be $n_{max} = \mp m_{max}/q(r)$ in order to ensure that elongated structures in the parallel direction are well described at this scale, namely $k_\parallel(r) = n_{max} + m_{max}/q(r) = 0$. In tokamak turbulence, m_{max} is basically constrained by micro-turbulence, which develops at Larmor scales such that $k_\theta \rho_i \sim 0.3$. The typical maximal m number of interest for standard situations [5] is such that $k_{\theta,max}\rho_i \sim 2$, so that $m_{max} \sim (r/a)\ \rho_*^{-1}$, which leads to $m_{max} \approx 500$ and $n_{max} \approx 250$ in ITER-like plasmas at mid-radius values.

Alternatively, one may compute parallel derivatives using field-aligned coordinates by employing a coarser grid in a chosen direction, while still properly describing the relevant $k_\parallel \sim 0$ modes. Although the method proposed in section 2.2 and implemented in FENICIA is more general than the one discussed in section 2.1.3, the reasoning is easier when focusing on the latter one. The parallel gradient can be computed by finite differences along the parallel direction s, which reads at second order:

$$\nabla_\parallel^{FCI} \phi(\rho,\xi,s) \approx \frac{\phi(\rho,\xi,s+\Delta s) - \phi(\rho,\xi,s-\Delta s)}{2\Delta s} \tag{5.14}$$

---

[5] This may not be the case in regimes with ion transport barriers, where turbulence at electron gyro-radius scales $k_\theta \rho_e \sim 0.1$ can become dominant.

where the superscript FCI stands for field-aligned coordinates, and $\Delta s = \Delta\varphi$ is the increment in the parallel direction. In terms of Fourier modes, an expression as such leads to the following:

$$\begin{aligned}
\nabla_{\parallel}^{FCI}\phi(\rho,\xi,s) &= \frac{1}{2\Delta s}\sum_{m,n}\hat{\phi}_{m,n}(r,t) \\
&\quad \left\{ \mathrm{e}^{i[m(\theta-\Delta\varphi/q)+n(\varphi+\Delta\varphi)]} - \mathrm{e}^{i[m(\theta+\Delta\varphi/q)+n(\varphi-\Delta\varphi)]} \right\} \\
&= \sum_{m,n}\hat{\phi}_{m,n}(r,t)\mathrm{e}^{i(m\theta+n\varphi)}\frac{\mathrm{e}^{i\Delta\varphi(n-m/q)]} - \mathrm{e}^{-i\Delta\varphi(n-m/q)]}}{2\Delta s} \\
&= \sum_{m,n}\hat{\phi}_{m,n}(r,t)\mathrm{e}^{i(m\theta+n\varphi)}\frac{i\sin[(n-m/q)\Delta\varphi]}{\Delta\varphi} \qquad (5.15)
\end{aligned}$$

It turns out that the effective parallel wave vector then reads $k_{\parallel}^{FCI} = \sin[(n - m/q)\Delta\varphi]/\Delta\varphi$. In this framework, all modes characterized by $n = m/q + \ell\pi/\Delta\varphi$ (with $\ell \in \mathbb{N}$) are resonant, in the sense that their effective parallel wave number is vanishing $k_{\parallel}^{FCI} = 0$. In this case, even large m modes can be coupled to "resonant" (i.e. such that $k_{\parallel}^{FCI} = 0$) low n modes. As a matter of fact, given a maximum poloidal wave number m_{max} which needs to be resolved, there is no need to go up to $n_{max} = m_{max}/q$ in order to properly account for resonant modes at this small transverse scale: the toroidal n_ℓ modes characterized by $n_\ell = m_{max}/q + \ell\pi/\Delta\varphi$ will already do the job.

This interesting property of field-aligned coordinates is evidenced in figure 5.14. We plotted the 2D Fourier transforms of the electric potential ϕ at mid-radius at the end of the simulation for different number of grid points in the z direction: $n_z = 10$ and $n_z = 35$. One notices that, in both cases, the spectrum exhibits large amplitude modes (illustrated by the yellow and red colors) outside the exact resonant band $n = -m/q$. This aliasing appears when the number of grid points in z is not sufficient, more precisely when $\Delta\varphi = 2\pi/n_z$ is bigger than half the inverse of the biggest physically relevant wavenumber n_{max} (after the Nyquist-Shannon theorem). In this case, the mean *exact* parallel wavenumber $\langle k_{\parallel}\rangle$ defined as

$$\langle k_{\parallel}\rangle = \left\{ \frac{\sum_{m,n}(n+m/q)^2\ |\hat{\phi}_{m,n}(r,t)|^2}{\sum_{m,n}|\hat{\phi}_{m,n}(r,t)|^2} \right\}^{1/2} \qquad (5.16)$$

is large. It is equal to 12 and 10.5 for these two respective cases (see fig.5.15). Conversely, the mean *effective* parallel wavenumber $\langle k_{\parallel}^{FCI}\rangle$, computed from flux-coordinate independent (FCI) field-aligned coordinates and defined as:

$$\langle k_{\parallel}^{FCI}\rangle = \left\{ \frac{\sum_{m,n}\left\{\sin[(n+m/q)\Delta\varphi]/\Delta\varphi\right\}^2\ |\hat{\phi}_{m,n}(r,t)|^2}{\sum_{m,n}|\hat{\phi}_{m,n}(r,t)|^2} \right\}^{1/2} \qquad (5.17)$$

remains small, of the order of 1 in both cases (cf. fig.5.15). This is due to the fact that aliasing leads to modes which still satisfy the condition for effective resonance, namely $n_\ell = -m/q + \ell\pi/\Delta\varphi$, with $\ell \in \mathbb{N}$ and $\Delta\varphi = 2\pi/n_z$ (oblique dash lines on fig.5.14). In other words, numerical methods which rely on (θ, φ) coordinates to compute the parallel derivative would interpret those off-diagonal modes as non-resonant ones, with large $k_\parallel$, while field-aligned coordinates are still able to correctly interpret them as effectively resonant ones.

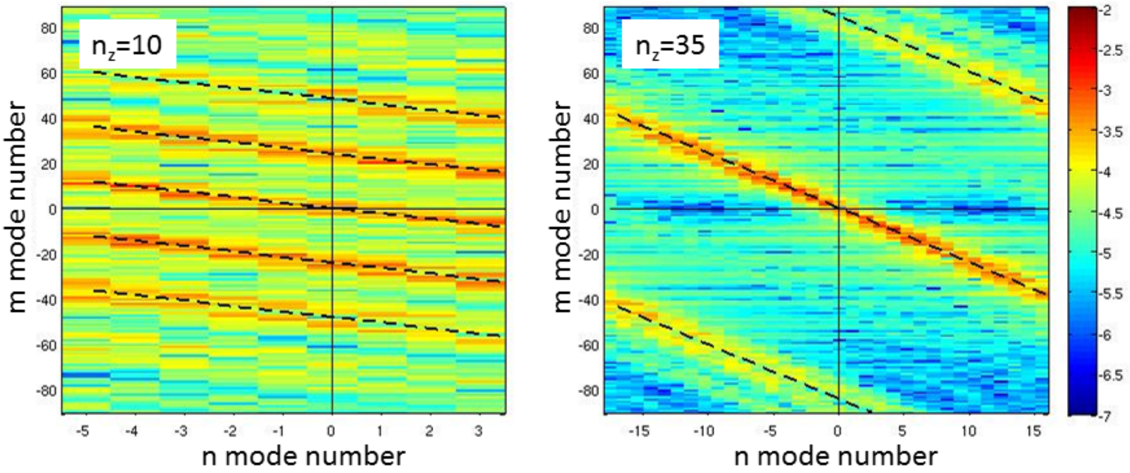

Figure 5.14: 2D Fourier transform of the electric potential ϕ at mid-radius and at the end of the simulation runs for two different grid meshes in the axial direction: $n_z = 10$ (left) and $n_z = 35$ (right). The oblique dash lines satisfy the relation $n_\ell = m/q + \ell\pi/\Delta\varphi$, with $\ell \in \mathbb{N}$ and $\Delta\varphi = 2\pi/n_z$.

The main interesting result is that the FCI approach permits a coarser mesh in the z direction while still allowing high resolution of the perpendicular spatial dimensions, where the small scales occur, and best representing the physical properties of the model. As Fig. 5.16 shows, the convergence is almost perfect, with similar values of the square of the electric potential obtained starting $nz = 15$ only. Because the aim is to represent the Physics in the most economical way, it is thus proven that the FCI system is indeed a judicious choice of coordinate transformations best suited for describing the wave dynamics along the field lines and providing us with even more efficiency and more flexibility in solving anisotropic 3D problems. In the next section, we further prove that this coordinate system is equally powerful at the separatrix (X-point) region.

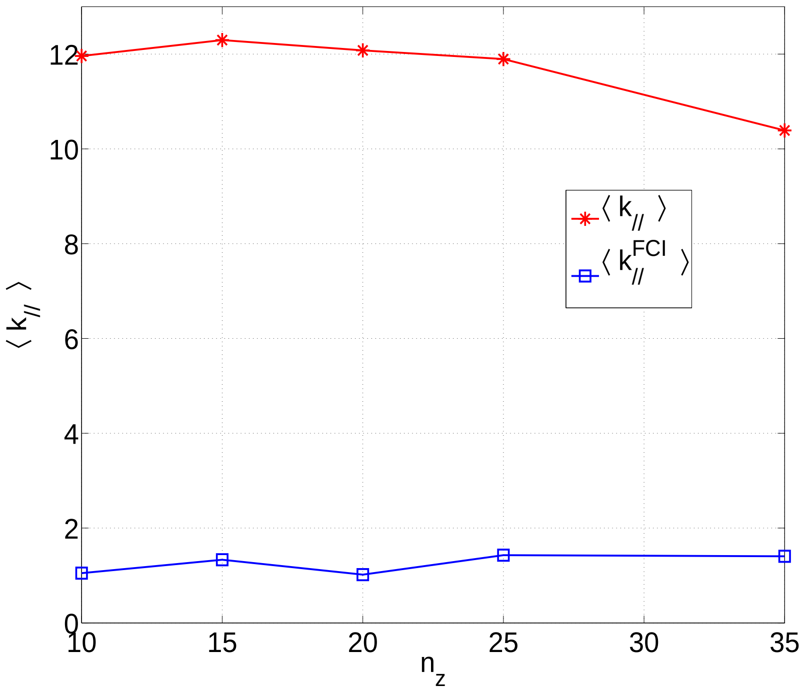

Figure 5.15: Exact and effective mean parallel wavenumbers (see text) as a function of the number of grid points along z.

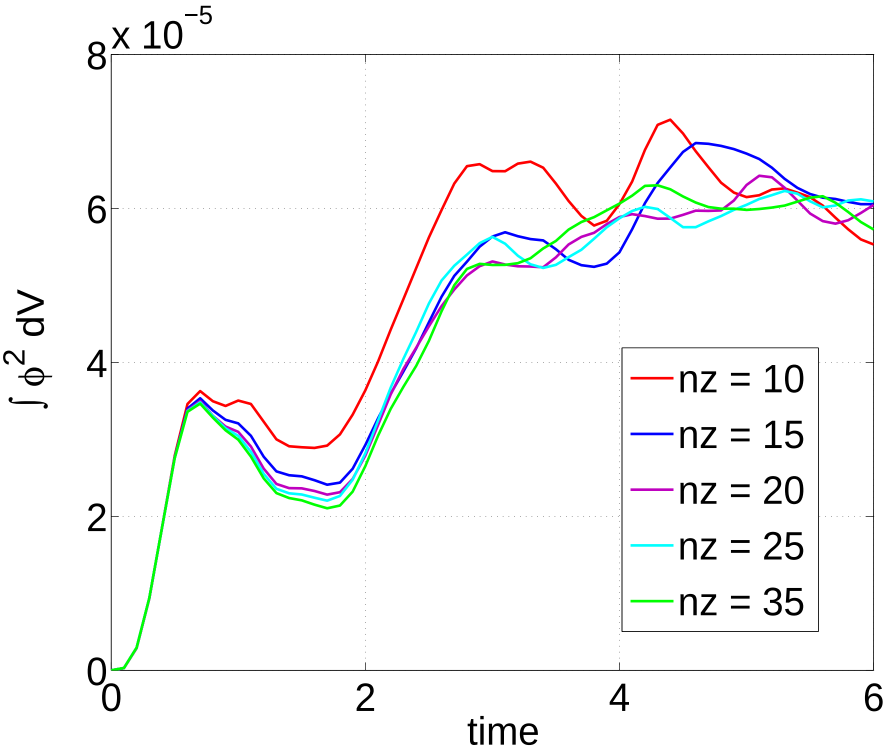

Figure 5.16

5.4 Test Case for the Island Geometry

As extensively discussed before, the Flux-Coordinate Independent system (FCI) allows the parallel derivative to be constructed by tracing the magnetic field lines from one perpendicular plane to the next, and interpolating to find the desired quantity. This frees us from using flux coordinates in the perpendicular plane,thus allowing for complex magnetic geometries free of singularities. Since FENICIA is easily extensible to different meshes and coordinate systems, we use it here to demonstrate the application of the FCI coordinate system to a magnetic island in a slab version of the code. Dirichlet boundary conditions are still used in the x direction, but periodic boundary conditions are now set in the y and z directions. The results of our investigation are presented into the influence of a static $n = 0$ magnetic island including both the X- and O- points on drift-wave turbulence.

5.4.1 Exact solutions for the island exterior and interior

In the remainder of this section, we will consider a magnetic equilibrium characterized by a magnetic island whose half radial width is equal to $\delta_x = 2\sqrt{A}$, with A being a parameter. Such an equilibrium corresponds to a magnetic field given by Eqs. (2.9)-(2.10), with:

$$\psi(x,y) = -\frac{(x-1)^2}{2} + A\cos(y) \tag{5.18}$$

The considered domain is $x_{min} \leq x \leq x_{max}$ (in practice, $x_{max} = 1 + \Delta$ and $x_{min} = 1 - \Delta$, with $0 < \Delta < 1$) and $-\pi \leq y \leq \pi$, with $0 \leq z \leq 2\pi$.

Let us consider the following model pertaining the parallel dynamics

$$\begin{aligned} \partial_t \phi + C\,\nabla_\parallel u &= 0 \\ \partial_t u + \frac{C(1+\tau)}{\tau}\,\nabla_\parallel \phi &= 0 \end{aligned} \tag{5.19}$$

where the parallel gradient operator reads as follows:

$$\nabla_\parallel = -[\psi, \cdot] + \partial_z \tag{5.20}$$

The aim of the present section is to construct exact solutions of model (5.19) in the magnetic equilibrium defined above, i.e. in the presence of a magnetic island. These solutions will then serve as test beds for the numerical benchmarks discussed in next subsection. To do so, one needs to define proper coordinates associated to the field lines. It readily appears that ψ is a label of magnetic field lines, since $\nabla_\parallel \psi = 0$. The coordinate η is a straight-field-line angle-like variable and has still to be calculated.

Let us introduce the following new set of coordinates:

$$\rho = -\psi/A = \frac{(x-1)^2}{2A} - \cos y \tag{5.21}$$

$$\eta = g(\rho) \int_0^y \frac{dy'}{[\cos y' + \rho]^{1/2}} \tag{5.22}$$

As detailed in appendix D, for η to be an angle ranging from $-\pi$ to π, $g(\rho)$ has to be given different expressions depending on whether ρ is bigger or smaller than 1, $\rho = 1$ being the radius at the separatrix of the island. The exterior of the island corresponds to the region where $\rho > 1$, while $\rho < 1$ characterizes the interior of the island.

For the exterior region $\rho > 1$, $g(\rho)$ has the following expression:

$$g(\rho)|_{\rho>1} = \frac{\pi}{2}(1+\rho)^{1/2} \left[K\left(\frac{2}{1+\rho}\right)\right]^{-1} \tag{5.23}$$

where K stands for the elliptic integral of the first kind:

$$K(x) \equiv \int_0^{\pi/2} d\theta \, (1 - x\sin^2\theta)^{-1/2} \tag{5.24}$$

Conversely, $g(\rho)$ reads as follows for the interior region $\rho < 1$:

$$g(\rho)|_{\rho<1} = \frac{\pi}{2\sqrt{2}} \left[K\left(\frac{1+\rho}{2}\right)\right]^{-1} \tag{5.25}$$

The resulting graphs of both ρ, defining the island geometry, and of η in the inner and outer regions of the island, are visible on figures 5.17a-5.17b. So far, we do not have an expression of $g(\rho)$ at the position of the separatrix, at $\rho = 1$. This prevents us from finding exact analytic solutions at $\rho = 1$. This issue is left for future investigation.

It can be shown that the parallel gradient takes the following compact expression in terms of this new set of coordinates:

$$\nabla_\parallel = g(\rho)\sqrt{2A}\frac{\partial}{\partial\eta} + \frac{\partial}{\partial z} \tag{5.26}$$

Let us then look for wave-like solutions of the model (5.19) of the form:

$$\begin{pmatrix} \phi(\rho,\eta,t) \\ u(\rho,\eta,t) \end{pmatrix} = \begin{pmatrix} \phi_0(\rho) \\ u_0(\rho) \end{pmatrix} \cos\left[m\eta - nz - \omega(\rho)t\right] \tag{5.27}$$

with (m, n) standing for the wave numbers in η and z, and $\omega(\rho)$ being the mode frequency. Injecting these expressions in Eq. (5.19) leads to the following system:

$$\begin{pmatrix} -\omega & C\left[g(\rho)\sqrt{2A}m - n\right] \\ \frac{C(1+\tau)}{\tau}\left[g(\rho)\sqrt{2A}m - n\right] & -\omega \end{pmatrix} \begin{pmatrix} \phi_0(\rho) \\ u_0(\rho) \end{pmatrix} = 0 \tag{5.28}$$

The eigenfrequency solution of the dispersion relation depends on ρ:

$$\omega_{\pm}(\rho) = \pm C \left(\frac{1+\tau}{\tau}\right)^{1/2} \left[g(\rho)\sqrt{2A}\,m - n\right] \tag{5.29}$$

The eigenvectors are then such that:

$$u_0(\rho) = \frac{C(1+\tau)}{\tau\omega_{\pm}}\,\phi_0(\rho) \tag{5.30}$$

For a given expression of $\phi_0(\rho)$, u_0 can be calculated by using Eq. (5.30), with $\omega_{\pm}$ given by Eq. (5.29). Then, Eq. (5.27) provides exact solutions of the model (5.19), which will be compared to their numerical counterparts in the next subsection.

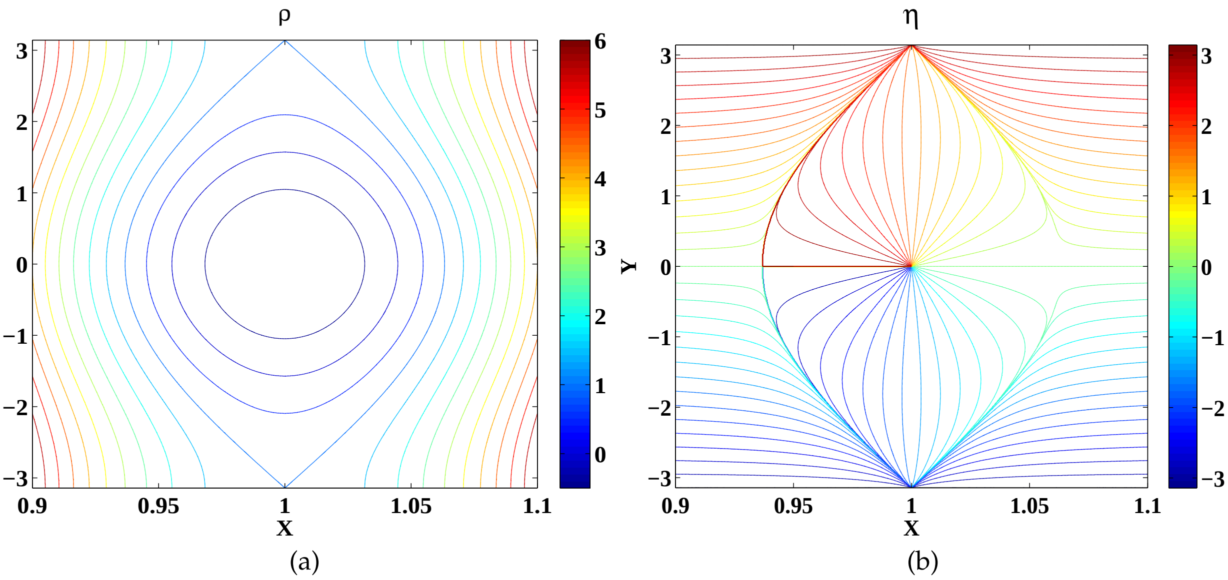

(a) (b)

Figure 5.17: The new coordinates ρ (a) and η (b) as a function of the grid mesh coordinates (x, y).

5.4.2 Numerical tests at the exterior and interior of the island

The first test aims at verifying that the numerical simulation of drift-wave propagation across the X-point gives results in good agreement with the exact solutions of this problem up to the order of accuracy of the chosen numerical scheme. We consider a box of size $\Delta = 0.1$, an island of size $4\sqrt{A}$ with $A = 10^{-3}$ and a mode (m, n) resonant at $\rho = \rho_{mn}$, i.e: $m/n = 1/(g(\rho_{mn})\sqrt{2\,A})$. This means that $k_{\parallel} = 0$ at ρ_{mn}. For this value of A, we plot $1/(g(\rho_{mn})\sqrt{2\,A})$ as a function of ρ for both the exterior and the interior of the island as shown in Figs .(5.18a-5.18b). For rational values of $1/(g(\rho)\sqrt{2\,A})$, there exists a resonant (m, n). One sees that the position around $\rho = 1$ is directly constrained by high (m, n) values, especially if

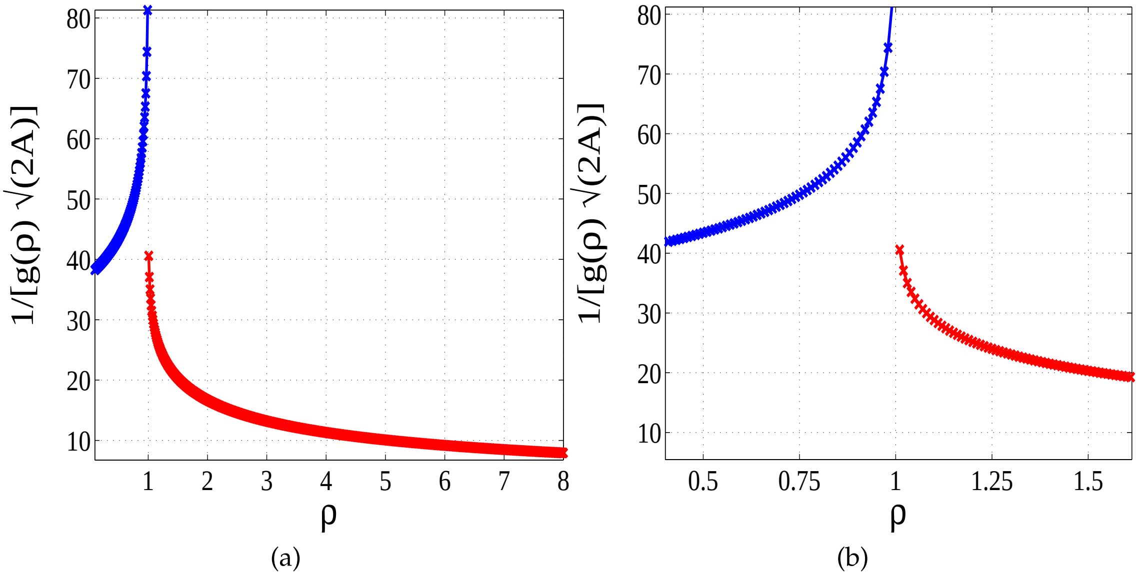

(a)

(b)

Figure 5.18: (a) plot of m/n as a function of ρ for both the exterior and the interior of the island (b) zoomed view around the separatrix region $\rho = 1$

one wishes to get closer to the separatrix starting from the interior of the island. The next step is to initialize a perturbation

$$\phi(t=0) = \phi_0(\rho)\cos(m\eta - nz) \tag{5.31}$$

where $\phi_0(\rho)$ is a Gaussian structure centered around ρ_{mn} and having the following form

$$\phi_0(\rho) = \exp\left[-\frac{(\rho-\rho_{mn})^2}{\Delta\rho^2}\right] \times \left(\frac{\rho}{\rho_{mn}}\right)^m \times \left(\frac{\rho-\rho_{bd}}{\rho_{mn}-\rho_{bd}}\right)^2 \tag{5.32}$$

with $\Delta\rho = \rho_{mn}/m$ and ρ_{bd} is the value of ρ at the boundaries $x = \{x_{min}, x_{max}\}$ for $y = 0$. The small radial width of the envelope ϕ_0, around the resonant surface ρ_{mn}, ensures that $k_\| \ll 1$. Two cases are to be examined: the exterior of the island ($\rho > 1$), and the interior ($\rho < 1$). The only difference between the two cases comes from the two different expressions of $g(\rho)$ given by Eq. (5.25) in the previous subsection. For the former one, we consider a perturbation $\phi_0(\rho)$ centered around $\rho_{mn} = 1.25$ for $(m,n) = (24,1)$. The initial condition for a simulation of size $(800 \times 800 \times 20)$ is shown in Fig. 5.22a. With a time step $\Delta t = 10^{-3}$, the simulation is run 1000 times up to $t = 1$ and the solution at the final time is given in Fig 5.22b. For clarity, a zoomed view of the initial and the final solution are also shown in Figs. (5.20a-5.20b).

The emphasis is now on showing that the exact slab solution given by (5.27) is recovered at the exterior of the island where $\rho > 1$. In Fig. (5.21), we plot the relative error

$$\frac{\left\langle(\phi_{num}-\phi_{exact})^2\right\rangle^{1/2}}{\left\langle(\phi_{exact})^2\right\rangle^{1/2}} \tag{5.33}$$

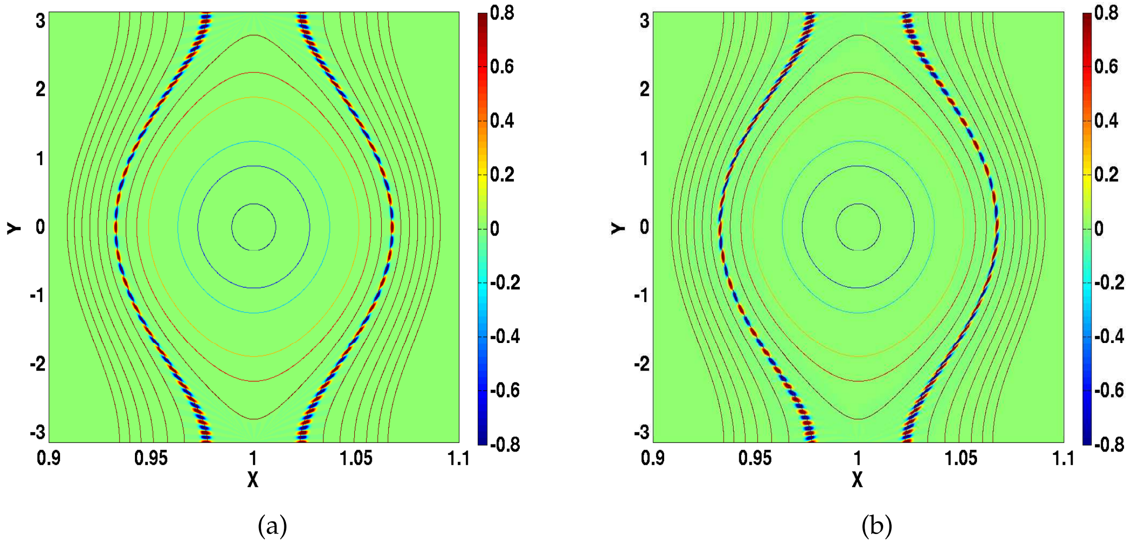

(a) (b)

Figure 5.19: (a) Initial condition $\phi(t=0)$ (b) solution ϕ at the final time step $t=1$

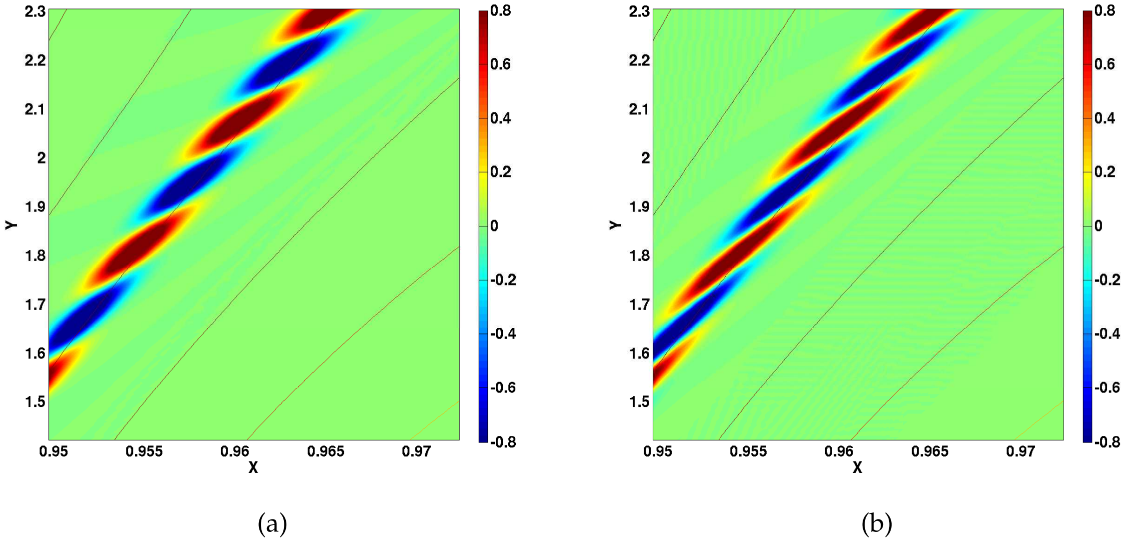

(a) (b)

Figure 5.20: (a) zoomed view of the initial condition $\phi(t=0)$ (b) zoomed view of the solution ϕ at the final time step $t=1$

between the exact and the numerical solution as a function of time for different spatial resolutions $(nx, ny, nz) = \{(400, 400, 20); (600, 600, 20); (800, 800, 20)\}$ where $\langle . \rangle = \int_0^{2\pi} dy \int_0^{2\pi} dz \int_1^{x_{max}} dx$. From Fig. 5.21, we see that the numerical results converge quickly to the analytic solution.

The same tests are performed at the interior of the island where we consider a perturbation $\phi_0(\rho)$ centered around $\rho_{mn} = 0.58$ for $(m, n) = (45, 1)$. The initial condition for a simulation of size $(800 \times 800 \times 20)$ is shown in Fig. 5.22a and the

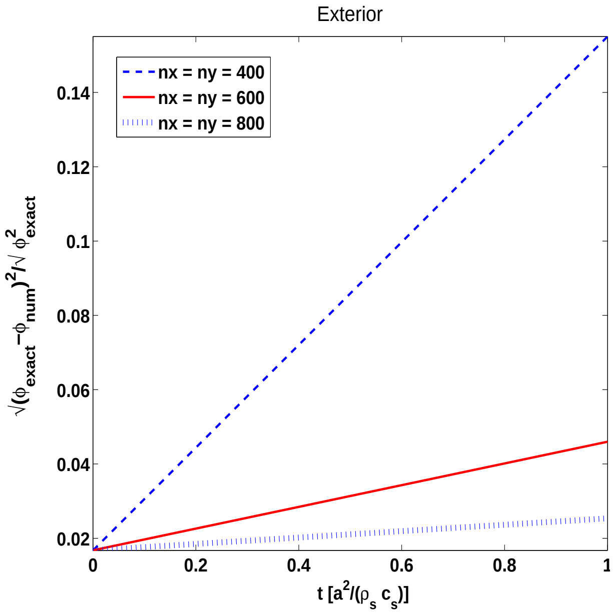

Figure 5.21: errors as a function of time given by different spatial resolutions

final solution at $t = 1$ is given in Fig 5.22b. A zoomed view of the initial and the final solution are also shown in Figs. (5.23a-5.23b).

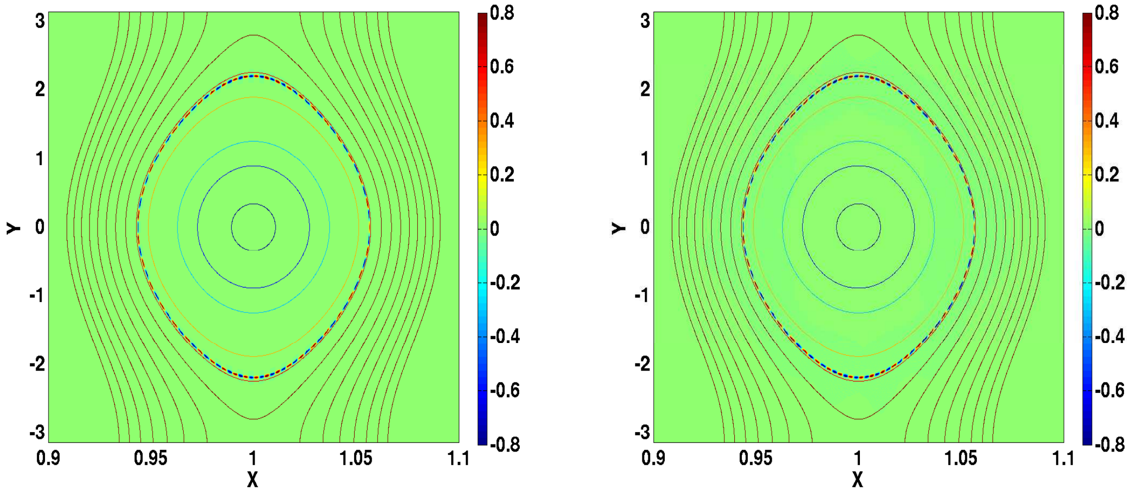

(a) (b)

Figure 5.22: (a) Initial condition $\phi(t = 0)$ (b) solution ϕ at the final time step $t = 1$

The numerical solution is again compared to the analytic solution given by (5.27) for $\rho < 1$. This is illustrated in Fig. (5.24) where we plot the relative error as a function of time. We observe that the numerical solution to the drift-wave problem converges to the exact one as the step size Δx decreases. However, the relative error for the resolutions considered here is still high ($\sim 30\%$). We interpret this by the fact that the poloidal resolution is still not sufficient to be able

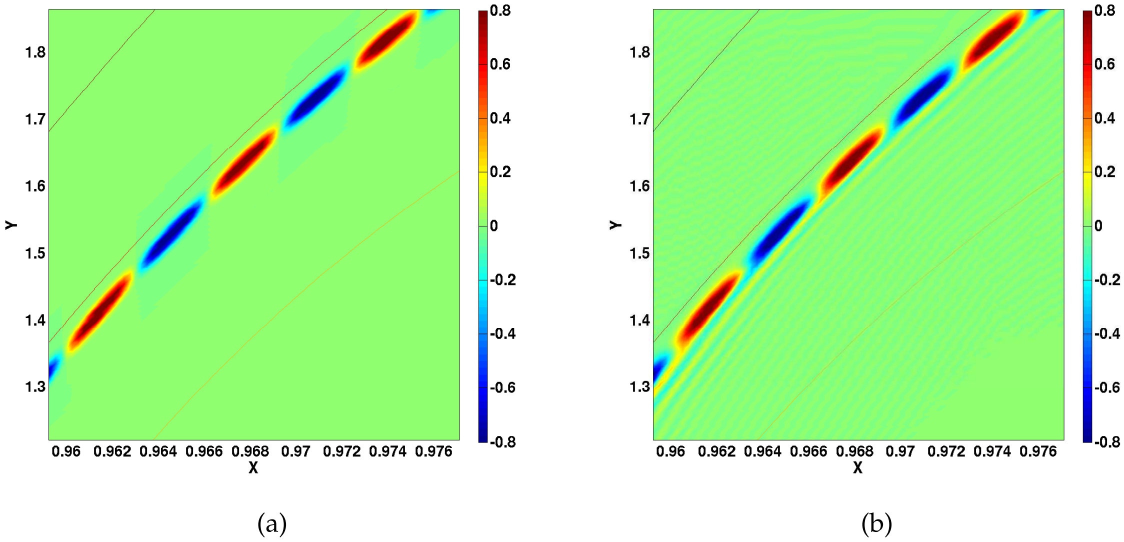

(a)

(b)

Figure 5.23: (a) zoomed view of the initial condition $\phi(t = 0)$ (b) zoomed view of the solution ϕ at the final time step $t = 1$

to resolve the $m = 45$ mode at the interior of the island. Further investigations are ongoing to widen the box size and the island's width in order to allow us to take a smaller poloidal resonant mode number m.

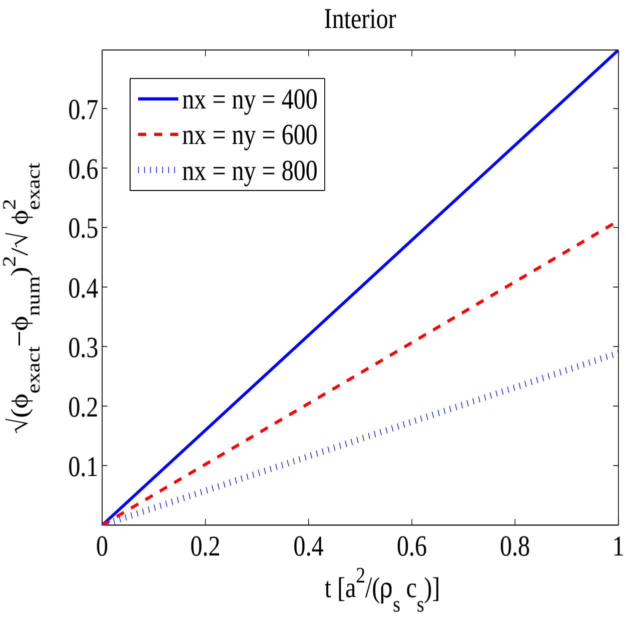

Figure 5.24: errors as a function of time given by different spatial resolutions

5.4.3 Tests across the separatrix

At the separatrix, where $\rho = 1$, the analytic solutions (5.27) are no longer valid. As stated in subsection 5.4.1, we do not have an expression for an analytic exact solution at the separatrix, should such a solution exist. Given this limitation, instead of considering an initial condition as a function of the variable η that diverges at $\rho = 1$, we thus consider a perturbation crossing the separatrix of the form

$$\phi(t) = N_0(\rho)\cos(my - nz) \tag{5.34}$$

where $N_0(\rho)$ is a Gaussian structure given by

$$N_0(\rho) = \mathrm{e}^{-(\rho-1)^2/\Delta\rho^2} \tag{5.35}$$

where $\Delta\rho$ is a parameter set to $\Delta\rho = 0.5$ here for the perturbation to cover both the left and right-hand sides of the separatrix. A series of simulations is then run with $\Delta = 0.1$, $A = 10^{-3}$ and $(m, n) = (5, 1)$. Figures (5.25-5.26-5.27) show the evolution of the electrostatic potential as a function of time (Bohm time). The time step for this simulation is $\Delta t = 10^{-3}$ and the box size is $(200 \times 200 \times 20)$. From Fig. 5.25 one sees that modes across the separatrix gradually evolve and shear. Due to the periodicity of the simulation box, we also observe eddies sticking out of one side of the box and reentering on the other side of the box. This process goes on until $t = 7$ when the solution breaks up into separate filaments that bunch together at the level of the X-point for the poloidal resolution is no more sufficient at this stage as it appears in the 2D snapshots of Fig. 5.26. 3D illustrations are shown in Fig. 5.27 showing the same simulation described above in its 3D state up to $t = 5$.

Because our ultimate goal was to prove the validity of the FCI approach for X-point geometries, three main tests are to be considered hereafter. The first test consists in showing the conservation of an energy-like quadratic quantity of the drift-wave model (5.19). For this purpose, we perform a scan in nx and in nz, the number of points in the x and z directions respectively. For a fixed number of points in the z direction, $nz = 20$, a scan over the following pairs is done in the x and y directions: $(nx, ny) = \{(100, 100); (200, 200); (400, 400); (600, 600)\}$ until $t = 1$. The Energy $E \equiv \int(\phi^2 + (1 + 1/\tau)^{-1} u^2)/2\, dxdydz$ is trivially conserved by Eqs. (5.19). It is plotted in Fig. 5.28a as a function of time. The conservation of E is guaranteed as the displacement Δx decreases (in all simulations we considered $n_x = n_y$). The line plot on the right-hand side graph 5.28b shows that it is effectively the case since in the worst case where $(nx, ny) = (100, 100)$ the relative change is equal to 4.5×10^{-3} and in the well-resolved case where $(nx, ny) = (600, 600)$ the relative change is almost null.

For the special case where the box size is $(nx, ny, nz) = (200, 200, 20)$ shown in the 2D and 3D snapshots above, we performed the run up to $t = 12$. Though there are filaments appearing after $t = 6$, the plot in graph 5.29a shows a relatively good conservation of the Energy. The rate of change as a function of time, as calculated in the plot of 5.29b reaches at most 5%.

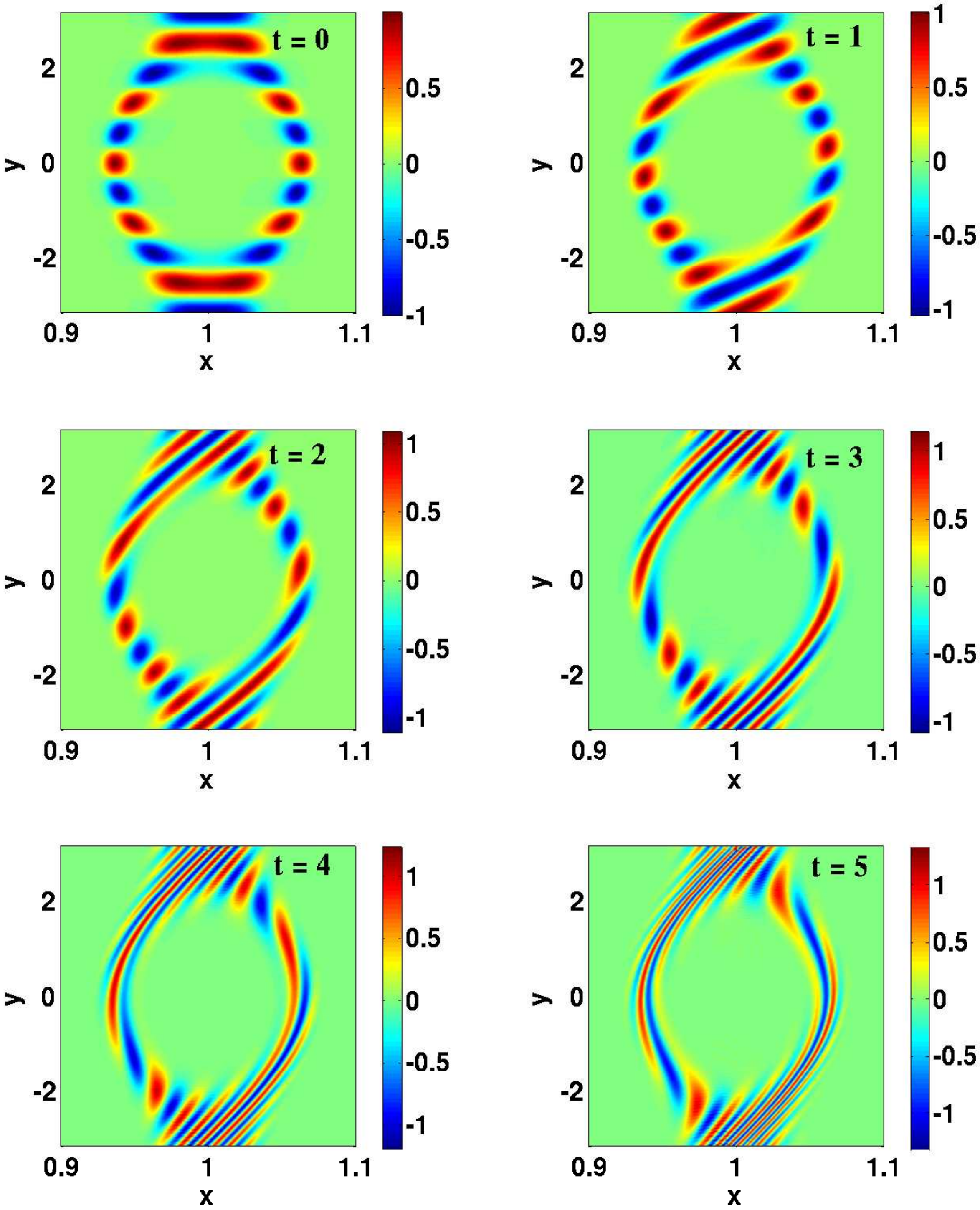

Figure 5.25: 2D snapshots of potential fluctuations at different simulation times

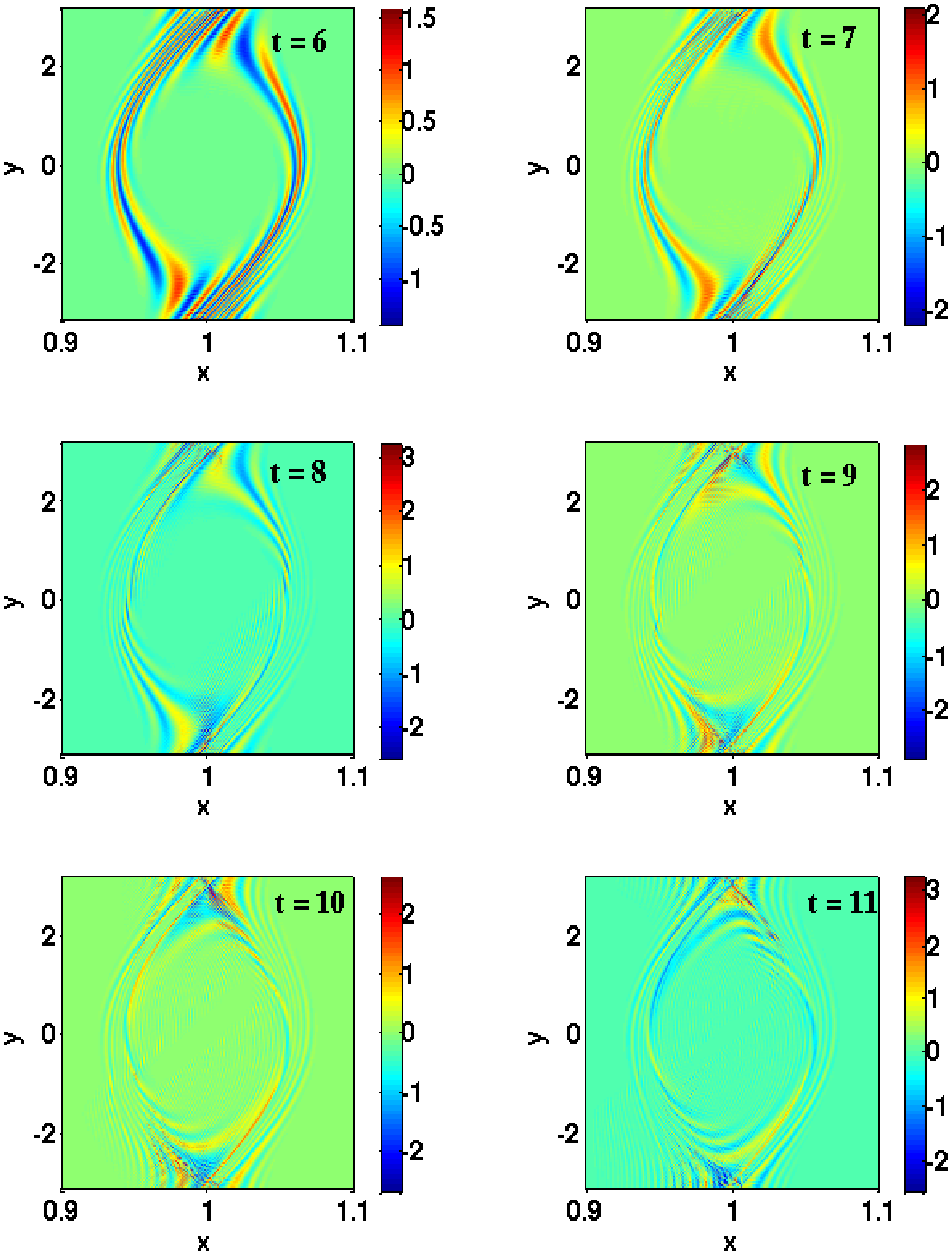

Figure 5.26: 2D snapshots of potential fluctuations at different simulation times

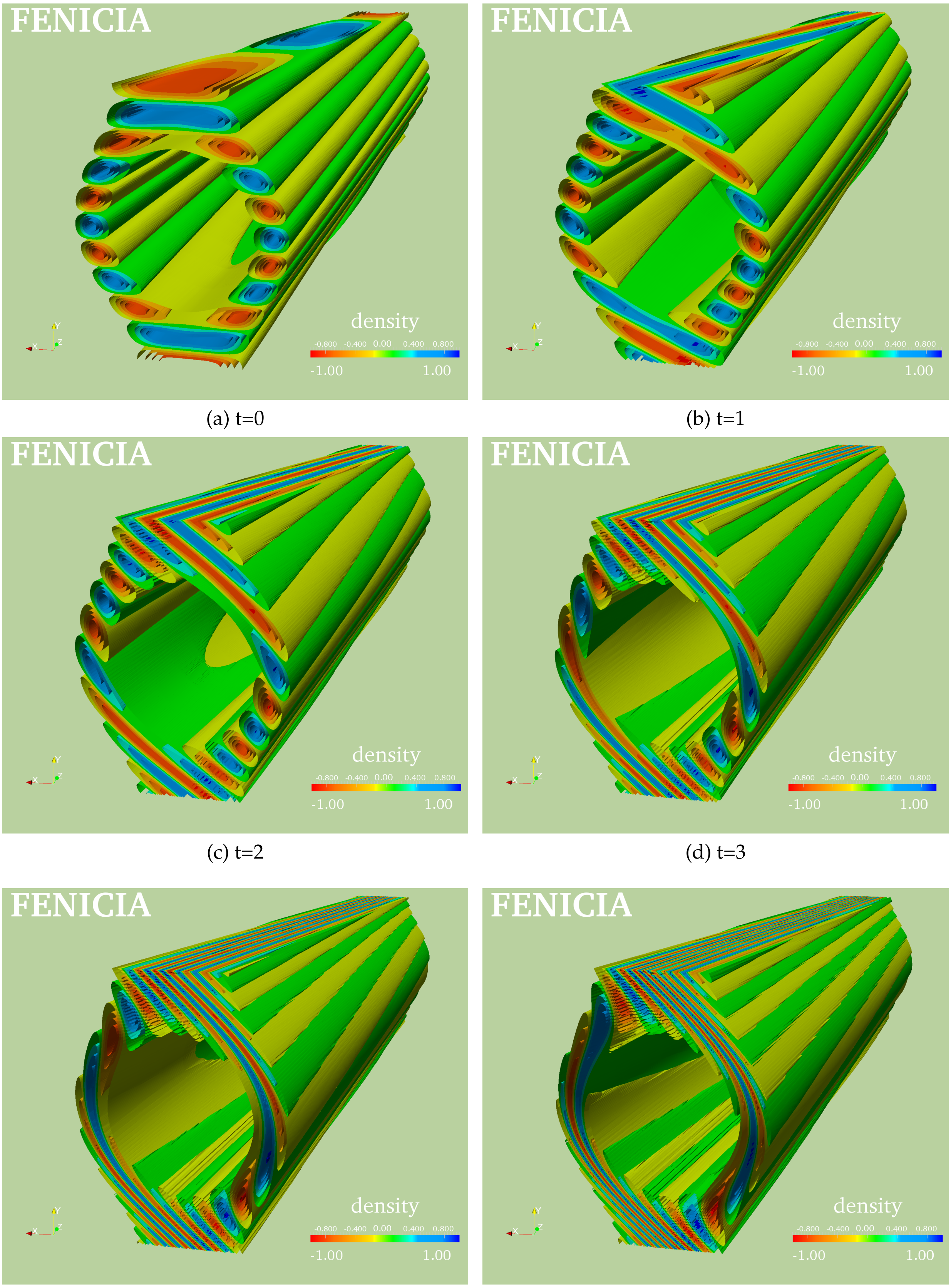

(a) t=0

(b) t=1

(c) t=2

(d) t=3

(e) t=4

(f) t=5

Figure 5.27: 3D snapshots of potential fluctuations at different simulation times

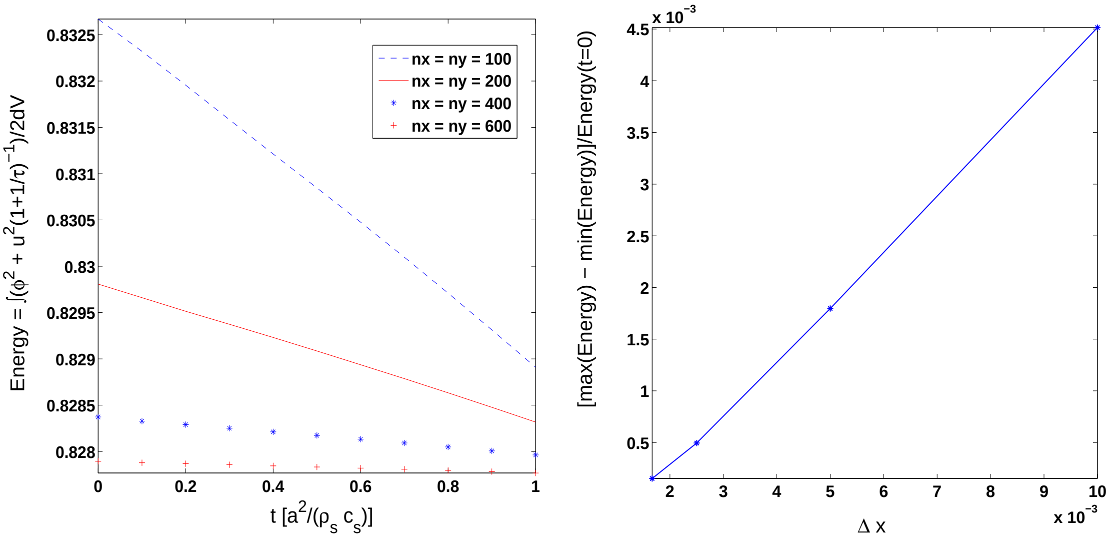

(a) (b)

Figure 5.28: (a) Conservation of Energy at the separatrix with respect to time for different spatial resolutions (b) The relative change in energy with respect to Δx

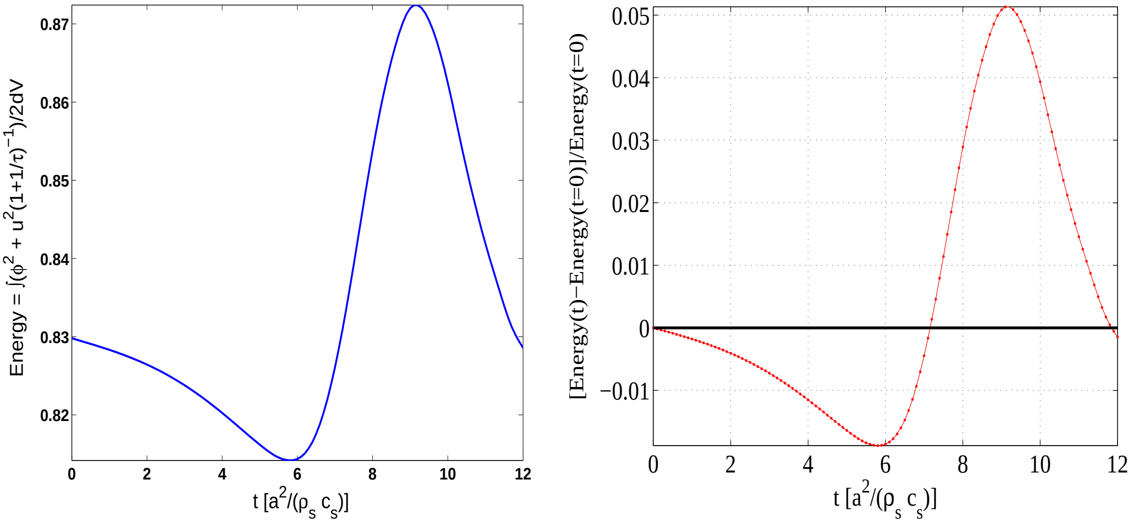

(a) (b)

Figure 5.29: (a) Conservation of Energy at the separatrix for a long simulation up to $t = 12$ with $(nx, ny, nz) = (200, 200, 20)$(b) The relative change in energy with respect to time

Similarly, the conservation of the Energy is well verified when scanning the number of points in the z direction. A box of size $(nx, ny, nz) = (400, 400, nz)$ is considered where $nz = \{20, 40, 60, 80, 100\}$. In graph 5.30a, the energy converges perfectly well as Δz decreases. Furthermore, its relative change is in the worst case equal to 5×10^{-4} as shown in Fig. 5.30b.

The second important test targets the demonstration of the convergence

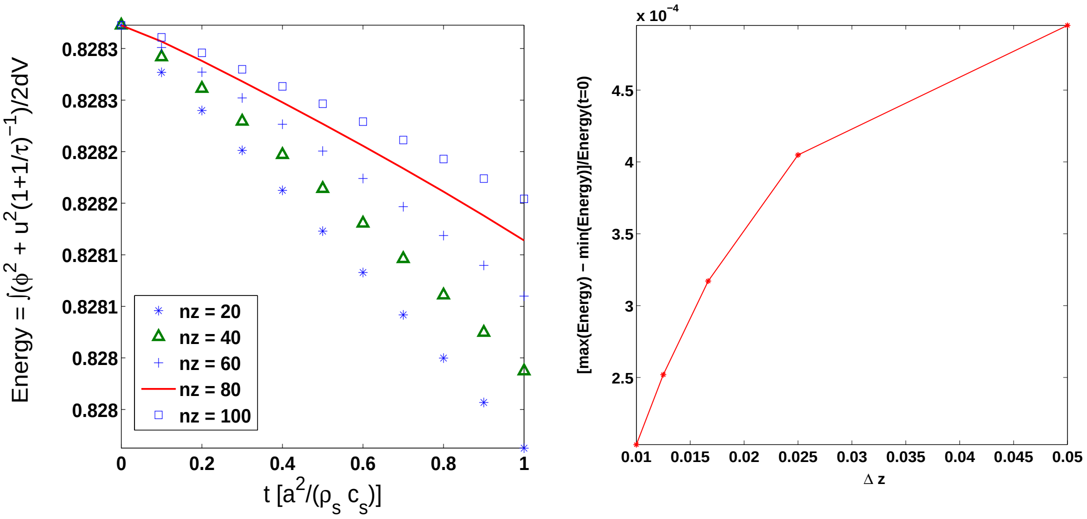

(a) (b)

Figure 5.30: (a) zoomed view of the initial condition $\phi(t = 0)$ (b) zoomed view of the solution ϕ at the final time step $t = 1$

of the numerical solution when crossing the separatrix region. A series of simulations performed with a box of size $(nx, ny) = (400, 400)$ and $nz = \{5, 10, 20, 40, 60, 80, 100\}$ are again considered for this purpose. We start by considering the first two solutions given by the simulations having $nz = 5$ and $nz = 10$. The idea is to calculate the difference between the two and repeat the process over each pair of solutions. The process should be repeated over the entire set of solutions ϕ given by all the simulations. It is called the *moving difference*. In Fig. 5.31 and 5.32 the moving difference of the solutions is plotted in $2D$ at the final time $t = 1$ for the first poloidal plane $iz = 1$. We clearly see that the difference is equal to zero after $nz = 40$. Which means that one does not need to go beyond $nz = 40$ for this simulation to study the same physics. This constitutes the main strength of the field-aligned FCI approach and validates its application to X-point configurations with a high exponential convergence rate shown in graph 5.33.

The graph of Fig. 5.33 indeed shows a plot line connecting all the fixed averages. It is called the moving average. More specifically, the average is calculated by dividing the sum of the difference between each pair of solutions by the total number of solutions. It is thus a mean that allowed us to prove that the numerical solution converges exponentially as the displacement in the z direction, Δz, decreases. To finish, we effectively do a last test showing the order of convergence of the numerical solution. In fact, for the same set of simulations, i.e: $(nx, ny) = (400, 400)$ and $nz = \{5, 10, 20, 40, 60, 80, 100\}$, the test consists of choosing a reference case supposed to be the closest possible case to the exact solution. With this hypothesis, it is legitimate to calculate the average of the difference between all the simulations and the reference simulation chosen to be that with $nz = 100$ (Root Mean Squared of the difference). The result is shown in graph 5.34b where we see that as nz tends to 100, the error tends to 0 with an

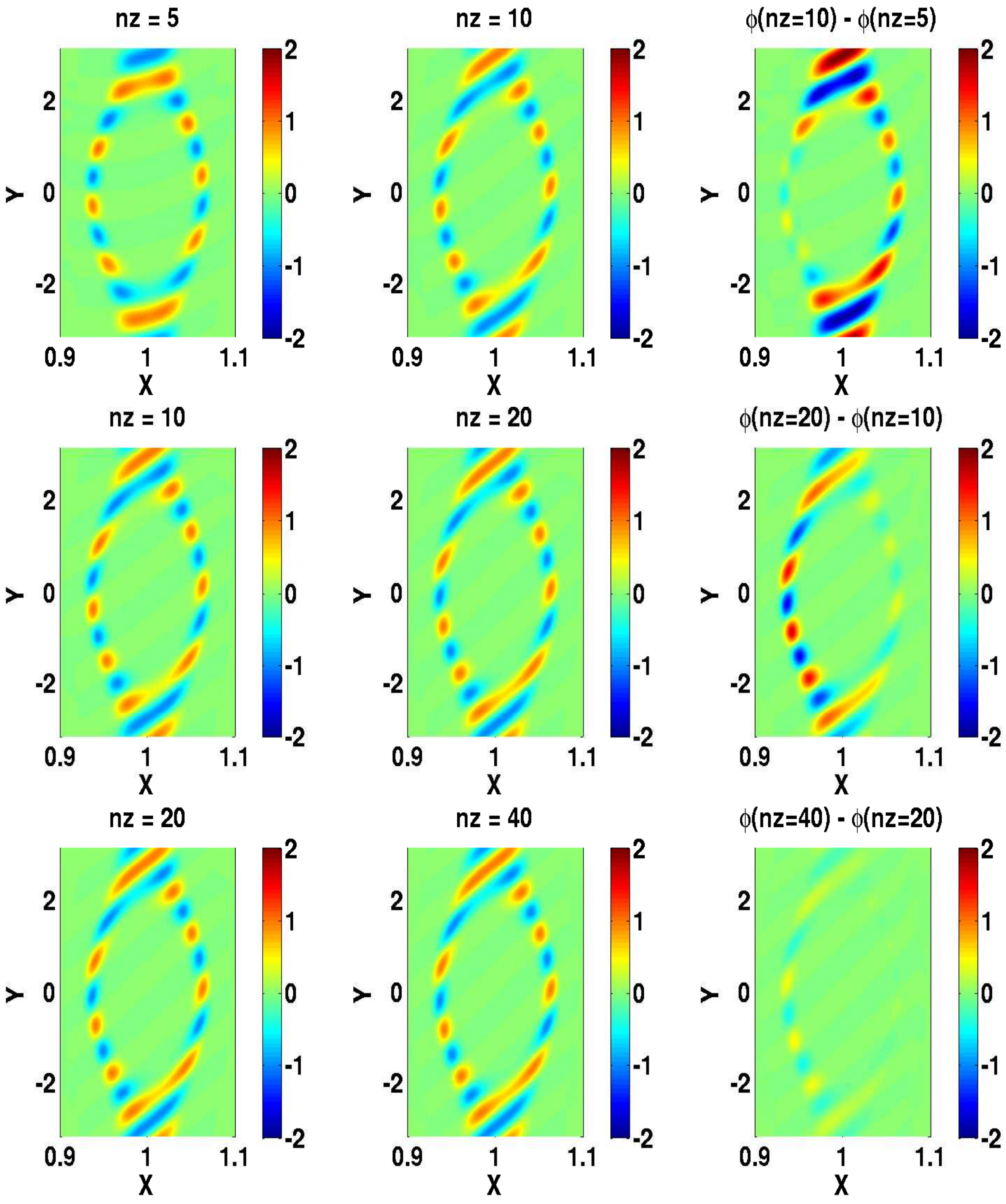

Figure 5.31: Moving difference

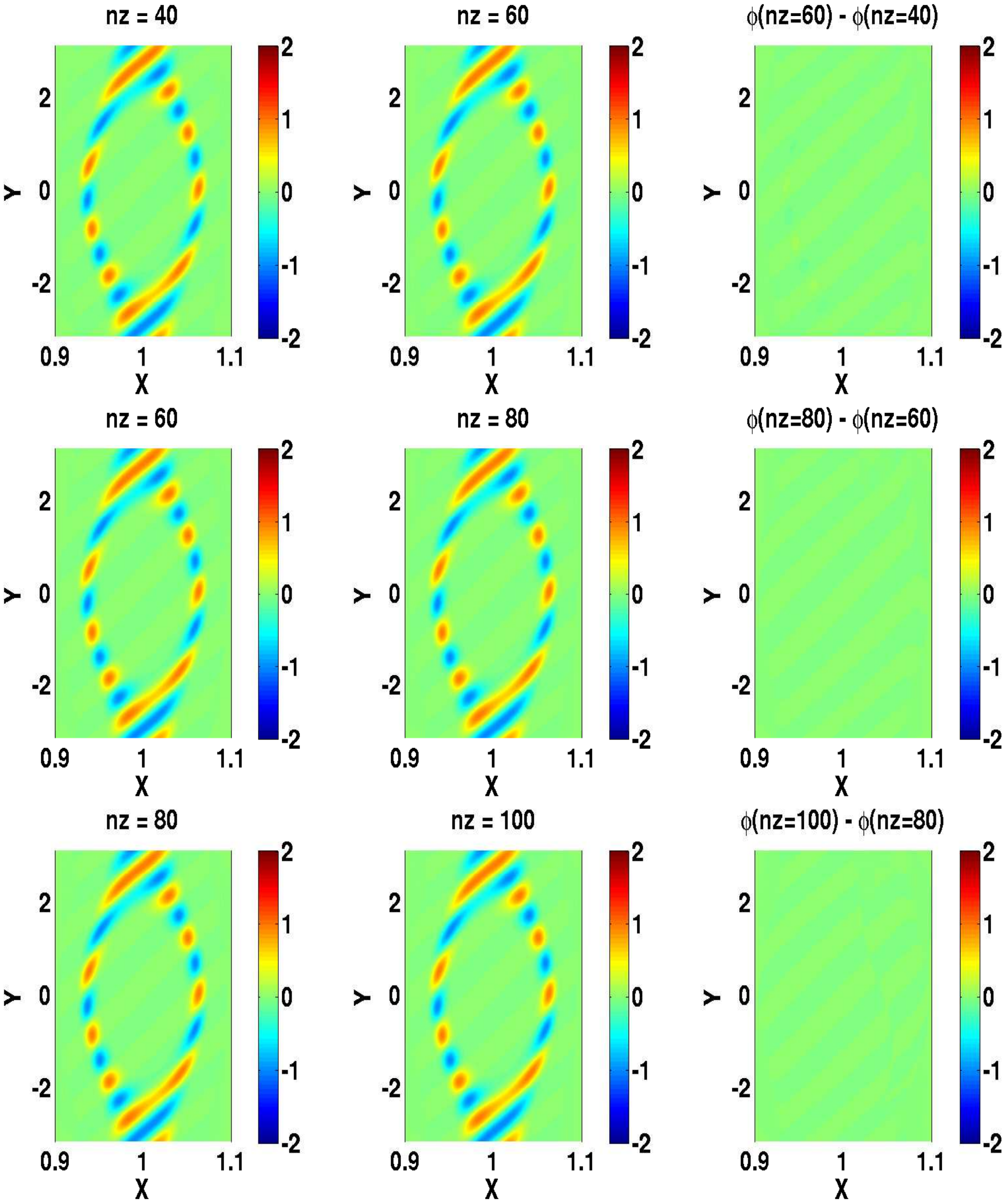

Figure 5.32: Moving difference

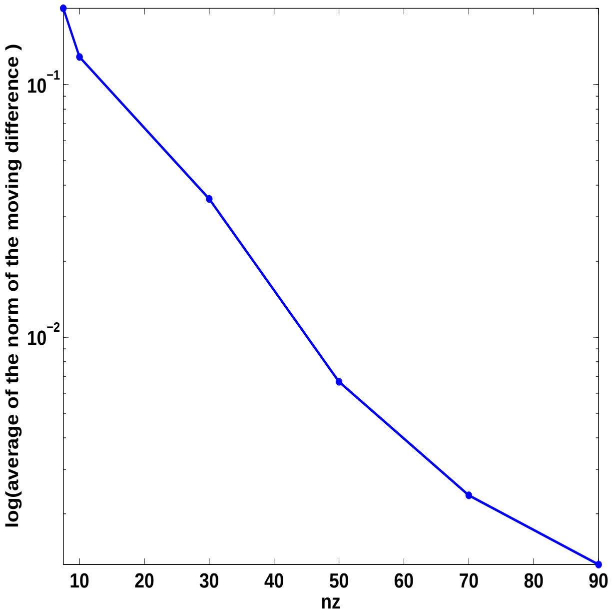

Figure 5.33: Average of the norm of the moving difference showing convergence of the numerical solution in nz at an exponential rate

estimation of the order of convergence given by the loglog plot in Fig. 5.34b. The convergence is indeed fast, of the order of $a = 2.6$, the corresponding slope of the loglog plot.

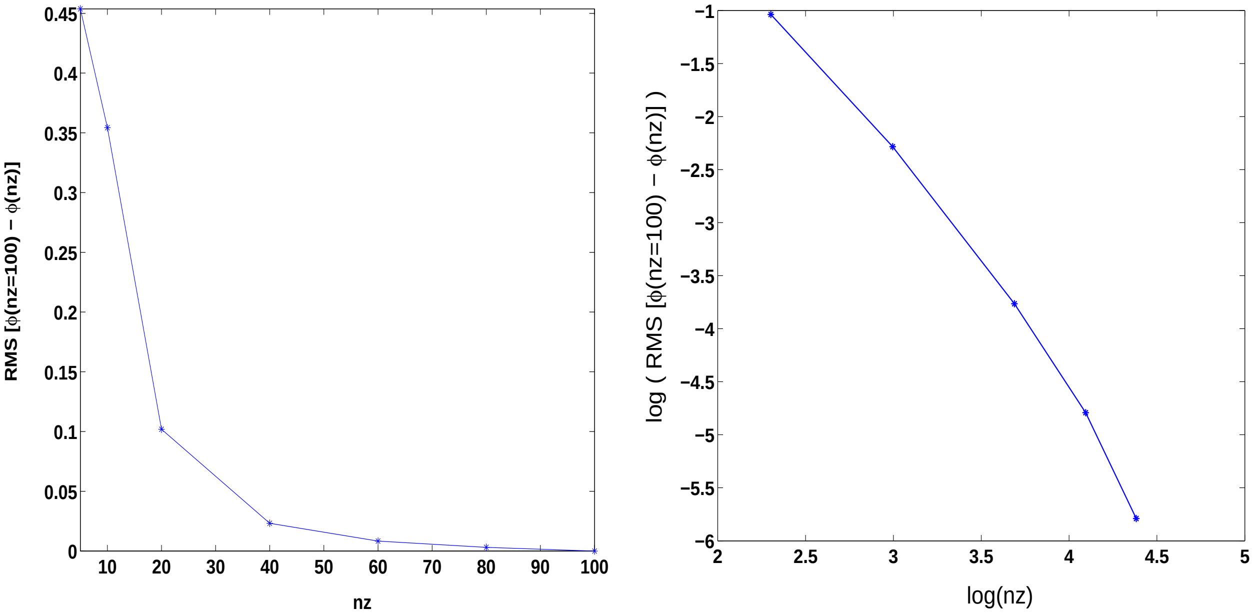

(a) (b)

Figure 5.34: (a)Average of the difference between the numerical solution at different nz values and the solution at the reference case $nz = 100$ (b) loglog plot showing the convergence rate having a slope $a = 2.6$

Chapter 6

Conclusions and Future Work

> تَركُ النُفوسِ بِلَا عِلمٍ وَ لَا أَدَبٍ
>
> تَركُ المَريضِ بِلَا طِبٍّ وَ لَا آسِ
>
> أَحمَد شَوقي (١٨٦٨ - ١٩٣٢)

Contents

Acrylique, (F. Hariri, 2008)

6.1 Highlights from this Thesis

The principle difficulty in achieving fusion in the laboratory arises from the fact that the plasma is typically unstable to magnetohydrodynamical or kinetic instabilities. These instabilities primarily driven by pressure (or temperature or density) and current gradients inherent in tokamak confinement devices, are known to govern plasma turbulence and MHD modes which in turn, seriously impedes reaching the critical Lawson condition. An important step required to reach practical fusion energy is thus the understanding of the mechanism behind the coherent turbulent structures created by plasma drift-wave instabilities. In the fusion community, numerical simulations of plasma micro-turbulence and large-scale MHD instabilities efficiently complement experimental measurements and empirical scaling laws.

The primary thrust of this work has been the development and implementation of a new approach to the problem of field-aligned coordinates in plasma turbulence simulations that I called the FCI approach. The method exploits the elongated nature of microinstability driven turbulence which typically have perpendicular $-$ to the guiding magnetic field $-$ scales on the order of the ion gyroradius, $k_\perp \rho_i \sim 1/2$, and parallel scales on the order of the machine size $\sim q\,R$. Mathematically speaking, it relies on local transformations that align a suitable coordinate to the magnetic field to allow efficient computation of the parallel derivative. However, it does not rely on flux coordinates and this permits discretizing any given field on a regular grid in the natural coordinates such as (R, Z, φ) or (x, y, z) in the cylindrical limit. The several advantages of the FCI approach over the old ones have been illustrated in Chapter 2. In particular, I demonstrated that the method allows a more natural treatment of the operations in the poloidal plane and deals without difficulty with X-point configurations and with O-points such as the magnetic axis, since it is constructed on coordinate systems with non-singular metric.

In light of these findings, I have developed a plasma simulation code in Fortran that I called FENICIA, which successfully reproduces linear and nonlinear microturbulence regimes. MHD regimes may be included in the code as well, but this has been left for future work. The code's features are detailed in Chapter 3. In short, FENICIA is a modular code solving the class of plasma models 1.19 and using the FCI approach. Operators relevant to the targeted ITG physics have been implemented. Thus, any combination of these operators can be solved by the code and addition of more operators is easy due to the modularity of the program. Thanks to the Flux Coordinate Independent field-aligned approach (FCI), FENICIA is flexible enough to permit switching between different types of magnetic geometries including the separatrix region.

The FCI approach requires interpolation in the poloidal plane. To this end, Hermite cubic interpolation with direct computation of the derivatives at the control points has been employed. Tests in Chapter 4 show that this choice is as accurate as cubic splines but more efficient in terms of computational resources. Tests using FENICIA were also carried out on the problem of spurious (numerical) diffusion of zonal fields, and on the problem of drift-wave propagation. With the zonal field test I show that the numerical diffusion rate due to the new method is negligible with respect to the evolution rate of actual physics processes of interest. On the other hand, with the wave propagation tests, I show that the error per unit time due to the computation of parallel derivatives with the new method is sub-dominant with respect to the error due to second order algorithms commonly used to treat the perpendicular dynamics, such as the Arakawa scheme. Both errors are anyway small enough to carry out feasible plasma turbulence simulations for times longer than the Bohm time. These tests also show explicitly the capability to simulate drift-wave propagation with toroidal mode numbers exceeding the Nyquist cutoff (half of the toroidal grid points). This is a situation which could not be dealt with by the straightforward approach that computes the derivative as a combination of the poloidal and of the toroidal derivatives, unless a large number of both poloidal and toroidal points is used. Thus the new method needs only a few tens of toroidal points, regardless of the toroidal mode number, provided that adequate resolution is available in the poloidal plane. But high resolution in the poloidal plane is not an additional constraint since it is anyway necessary to treat the perpendicular dynamics accurately. When applied to turbulence simulations of a machine like ITER, I showed that the new approach allows one to save a couple of orders of magnitude in computer resources.

Fully nonlinear simulation results of a 3-dimensional 4-field ITG model are presented in Chapter 5. Some of the linear properties of the ITG instability in magnetized plasmas have been recalled with a special focus on its growth rates and threshold. Then a convergence test was performed in the nonlinear turbulent regime, showing fast convergence achieved at $nz = 15$, where more traditional approaches would have failed, as explained in the manuscript. A result with which I have successfully showed that one needs only a few tens of toroidal points to describe the target physics problem, regardless of the toroidal mode number, provided that adequate resolution is available in the poloidal plane. Finally, I finish by proving that in the presence of a magnetic island, the study of drift-wave propagation across the X-point gives results in good agreement with the exact solutions of this problem. The corresponding quadratic properties are also shown to be adequately conserved. Most importantly, convergence of the numerical solution is verified with respect to the number of points in the z direction allowing one to consider a much thinner grid to study the same Physics.

I finally conclude this thesis by the following: the FCI approach prevails by allowing, not only flux-coordinate independent operations in the poloidal plane as discussed in Chapter 2, but it also allows complex magnetic geometries free of singularities. It deals without difficulty with X-point configurations and with O-points such as the magnetic axis. The flexible nature of the code FENICIA allowed us to demonstrate the application of this coordinate system to a magnetic island in a slab (see Chapter 5), thus the validity of its application to X-point configurations.

6.2 Future Work and Final Thoughts

Field-aligned mapping across the islands is now possible using our simulations with FENICIA. Several critical problems can now be addressed. It is of great importance to study the physics of the interaction of islands and turbulence. So far, the results presented in Chapter 5 allowed one to validate the FCI approach in the presence of a prescribed magnetic island. Investigating the effect of such an island on drift-wave turbulence is a straightforward next step. This is a foregoing work currently addressed by P. HILL. The next important step would then be to study this interaction in a self-consistent model, where both the island and turbulence are simultaneously evolved. Future work should also consider including the physics of electrons and electromagnetic effects, so electrons can no longer be adiabatic and resolving the electron motion would be a necessary step forward.

Our primary focus should be to add more physics to our equations in FENICIA until we are confident that they are experimentally relevant. Realistic experimental ITER-type parameters for direct comparisons with experiments will then be possible. One should certainly consider completing our transport model by first incorporating the curvature terms in the code so as to model the toroidal branch of ITG turbulence. But the nonlinear simulation results presented in this thesis are in cylindrical magnetic geometry. Thus, including the effects of a toroidal magnetic geometry is a straightforward next step. A long-term foresight would be studying turbulence and transport across the last closed field surface (LCFS) in an axisymmetric X-point configuration. This will require the treatment of physics related to the the Scrape-Off Layer, particularly the physics of plasma-wall interaction.

A difficulty using the Flux Coordinate Independent (FCI) approach is that it hardly allows the computation of the flux-surface average term. In the case of adiabatic electrons, the flux-surface-average term needs to be computed, but is time and memory consuming for three-dimensional configurations. This issue should thus be carefully addressed to figure out the cheapest algorithm to implementing this term. This will also be very useful for physical diagnostics looking into the time evolution of equilibrium quantities.

Finally, the validation of FENICIA has been done by comparing numerical with exact solutions through purely theoretical simplified problems. Benchmarks with other fluid simulations and kinetic simulations is worthy of further investigations. An important point to say in that regard is that the FCI approach could be implemented in any existing modular code, including gyrokinetic codes. An interesting extension would also be to implement the gyrokinetic description into FENICIA, hence moving from three to five dimensions.

Appendix A

This is a small note to draw the reader's attention to some stability criteria that should be satisfied when running a simulation. Consider the following equation:

$$\partial_t n + C\, \nabla_{\|} n = 0 \tag{A.1}$$

where n is the density, C is the speed of the wave and $\nabla_{\|} = \partial_\theta / q + \partial_\varphi$. Solutions to this equation can be written as

$$n(r, \theta, \varphi) = n_0(r) cos(m\, \theta - n\, \varphi - \omega(r) t) \tag{A.2}$$

with $n_0(r)$ being a function centered around the rational surface and

$$\begin{aligned} \left\| \frac{\nabla_{\|} n}{n} \right\| &= \left\| \frac{-n_0(r)\, (m/q - n) sin(m\, \theta - n\, \varphi - \omega(r) t)}{n} \right\| && \text{(A.3)} \\ &\sim \omega'(r) t && \text{(A.4)} \end{aligned}$$

Knowing that the wave frequency $\omega(r) = C\, (m/q(r) - n)$. The constraint to be satisfied for a wave to be well-resolved is

$$\omega'(r) t \Delta x \ll 1 \tag{A.5}$$

We write

$$\begin{aligned} \omega'(r) t &= -\frac{m}{r\, q(r)} \left(\frac{r\, q'(r)}{q(r)} \right) && \text{(A.6)} \\ &= \frac{k_\theta \hat{s}}{q(r)} && \text{(A.7)} \end{aligned}$$

For $q_s = 1 + 2r_s^2$, the expression of the magnetic shear at the rational surface writes

$$\begin{aligned} \hat{s} &= \frac{r_s\, q'(r_s)}{q(r_s)} && \text{(A.8)} \\ &= \frac{4r_s^2}{1 + 2r_s^2} && \text{(A.9)} \end{aligned}$$

Replace expression A.9 in A.7 to get

$$\omega'(r) t = \frac{2m(q_s - 1)}{q_s^2} \tag{A.10}$$

For a given r_s, m and Δx, we get t the maximum sufficient time to study the physics we seek. For instance, if $r_s = \sqrt{2}/2$, $m = 4$ and $\Delta x = 10^{-2}$, then the maximum time is $t = 10$.

Appendix B

Consider the one-dimensional version of (4.17), which is a good approximation for the case of small wavelengths:

$$\partial_t n + \partial_x n = 0 \tag{B.1}$$

Assume periodic boundary conditions in x and perform a uniform discretization in x with centered finite differences. Take initial conditions of the form $n = coskx$ and look for solutions of the form

$$n_i = \alpha_c \cos kx_i + \alpha_s \sin kx_i \tag{B.2}$$

Then

$$n_{i+1} - n_{i-1} = -2\alpha_c \ \sin k\Delta x \ \sin kx_i + 2\alpha_s \ \sin k\Delta x \ \cos kx_i \tag{B.3}$$

Call the numerical frequency

$$\omega_n = \frac{\sin k\Delta x}{\Delta x} \ \text{ such that } \ \lim_{x\to 0} \frac{\sin k\Delta x}{\Delta x} = k \tag{B.4}$$

Thus the numerical solution to the system can be written, to all orders in time, as

$$n_i = \cos \omega_n t \ \cos kx_i + \sin \omega_n t \ \sin kx_i \tag{B.5}$$

and the exact solution as

$$n_{exact} = \cos k(x_i - t) = \cos \omega t \ \cos kx_i + \sin \omega t \ \sin kx_i \tag{B.6}$$

From the expression of the error

$$E^2 = \frac{\langle (n_{exact} - n_i)^2 \rangle}{\langle (n_{exact})^2 \rangle} \tag{B.7}$$

where $< . >$ denotes the average over x_i, one finds that $E \approx k^3 \Delta x^2$ for $k\,\Delta x \ll 1$. This is indeed what is obtained for case **3** of Fig. 4.5, in both m (k) and Δx.

Appendix C

The problem can be illustrated by the vorticity equation for two-dimensional incompressible flow

$$\frac{\partial \xi}{\partial t} + \mathbf{v}.\boldsymbol{\nabla}\xi = 0, \tag{C.1}$$

where

$$\mathbf{v} = \mathbf{k} \times \boldsymbol{\nabla}\psi$$
$$\xi = \mathbf{k}.\boldsymbol{\nabla} \times \mathbf{v} \equiv \nabla^2\psi$$

and ψ is the stream function so that

$$\begin{cases} v_x = -\partial_y\psi \\ v_y = \partial_x\psi \end{cases}$$

because we are in a 2D incompressible case where $\boldsymbol{\nabla}.\mathrm{v} = 0$, $\boldsymbol{\nabla}$ is the two-dimensional del operator, and $\mathbf{k}$ is the unit vector perpendicular to the plane of motion.

Verification:

$$\mathbf{v} = \mathbf{k} \times \boldsymbol{\nabla}\psi = \begin{vmatrix} \mathbf{i} & \mathbf{j} & \mathbf{k} \\ 0 & 0 & 1 \\ \partial_x\psi & \partial_y\psi & 0 \end{vmatrix} = \begin{pmatrix} -\partial_y\psi \\ \partial_x\psi \\ 0 \end{pmatrix}$$

and

$$\begin{aligned} \xi &= \mathbf{k}.\boldsymbol{\nabla} \times \mathbf{v} \\ &= \begin{pmatrix} 0 \\ 0 \\ 1 \end{pmatrix} \begin{vmatrix} \mathbf{i} & \mathbf{j} & \mathbf{k} \\ \partial_x\psi & \partial_y\psi & 0 \\ v_x & v_y & 0 \end{vmatrix} \\ &= \nabla^2\psi \end{aligned}$$

In Eq. (C.1), use $\mathbf{v} = \mathbf{k} \times \boldsymbol{\nabla}\psi$ to get

$$\frac{\partial \xi}{\partial t} + (\mathbf{k} \times \boldsymbol{\nabla}\psi).\boldsymbol{\nabla}\xi = 0$$

$$\Rightarrow \frac{\partial \xi}{\partial t} + \begin{pmatrix} -\partial_y\psi \\ \partial_x\psi \\ 0 \end{pmatrix} . \begin{pmatrix} \partial_x\xi \\ \partial_y\xi \\ 0 \end{pmatrix} = 0$$

Finally, Eq. (C.1) can be rewritten as

$$\begin{aligned}\frac{\partial \xi}{\partial t} &= \partial_x \xi \, \partial_y \psi - \partial_y \xi \, \partial_x \psi && \text{(C.2)} \\ &= \{\xi, \psi\} && \text{(C.3)} \\ &= J(\xi, \psi) && \text{(C.4)}\end{aligned}$$

Or

$$\frac{\partial \nabla^2 \psi}{\partial t} = J(\nabla^2 \psi, \psi) \tag{C.5}$$

where J is the Jacobian operator with respect to the cartesian coordinates, x and y, in the plane. When the Jacobian in this equation is replaced by space differences of the usual form,

$$J_{i,j}(\xi, \psi) = \frac{1}{4d^2}[(\xi_{i+1,j} - \xi_{i-1,j})(\psi_{i,j+1} - \psi_{i,j-1}) - (\xi_{i,j+1} - \xi_{i,j-1})(\psi_{i+1,j} - \psi_{i-1,j})], \tag{C.6}$$

where i is the finite difference grid index in x, j is the index in y and d is the grid interval, and the equation is integrated over some tens of time steps, using an ordinary time-centered differencing scheme, it is found that the solution begins to show a characteristic structure termed "stretching" or "noodling" [Baer 1961]. This is a structure in which the motion degenerates into eddies of a few grid intervals in size and of elongated, filamented shape. The early stages of this noodling can be due to physical processes, but, once formed, the eddies usually intensify without limit, causing numerical computational instability and explosive growth of the total kinetic energy of the system. Platzman [Baer 1961] recognized the existence of "aliasing errors", or errors due to misrepresentation of the shorter waves because of the inability of the finite grid to properly resolve them. Phillips [Phillips 1959] further showed that the above computational instability can be caused by this "aliasing".

According to [Arakawa 1966], the proper derivation of the FD Jacobian in order to overcome the instability without sacrificing its accuracy can be written as

$$\begin{aligned}J_{i,j}(\xi, \psi) = -\frac{1}{12d^2}\,[\,&(\psi_{i,j-1} + \psi_{i+1,j-1} - \psi_{i,j+1} - \psi_{i+1,j+1})(\xi_{i+1,j} - \xi_{i,j}) \\ +\; &(\psi_{i-1,j-1} + \psi_{i,j-1} - \psi_{i-1,j+1} - \psi_{i,j+1})(\xi_{i,j} - \xi_{i-1,j}) \\ +\; &(\psi_{i+1,j} + \psi_{i+1,j+1} - \psi_{i-1,j} - \psi_{i-1,j+1})(\xi_{i,j+1} - \xi_{i,j}) \\ +\; &(\psi_{i+1,j-1} + \psi_{i+1,j} - \psi_{i-1,j-1} - \psi_{i-1,j})(\xi_{i,j} - \xi_{i,j-1}) \\ +\; &(\psi_{i+1,j} - \psi_{i,j+1})(\xi_{i+1,j+1} - \xi_{i,j}) \\ +\; &(\psi_{i,j-1} - \psi_{i-1,j})(\xi_{i,j} - \xi_{i-1,j-1}) \\ +\; &(\psi_{i,j+1} - \psi_{i-1,j})(\xi_{i-1,j+1} - \xi_{i,j}) \\ +\; &(\psi_{i+1,j} - \psi_{i,j-1})(\xi_{i,j} - \xi_{i+1,j-1}),\end{aligned} \tag{C.7}$$

Appendix D

Consider the following model pertaining only the parallel dynamics:

$$\partial_t \phi + C\,\nabla_{\|}\phi = 0 \tag{D.1}$$

with a magnetic field of the form

$$\psi(x,y) = -\frac{(x-1)^2}{2} + A\cos(y) \tag{D.2}$$

The parallel gradient operators can then be written as:

$$\nabla_{\|} = -[\psi,\cdot] + \partial_z. \tag{D.3}$$

In order to construct exact solutions to the above model in the presence of a magnetic island, the idea is to define a coordinate system: $(x,y) \longrightarrow (\rho', y')$ such thatψ is a magnetic surface label, i.e: $\nabla_{\|}\psi = 0$. One would write

$$\begin{aligned}
\rho' &= -\psi/A = \frac{(x-1)^2}{2A} - \cos y && \text{(D.4)}\\
y' &= y && \text{(D.5)}\\
x' &= x-1 && \text{(D.6)}
\end{aligned}$$

where ρ is a normalization of ψ so that $\rho = 1$ refers to the separatrix. Note that at $y = 0$ (O-point), $\cos y \sim 1 - y^2/2 \longrightarrow \rho' \simeq \frac{(x-1)^2}{2A} - 1 + y^2/2$ which defines the equation of an ellipse. With this set of coordinates, the spatial derivatives in the x and y directions write:

$$\begin{aligned}
\partial_x &= \partial_x\rho'\,\partial_{\rho'} + \partial_x y'\,\partial_{y'} = x'\,\partial_{\rho'}/A && \text{(D.7)}\\
\partial_y &= \partial_y\rho'\,\partial_{\rho'} + \partial_y y'\,\partial_{y'} = \sin y\,\partial_{\rho'} + \partial_{y'} && \text{(D.8)}
\end{aligned}$$

This leads to a parallel operator of the form

$$\begin{aligned}
\nabla_{\|} &= x'\,\partial_y + A\sin y\partial_x + \partial_z && \text{(D.9)}\\
&= x'(\sin y\,\partial_{\rho'} + \partial_{y'}) - x'\sin y\,\partial_{\rho'} + \partial_z\\
&= x'\,\partial_{y'} + \partial_z
\end{aligned}$$

Eq. (D.1) can then be written as

$$\partial_t \phi + x'(\rho', y')\, \partial_{y'} \phi + \partial_z \phi = 0 \tag{D.10}$$

where $x'(\rho', y') = \pm\sqrt{(2A)}\, (\rho' + \cos y')^{1/2}$. At this point, to ensure the separation of variables, one defines a new system: $(\rho', y') \longrightarrow (\rho, \eta)$ such that

$$x'\partial_y \equiv \sqrt{(2A)}\, g(\rho)\, \partial_\eta = \pm\sqrt{(2A)}\, (\rho' + \cos y')^{1/2} \tag{D.11}$$

We conclude from (D.11) that

$$\partial_\eta = \frac{g(\rho)\, dy'}{(\rho' + \cos y')^{1/2}} \tag{D.12}$$

so for $x' > 0$, the new variable η can be expressed as

$$\eta = \left[g(\rho) \int\limits_0^y \frac{dy'}{(\rho + \cos y')^{1/2}} \right]_{\rho = x'^2/(2A) - \cos y} \tag{D.13}$$

with $g(\rho)$ chosen such that

$$\begin{aligned} \eta(x', y = \pi) &= \pi\, \forall x' \\ \eta(x', y = -\pi) &= -\pi \end{aligned} \tag{D.14}$$

This gives

$$\pi = g\left(1 + \frac{x'^2}{2A}\right) \int\limits_0^\pi \frac{dy'}{\left[\cos y' + \left(1 + \frac{x'^2}{2A}\right)\right]^{1/2}} \quad \forall x' \tag{D.15}$$

so

$$g(\rho) = \pi \left[\int\limits_0^\pi \frac{dy'}{(\cos y' + \rho)^{1/2}} \right]^{-1} \quad \forall x' \tag{D.16}$$

The function η is regular everywhere, but delicate near $\rho = \pm 1$ (X and O points) where $\int_0^y dy'/(\rho' + \cos y')^{1/2}$ diverges. When $\rho < 1$, the argument of the integral involves the term $(\cos y' + \rho)^{1/2}$ which becomes negative at $\cos y' = -\rho$. We choose to limit the integration to the upper bound y_M such that $\cos y_M = -\rho$. The situation is described through a schematic of the island in Fig. D.1. The explicit expression of $g(\rho)$ at the exterior of the island (i.e: $\rho > 1$) can be derived as follows:

$$\begin{aligned} \int\limits_0^\pi \frac{dy'}{(\rho' + \cos y')^{1/2}} &= \int\limits_0^{\pi/2} \frac{2d\theta}{(\rho + \cos 2\theta)^{1/2}} \\ &= \int\limits_0^{\pi/2} 2d\theta\, \left[\rho + (1 - 2\,\sin^2\theta)\right]^{-1/2} \\ &= \int\limits_0^{\pi/2} 2d\theta\, (\rho + 1)^{-1/2}\, \left[1 - 2\,\sin^2\theta/(1 + \rho)\right]^{-1/2} \end{aligned} \tag{D.17}$$

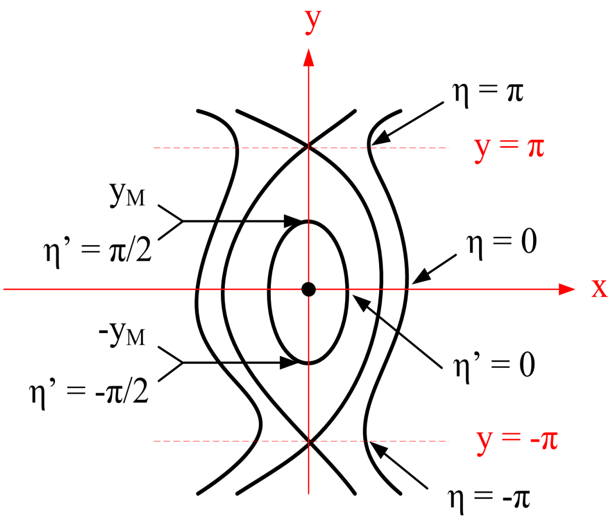

Figure D.1: A schematic of an island with the new variables

Use definitions of elliptic integrals of first kind

$$K(m) \equiv \int_0^{\pi/2} d\theta \, (1 - m \sin^2 \theta)^{-1/2} \tag{D.18}$$

to get

$$\int_0^{\pi} dy' \, (\rho + \cos y')^{-1/2} = 2\,(1+\rho)^{1/2}\, K\left(\frac{2}{1+\rho}\right) \tag{D.19}$$

Note that $K\,(2/(1+\rho)$ diverges logarithmically as $\rho \longrightarrow 1^+$. Finally, for $\rho > 1$, $g(\rho)$ can be written as

$$g(\rho) = \frac{\pi}{2}\,(1+\rho)^{1/2} \left[K\left(\frac{2}{1+\rho}\right)\right]^{-1} \tag{D.20}$$

At the interior of the island (i.e: $\rho < 1$), however, the limit of integration is y_M such that $\cos y_M = -\rho$. Thus

$$\eta' = \left[g(\rho) \int_0^{y} \frac{dy'}{(\rho + \cos y')^{1/2}} \right]_{\rho = x'^2/(2A) - \cos y} \tag{D.21}$$

but now

$$g(\rho) = \frac{\pi}{2} \left[\int_0^{y_M} \frac{dy'}{(\cos y' + \rho)^{1/2}} \right]^{-1} \quad \forall x' \tag{D.22}$$

In order to express $g(\rho)$ as a function of K, the elliptic integral, we proceed by first rewriting the expression $I = \int_0^{y_M} dy' \, (\cos y' + \rho)^{-1/2}$ by change of variables. We indeed have

$$\cos y' = 1 - (1+\rho)\sin^2 \alpha \tag{D.23}$$

where $0 \leq \alpha \leq \pi/2$. Thus

$$(\cos y' + \rho)^{-1/2} = (1+\rho)^{-1/2}(1-\sin^2\alpha)^{-1} = (1+\rho)^{-1/2}(\cos\alpha)^{-1} \tag{D.24}$$

Moreover, by differentiation we get

$$-\sin y'\, dy' = -2(1+\rho)\sin\alpha\cos\alpha\, d\alpha \tag{D.25}$$

Also,

$$\sin^2 y' = 1 - \cos^2 y' = 2\,(1+\rho)\,\sin^2\alpha\,\left[1 - \frac{1+\rho}{2}\,\sin^2\alpha\right] \tag{D.26}$$

yielding

$$\sin y' = \left[2\,(1+\rho)\right]^{1/2}\,\sin\alpha\,\left[1 - \frac{1+\rho}{2}\,\sin^2\alpha\right]^{1/2} \tag{D.27}$$

and

$$dy' = \left[2\,(1+\rho)\right]^{1/2}\,\cos\alpha\,\left[1 - \frac{1+\rho}{2}\,\sin^2\alpha\right]^{1/2}\,d\alpha \tag{D.28}$$

Hence,

$$I = \sqrt{2}\int_0^{\pi/2} \frac{d\alpha}{\left[1 - \frac{1+\rho}{2}\sin^2\alpha\right]^{1/2}} \tag{D.29}$$

$$= \sqrt{2}\,K\left(\frac{1+\rho}{2}\right) \tag{D.30}$$

Finally for $\rho < 1$ we have,

$$g(\rho) = \frac{\pi}{2^{3/2}}\,\left[K\left(\frac{1+\rho}{2}\right)\right]^{-1} \tag{D.31}$$

For $x' < 0$, as shown in Fig. D.1, η' needs to be completed. We define

$$\eta' = \pi - \left[g(\rho)\int_0^y \frac{dy'}{(\rho+\cos y')^{1/2}}\right]_{\rho = x'^2/(2A) - \cos y} \tag{D.32}$$

so that $\pi/2 \leq \eta' \leq 3\pi/2$ when $x' < 0$. And

$$\eta' = 2\pi + \left[g(\rho)\int_0^y \frac{dy'}{(\rho+\cos y')^{1/2}}\right]_{\rho = x'^2/(2A) - \cos y} \tag{D.33}$$

for $x' > 0$, but $y < 0$ if one wants $3\pi/2 \leq \eta' \leq 2\pi$ in the fourth quadrant.

Bibliography

[Arakawa 1966] A. Arakawa. *Computational design for long-term numerical integration of the equations of fluid motion: Two-dimensional incompressible flow. Part I.* Journal of Computational Physics, vol. 1, no. 1, pages 119–143, 1966.

[Baer 1961] F. Baer and G.W. Platzman. *A Procedure for Numerical Integration of the Spectral Vorticity Equation.* Journal of Atmospheric Sciences, vol. 18, pages 393–401, 1961.

[Beer 1995] M.A. Beer, S.C. Cowley and G.W. Hammett. *Field-aligned coordinates for nonlinear simulations of tokamak turbulence.* Physics of Plasmas, vol. 2, page 2687, 1995.

[Boozer 1980] Allen H Boozer. *Guiding center drift equations.* Physics of Fluids, vol. 23, page 904, 1980.

[Boozer 1981] Allen H Boozer. *Plasma equilibrium with rational magnetic surfaces.* Physics of Fluids, vol. 24, page 1999, 1981.

[Chen 1984] Francis F Chen and MA Lieberman. Introduction to plasma physics and controlled fusion/francis f. : Plenum Press, New York, 1984.

[Connor 1979] JW Connor, RJ Hastie and JB Taylor. *High mode number stability of an axisymmetric toroidal plasma.* Proceedings of the Royal Society of London. A. Mathematical and Physical Sciences, vol. 365, no. 1720, pages 1–17, 1979.

[Connor 1988] J.W. Connor, S.C. Cowley, R.J. Hastie, T.C. Hender, A Hood and T.J. Martin. *Tearing modes in toroidal geometry.* Physics of Fluids, vol. 31, page 577, 1988.

[Cowley 1986] S.C. Cowley, R.M. Kulsrud and T.S. Hahm. *Linear stability of tearing modes.* Physics of Fluids, vol. 29, page 3230, 1986.

[Cowley 1991] S.C. Cowley, RM Kulsrud and R. Sudan. *Considerations of ion-temperature-gradient-driven turbulence.* Physics of Fluids B: Plasma Physics, vol. 3, page 2767, 1991.

[Dimits 1993] A. M. Dimits. *Fluid simulations of tokamak turbulence in quasiballooning coordinates*. Phys. Rev. E, vol. 48, pages 4070–4079, Nov 1993.

[Dorland 1993a] W. Dorland. *Gyrofluid Models of Plasma Turbulence*. PhD thesis, 1993.

[Dorland 1993b] W. Dorland and G.W. Hammett. *Gyrofluid turbulence models with kinetic effects*. Physics of Fluids B: Plasma Physics, vol. 5, page 812, 1993.

[Fonck 1993] RJ Fonck, G Cosby, RD Durst, SF Paul, N Bretz, S Scott, E Synakowski and G Taylor. *Long-wavelength density turbulence in the TFTR tokamak*. Physical review letters, vol. 70, no. 24, pages 3736–3739, 1993.

[Hamada 1962] Shigeo Hamada. *Hydromagnetic equilibria and their proper coordinates*. Nuclear Fusion, vol. 2, no. 1-2, page 23, 1962.

[Hammett 1990] G.W. Hammett and F.W. Perkins. *Fluid moment models for Landau damping with application to the ion-temperature-gradient instability*. Phys. Rev. Lett., vol. 64, pages 3019–3022, Jun 1990.

[Hammett 1992] G.W. Hammett, W. Dorland and F.W. Perkins. *Fluid models of phase mixing, Landau damping, and nonlinear gyrokinetic dynamics*. Physics of Fluids B: Plasma Physics, vol. 4, page 2052, 1992.

[Hammett 1993] G.W. Hammett, M.A. Beer, W. Dorland, S.C. Cowley and S.A. Smith. *Developments in the gyrofluid approach to Tokamak turbulence simulations*. Plasma Physics and Controlled Fusion, vol. 35, no. 8, page 973, 1993.

[Hariri 2013] F. Hariri and M. Ottaviani. *A flux-coordinate independent field-aligned approach to plasma turbulence simulations*. Computer Physics Communications, vol. 184, no. 11, pages 2419 – 2429, 2013.

[Hasegawa 1983] Akira Hasegawa and Masahiro Wakatani. *Plasma edge turbulence*. Physical Review Letters, vol. 50, no. 9, page 682, 1983.

[Hazeltine 2003] Richard D Hazeltine and James D Meiss. Plasma confinement. Courier Dover Publications, 2003.

[Holtkamp 2007] Norbert Holtkamp. *An overview of the ITER project*. Fusion Engineering and Design, vol. 82, no. 5, pages 427–434, 2007.

[Johnson 2005] SG Johnson and M Frigo. *The design and implementation of FFTW3*. Proc. IEEE, vol. 93, pages 216–231, 2005.

[Kim 1994] J. Y. Kim and M. Wakatani. *Radial Structure of High-Mode-Number Toroidal Modes in General Equilibrium Profiles*. Phys. Rev. Lett., vol. 73, pages 2200–2203, Oct 1994.

[M.A.Beer 1995] M.A.Beer. *Gyrofluid Models of Turbulent Transport in Tokamaks*. PhD thesis, 1995.

[Max 1977] Jacques Max, Daniel Berthier and Louis Néel. Méthodes et techniques de traitement du signal et applications aux mesures physiques: principes et appareillages de traitement en temps réel. Masson, 1977.

[Mazzucato 1993] E Mazzucato and R Nazikian. *Radial scale length of turbulent fluctuations in the main core of TFTR plasmas*. Physical review letters, vol. 71, no. 12, pages 1840–1843, 1993.

[Melrose 1989] Don B Melrose. Instabilities in space and laboratory plasmas. Cambridge University Press, 1989.

[Ottaviani 1999] M. Ottaviani and G. Manfredi. *The gyro-radius scaling of ion thermal transport from global numerical simulations of ion temperature gradient driven turbulence*. Physics of Plasmas, vol. 6, page 3267, 1999.

[Ottaviani 2011] M. Ottaviani. *An alternative approach to field-aligned coordinates for plasma turbulence simulations*. Physics Letters A, vol. 375, no. 15, pages 1677 – 1685, 2011.

[Phillips 1959] NA Phillips. *The atmosphere and the sea in motion*. Rockefeller Inst. Press, New York, 1959.

[Press 2007] William H Press. Numerical recipes 3rd edition: The art of scientific computing. Cambridge university press, 2007.

[Sarazin 2009] Y. Sarazin, G. Dif-Pradalier, D. Zarzoso, X. Garbet, Ph. Ghendrih and V. Grandgirard. *Entropy production and collisionless fluid closure*. PPCF, vol. 51, page 13, 2009.

[Scott 1998] B. Scott. *Global consistency for thin flux tube treatments of toroidal geometry*. Physics of Plasmas, vol. 5, page 2334, 1998.

[Scott 2001] B. Scott. *Shifted metric procedure for flux tube treatments of toroidal geometry: Avoiding grid deformation*. Physics of Plasmas, vol. 8, page 447, 2001.

[Tomabechi 1991] K Tomabechi, JR Gilleland, Yu A Sokolov, R Toschi and ITER Team. *ITER conceptual design*. Nuclear Fusion, vol. 31, no. 6, page 1135, 1991.

[Wesson 2011] John Wesson. Tokamaks, volume 149. OUP Oxford, 2011.

[White 1984] RB White and MS Chance. *Hamiltonian guiding center drift orbit calculation for plasmas of arbitrary cross section*. Physics of Fluids, vol. 27, page 2455, 1984.

[Zweben 1989] SJ Zweben and SS Medley. *Visible imaging of edge fluctuations in the TFTR tokamak*. Physics of Fluids B: Plasma Physics, vol. 1, page 2058, 1989.